NUMERICAL SIMULATION OF THE TRUSS SPAR

'HORN MOUNTAIN' USING COUPLE

A Thesis

by

BASIL THECKUM PURATH

Submitted to the Office of Graduate Studies of
Texas A&M University
in partial fulfillment of the requirements for the degree of

MASTER OF SCIENCE

May 2006

Major Subject: Ocean Engineering

NUMERICAL SIMULATION OF THE TRUSS SPAR

'HORN MOUNTAIN' USING COUPLE

A Thesis

by

BASIL THECKUM PURATH

Submitted to the Office of Graduate Studies of
Texas A&M University
in partial fulfillment of the requirements for the degree of

MASTER OF SCIENCE

Approved by:

Chair of Committee,	Jun Zhang
Committee members,	Richard S. Mercier
	Achim Stossel
Head of Department,	David Rosowsky

May 2006

Major Subject: Ocean Engineering

ABSTRACT

Numerical Simulation of the Truss Spar 'Horn Mountain' Using COUPLE. (May 2006)
Basil Theckum Purath, B.Tech.,
Cochin University of Science and Technology,
Kerala, India
Chair of Advisory Committee: Dr. Jun Zhang

A truss spar, named as Horn Mountain, was deployed in the Gulf of Mexico in 1,650 m of water, approximately 150 km southeast of New Orleans in June 2002. Horn Mountain is operated by British Petroleum (B.P.). Extensive field measurements were made using an integrated marine monitoring system attached to the truss spar. In this study, dynamic analysis of the truss spar interacting with its mooring and riser system was performed using a time-domain numerical code, known as 'COUPLE'. The simulated results were then compared with the corresponding field measurements made during Hurricane Isidore.

During the numerical study, various hydrodynamic parameters which were crucial to the accuracy of predicting the global motions of the truss spar and tensions in mooring lines and risers were scrutinized, such as the drag and added-mass coefficients of heave plates, hard tank and truss beams. Satisfactory agreement between the simulation and corresponding measurements was reached, indicating that the numerical code, COUPLE, can be used to conduct the time-domain analysis of a truss spar interacting with its mooring and riser system under severe storm impact.

A comparative study was also conducted to analyze the significance of interaction of risers with the hull structure. Three different cases of coupled analysis are simulated, namely (i) coupled analysis of truss spar interacting with mooring lines, (ii) coupled analysis of truss spar interacting with the mooring lines and the steel catenary risers, (iii) coupled analysis of truss spar interacting with the mooring lines, the steel catenary risers and top tension risers. Major statistical parameters of the global motions

of the truss spar and the mooring line tensions for the three cases are compared with the field measurements.

ACKNOWLEDGEMENTS

I express my sincere gratitude to Dr. Steve Perryman, B.P., who provided me the field measurements of Horn Mountain truss spar during Hurricane Isidore. Without his timely help I wouldn't have finished this thesis.

I would like to thank Dr. John Halkyard, Technip for his valuable guidance on the details of the truss spar. I also would like to thank Dr. Igor Prislin, Scientific Marine Services for his guidance on the processing of field data.

I would like to thank my chair, Dr. Jun Zhang, for his guidance and contribution to my understanding of this research and the subject of offshore floating systems as a whole. I would also like to thank my advisory committee members: Dr. Richard S. Mercier and Dr. Achim Stossel, for their trust and guidance throughout this research project.

I also wish to thank my fellow classmates and friends for their active help and contribution, especially Mr. Rajith Padmanabhan, Ms. Amal Chellappan and Mr. Vimal Vinayan. Finally, special thanks to my family for their constant support and motivation without which I would have never come this far.

TABLE OF CONTENTS

Page

Page

LIST OF TABLES

Page

LIST OF FIGURES

Page

Page

Page

1. INTRODUCTION

1.1 Recent Trends in Deep Water Oil Exploration

As offshore oil and gas exploration is pushed into deeper and deeper waters, many innovative floating offshore structures are considered for a variety of reasons such as cost savings, enhanced global performance, reduced tensions in the mooring lines and flexibility in the use of risers. Spar platforms are one such compliant offshore floating structure used for deep water applications for the drilling, production, processing, and storage and offloading of petroleum and natural gas. So far 14 spar platforms have been installed in the Gulf of Mexico. The two most common types of hull configurations used in the Gulf of Mexico are the Classic Spar and the Truss Spar (Magee et al., 2000).

A classic spar has a cylindrical cross section along its entire length and is divided into three major sections. The top section is the 'Hard Tank' that supports the topsides by the virtue of its buoyancy. This also carries the variable ballast for different loading conditions. The bottom section is called the 'Soft Tank' which is used for combining solid ballast and seawater ballast and improves the stability of the structure by bringing down the center of gravity of the structure. A circular mid section which separates the hard tank and the soft tank is flooded and can be used for oil storage. The soft tank and the midsection are usually freely flooded in order to pressure-equalize with the external hydrostatic pressure. The spar structures are also characterized by a central well which is also known as the 'Moonpool' and is open to sea water. The reduced fluid motions inside this moonpool relative to the hull allow the risers, umbilicals and other accessories to be carried to the topsides.

When the storage capability of a classic spar is not required, the truss spar provides a lighter, more cost-effective alternative that still maintains the same motion

---

This thesis follows the style of *Journal of Waterway, Port, Coastal, and Ocean Engineering.*

characteristics of a classic spar. In a truss spar, the circular midsection of a classic spar is replaced with a truss structure. This truss structure usually consists of four vertical legs connected together by a lattice frame work of horizontal and inclined braces. This truss structure is divided into different sections by means of square horizontal plates at various elevations (known as the 'Heave Plates'). Truss spars have a reduced draft compared to classic spars leading to increased heave motions. But the presence of heave plates effectively reduce the heave motions of the structure.

More recent developments in spars include the third generation spar, also known as the 'Cell Spar'. It is designed as an alternative to long-distance tie back of risers. This type of spar design consists of a vertical configuration of several small diameter cylinders forming a giant column instead of a single circular cross section. One of the important advantages of such a spar is its economy, a small size and an ease of fabrication. These less expensive cell spars will enable producers to look at deepwater reserves that in the past might have been too small to develop economically.

The spar structures also have strakes, attached in a helical fashion around the exterior of the cylinder, to mitigate the vortex induced vibrations of the structure induced by currents. The spars are held in place by a semi taut or taut lateral catenary mooring system. The mooring lines are attached to the structure through fairleads which are normally located near the center of gravity where the global motions are the least, there by reducing the dynamic tensions in the mooring lines.

The common features of spars are listed below:

- It can be operated in very deep waters up to 3000 m of water depth for drilling and production and storage
- It can have a large range of topside payloads
- It is easy to fabricate
- It can be used for phased field development due to its ability to move the facility and drill additional wells under the spar.

- After years of use, at the end of a field's productive life, a spar platform can be moved to a new location. This makes it economically feasible to develop smaller deepwater fields.
- Rigid steel production risers are supported in the center well by separate buoyancy cans
- It is always stable since the center of buoyancy is significantly above the center of gravity
- Oil can be stored at low marginal cost,
- The mooring system is easy to install, operate and relocate

There are various challenges in the design and analysis of spar structures due to uncertainties in various load and response parameters. These include difficulties in predicting hydrodynamic coefficients of the hull structure, heave plates, mooring lines and risers and uncertainties in the metocean environment.

1.2 Significance of Truss Spars in Gulf of Mexico

In the Gulf of Mexico where oil storage is seldom a requirement, truss spars are the most widely used spars. The truss section of the spar is much cheaper to fabricate and it reduces the total weight of the spar enhancing the payload capacity. The truss also provides relative transparency to ambient current resulting in less surge and sway offset and mooring requirements and greater flexibility in riser designs. There are currently 9 truss spars installed in Gulf of Mexico. From the feed back obtained from the field measurements, the global performance of these truss spars is found to be excellent.

1.2.1 Advantages of Truss Spars

The salient features of truss spars over classic spar (Magee et al., 2000) are described below.

- Reduction in the total weight of the hull and fabrication costs
- Easy to fabricate

- Reduced drag loads leading to smaller surge offset in a high current environment and reduced loads on the mooring lines.
- Heave plates reduce the heave motions of a truss spar leading to reduced fatigue loads on the risers
- Reduced draft allows shallower water applications
- Better VIV performance as the truss section is transparent to current
- Can be transported dry and in one piece close to the installation site
- Flexibility in the installation of steel catenary risers (SCR) as truss sections allow to carry the risers through the sides of the spar

1.2.2 Challenges in the Design of Truss Spars

As discussed earlier, one of the salient features of truss spars is the heave plates. The effectiveness of the heave plates is crucial to the heave performance of a truss spar. The heave plates trap a large amount of water which moves along with the structure. This trapped water is known as added mass. Effective heave plates increase the added mass of a structure leading to an increase in the heave natural period typically in the range of 22-30 seconds and detune from the ambient wave period range of 15-20 seconds. Hydrodynamic damping induced by the heave plates is also effective in reducing the heave motions of a spar. Various studies and experiments indicated that heave motion is primarily inertia dominated and the effect of drag damping is less significant (Magee et al., 2000) Due to its quadratic nature, drag damping is most important in severe seas.

Sizing, spacing and number of heave plates are the major design parameters for obtaining the required heave period for the structure. Prislin et al., (1998) experimentally studied the variation of the natural heave period with the variation of number of heave plates and spacing. The results of their experiments indicate that as plate spacing increases, the added mass per plate also increases and closes to the value of added mass of a single plate. Increasing the total number of plates within a constant height decreases the added mass per plate. The drag coefficient per plate remains same for constant plate

spacing regardless of the total number of plates. Typically the number of heave plates used for a truss spar in Gulf of Mexico is 2 to 3.

1.2.3 Coupled Dynamic Analysis of Truss Spars

An integrated floating structure consists of a mooring system, riser system and a floating platform. When the integrated system is in motion, its three components (mooring, risers and platform) dynamically interact with each other. In deep water, their interactions are significant hence their motions and forces should be analyzed together, which is known as coupled dynamic analysis.

A traditional and simplified way of solving the dynamics of floating systems is to employ an uncoupled method, which ignores all or part of the dynamic interactions between a platform and its mooring lines and risers. As the water depth of offshore fields is getting deeper, mooring lines and risers become longer and heavier and uncoupled analysis methods may lead to inaccurate results. Thus, coupled dynamic analysis of a floating platform system becomes necessary with increasing water depth and in a coupled analysis the dynamic equations of motion of the hull and mooring/tendon/riser system are solved simultaneously.

For hull structures composed only of slender members (relative to the wave length), such as a truss spar, Morison equation may be used to compute the wave and current loads. Accurate wave kinematics is crucial to render accurate wave loads in the use of the Morison equation. Wave kinematics can be computed using many different wave models, such as second-order wave theory, Wheeler Stretching, linear extrapolation and Hybrid Wave Models (HWM). Hybrid Wave Models are accurate at least up to second order in wave steepness as they use two different perturbation schemes (conventional wave perturbation and phase modulation perturbation) to reach fast convergence of a truncated perturbation solution for a wave field of a broad-banded wave spectrum. They were proved to be very accurate through the comparison with both field and laboratory measurements (Ye, 1994, Zhang et al. 1996, 1997).

Time domain coupled dynamic analysis is usually much more accurate than the quasi-static approach in predicting the hull motions and mooring line tensions. However,

it is also computationally intensive, which hinders its application as a common design tool. A simulation of a moored floating structure for duration of three hours (prototype scale) may take much longer time to perform using a time domain coupled analyses. In practice, a mooring-line/riser system involves many mooring lines and risers. Therefore, the CPU time consumed for computing mooring-line and riser dynamics is considerably large and efficiency of numerical codes becomes very important.

A coupled dynamic analysis program called COUPLE, which is applicable to floating structures, was developed and a code for cable dynamics, called CABLE3D, was modified by improving numerical scheme and expanding it to allow for a relatively large extension in a cable (Chen, 2002). COUPLE has two options for modeling mooring/tendon/riser system, namely, quasi-static and coupled dynamic approach. Recently, COUPLE also takes into account the current load, wind load and VIV (Vortex Induced Vibration) effects (Ding et al, 2003).

1.3 Objective and Scope of This Study

The Horn Mountain truss spar was deployed in the Gulf of Mexico in 1,650 m of water depth, approximately 150 km southeast of New Orleans. Extensive field measurements were made using an integrated marine monitoring system attached to the truss spar. In this study, dynamic analysis of the truss spar interacting with its mooring and riser system is performed using 'COUPLE'. The simulated results are then compared with the corresponding field measurements made during Hurricane Isidore.

During the numerical simulation, various parameters of the truss spar which are crucial to the accuracy of predicting the global motions and tensions of the mooring lines and risers are scrutinized, such as the drag and added-mass coefficients of heave plates, hard tank and truss beams. Satisfactory agreement between the simulation and corresponding measurements is reached, indicating the numerical code, COUPLE, can be used to conduct the time-domain analysis of a truss spar interacting with its mooing and riser system under severe storm impact.

A comparative study was also conducted to analyze the significance of interaction of risers with the hull structure. Three different cases of coupled analysis were simulated, namely

- Coupled analysis of truss spar interacting with mooring lines only;
- Coupled analysis of truss spar interacting with the mooring lines and the steel catenary risers ;
- Coupled analysis of truss spar interacting with the mooring lines, the steel catenary risers and top tension risers.

Major statistical parameters of the global motions of the truss spar and the mooring line tensions are compared for theses cases.

A detailed study on the riser motions near to the touchdown area was also performed which includes the variation of the suspended length of steel catenary riser (SCR) and sensitivity of SCRs to surge, sway and heave motions of the truss spar.

2. SCENARIO

2.1 Description of the Truss Spar – Horn Mountain

2.1.1 Location of the Spar

The truss spar is deployed in the Horn mountain field (Halkyard et al, 2004) which is 160 kilometers south east of New Orleans as shown in Fig. 1. This field lies in Mississippi Canyon blocks 126 and 127 in 5425 ft deep water. Horn Mountain truss spar is operated by British Petroleum (B.P.). The production rate of the spar stands at an average of 65,000 barrels of oil and 68 million cubic feet of natural gas per day.

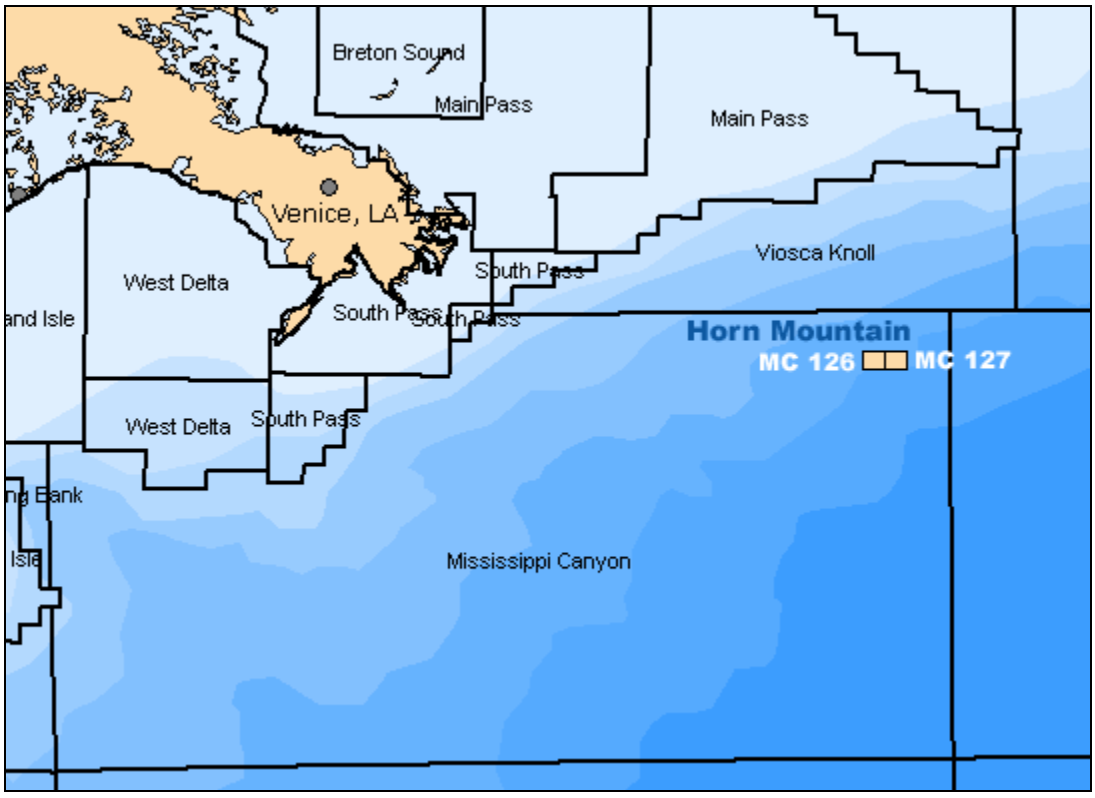

Fig. 1 Location of Horn Mountain Field

2.1.2 Main Particulars of the Spar

The main particulars of the Horn Mountain spar hull structure is given in the Table 1

Table 1 Main particulars of the truss spar

Total Length	169.16 m
Draft	153.924 m
Center of Buoyancy from Keel (KB)	107.69 m
Center of Gravity from Keel (KG)	90.39 m
Total Displacement	56,401.45 tonnes
Operating topside weight	4037 tonnes
Diameter of Hard Tank	32.31 m
Length of Hard Tank	68.88 m
Roll Gyradius	60.96 m
Pitch Gyradius	60.96 m
Yaw Gyradius	12.50 m

2.1.3 Structural Description of the Spar

The hull structure mainly consists of three sections. A 68.88m long and 32.31m diameter hard tank, 5m long and 32.31m diameter soft tank and a 96m long truss section connecting the soft tank and the hard tank. The truss section is divided into three subsections by means of heave plates. Each subsection consists of four vertical cylindrical legs at the corners, cross circular beams running diagonally and vertical braces. The soft tank is used for supporting solid ballast to improve the stability of the structure. In additions to this a cylindrical tank is attached on top of the soft tank, which can be ballasted to tow the structure in horizontal position. The hull structure is also

characterized with a 15.85m x 15.85m central well which is open to sea water. The structural details of the spar are shown in Fig. **2**.

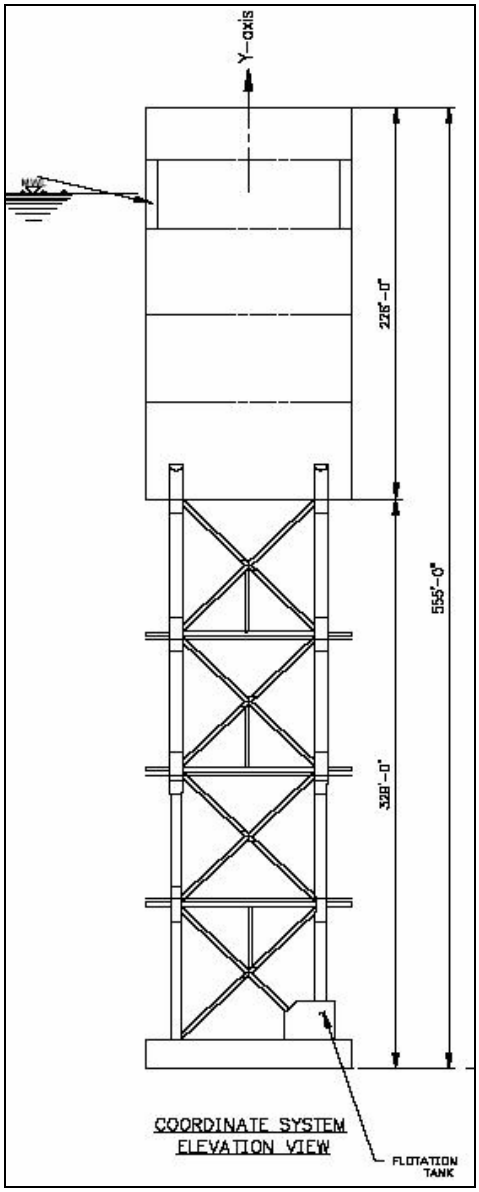

Fig. 2 Hull configuration

2.1.4 Mooring and Riser System of the Spar

The mooring system consists of three groups, each group having three semi taut chain-wire-chain mooring lines. They are connected to the hull through fairleads located 50 m below the water surface. The mooring line configuration is illustrated in Fig. 3 . Orientation of mooring lines with respect to the positive x-axis and the angle of line connecting fairlead and the center of the spar with respect to the positive x-axis are shown in the figure. The fairleads located at a water depth of 50m on the hard tank. The mooring line characteristics are given in Table 2. The pretension at the time of installation in each of the mooring lines is given in Table 3.

Table 2 Mooring line properties

Line Properties		**Unit**	**Fairlead chain**	**Riser wire**	**Ground chain**
Type			R4 Studless	Spiral Strand	R4 Studless
Length	Group 1 (#1, #2, #3)	m	82.3	2137.3	77.3
	Group 2 (#4, #5, #6)	m	82.3	2137.3	77.3
	Group3 (#7, #8, #9)	m	137.16	2137.3	77.3
Diameter		cm	14.61	12.8	14.61
Dry Weight		kg/m	453.30	86.46	453.30
Wet weight		kg/m	394.36	68.46	394.36
Minimum Breaking Load		kN	18887	15791	18887

The truss Spar has a wellbay which accomodates 14 production top tensioned riser (TTR) slots and 2 import steel catenary riser (SCR) well slots. The SCRs are

connected to the hull structure through porches which are located on the hull at a water depth of 50 m. The TTRs are carried through the keel of the vessel to the upper deck. Orientation of the steel catenary risers with respect to the positive x-axis is shown in Fig. 4. The properties of the risers are given in Table 4.

Table 3 Mooring line pretensions

Mooring Line No.	**Pretension (kN)**
1	2348.7
2	2348.7
3	2357.6
4	2682.3
5	2700.1
6	2709.0
7	2833.5
8	2846.9
9	2846.9

Table 4 Properties of risers

Characteristics	**Unit**	**SCR 1**	**SCR 2**	**TTR**
Length	m	3352.8	3352.8	1500
Diameter	cm	0.3048	0.254	0.3048
Dry Weight	Kg/m	97.743	56.699	97.743
Unit Buoyancy	Kg/m	75.15	52.19	75.15

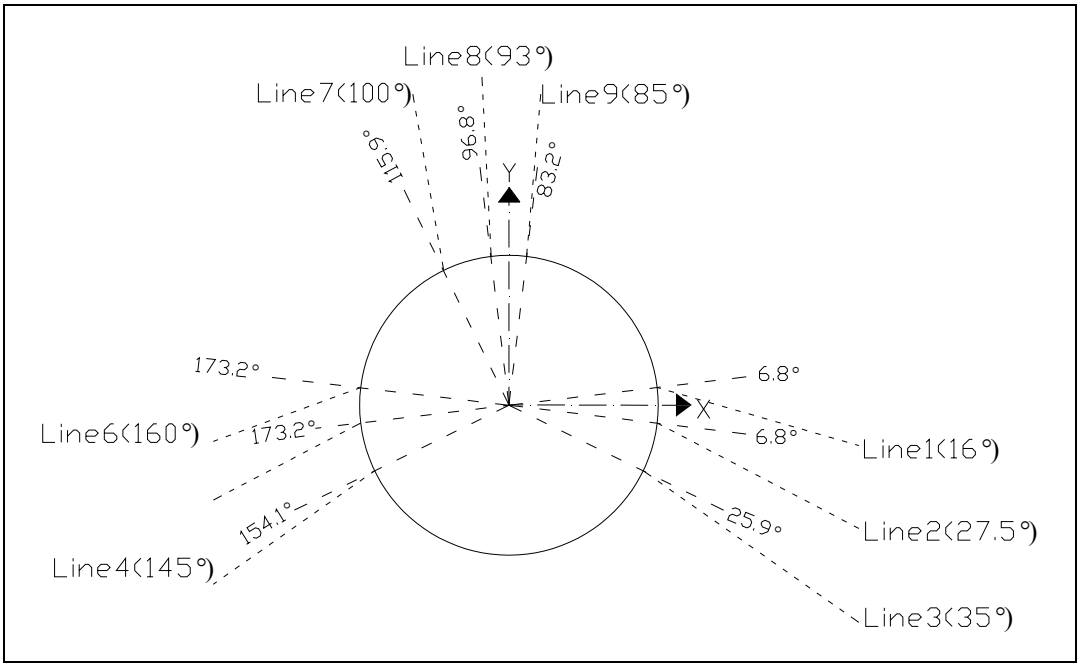

Fig. 3 Mooring system configuration

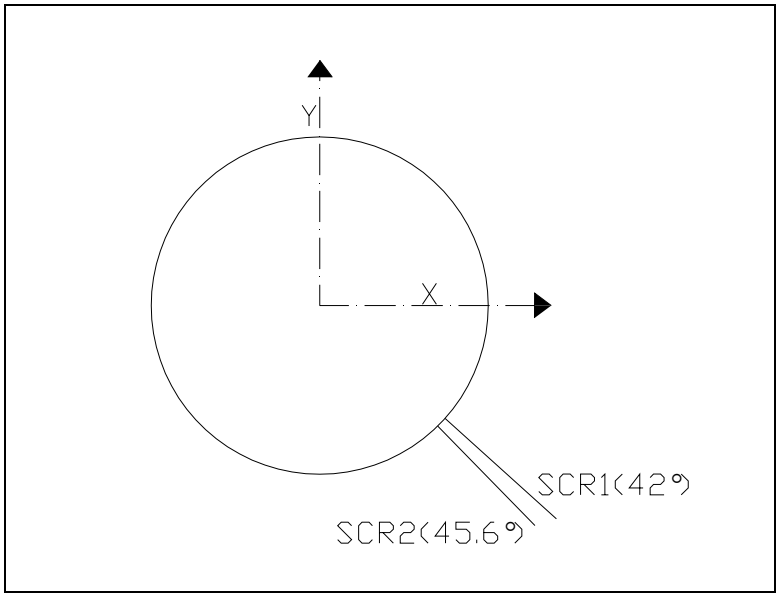

Fig. 4 Steel catenary risers configuration

2.2 Description of the Event- Hurricane Isidore

The Hurricane Isidore started as a tropical depression at 1200 Coordinated Universal Time (UTC) on 17th September 2002, about 120 nautical miles south of Kingston, Jamaica (Avila L., 2002). The depression became Tropical Storm Isidore around 0600 UTC on 18th September, and, embedded within a weak steering current. The tropical cyclone moved very slowly toward the northwest, passing just west of Jamaica. Isidore then moved very slowly toward the west-northwest across the Cayman Islands and became a hurricane at 1800 UTC on 19th September. Its winds reached 90 knots around 0600 UTC on 20th September as it was nearing the southwest coast of the Isle of Youth, Cuba. Isidore attained a category 1 (on the Saffir-Simpson Hurricane Scale) hurricane status when it hit western Cuba. It gained strength and hit the coast of northern Yucatan Peninsula as a category 3 hurricane. The maximum intensity reached was 110 knots at 1800 UTC on 21st September. Isidore reduced its intensity over Yucatan Peninsula before moving northward over the Gulf of Mexico where the circulation expanded but the cyclone never redeveloped an inner core of strong winds. Isidore made landfall with winds of 55 knots and a minimum pressure of 984 millibar just west of Grand Isle, Louisiana at 0600 UTC on 26th September. The Hurricane passed over the Horn Mountain for a duration of 5 hours between 1900 hrs to 2400 hrs on September 25th . The path of the hurricane is shown in Fig. 5.

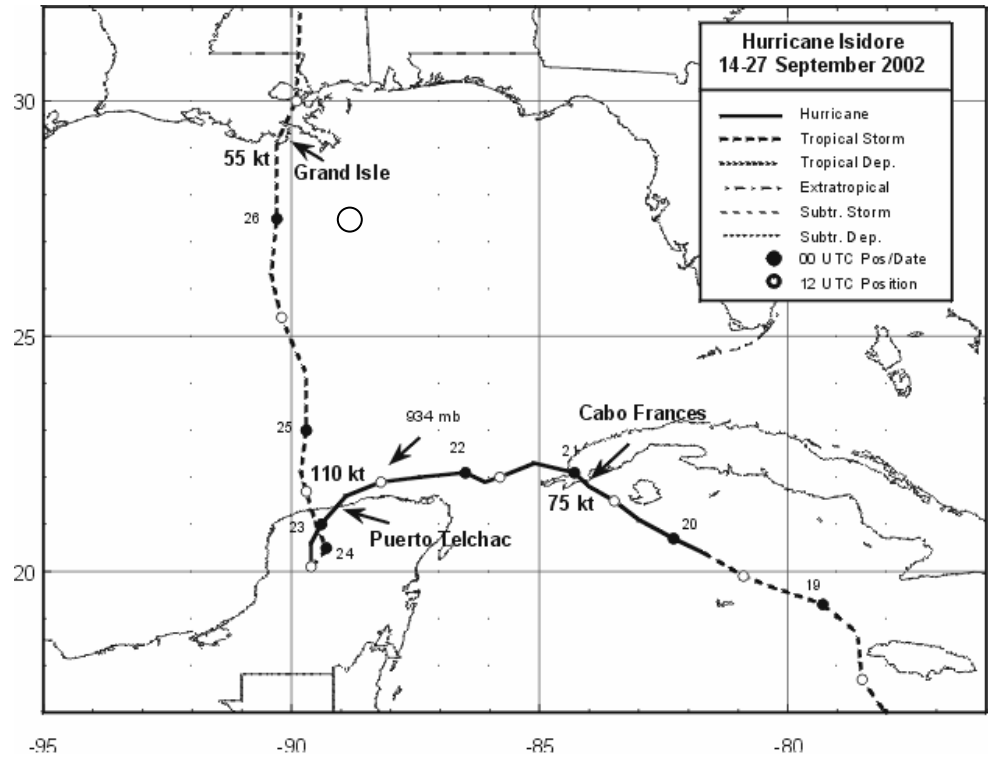

Fig. 5 The path of Hurricane Isidore (courtesy NHC)

('O' Indicates the position of Horn Mountain spar)

3. FULL SCALE DATA ANALYSIS

3.1 Collection of the Full Scale Measurements

The Integrated Marine Monitoring System (IMMS) installed on the Horn Mountain Spar and the National Data Buoy Center (NDBC) are the main sources for obtaining the full scale measurements of global motions of the hull, mooring line tensions, riser tensions and metocean data.

3.1.1 Integrated Marine Monitoring System (IMMS)

An Integrated Marine Monitoring System (IMMS) is a comprehensive monitoring system for collecting and displaying real-time information of the various characteristics of the spar (Edwards 2003). This IMMS is designed to monitor, log and display:

- Production Riser Tension
- Production Riser Buoyancy Can Pressure, Total Buoyancy and Stroke
- Platform Position (GPS signals)
- Trim, Heel, Roll and Pitch
- 3 Linear accelerations and 3 angular velocities
- Draft
- Wind Speed and Direction
- Air Temperature and Barometric Pressure
- Wave Heights
- Ballast Tank Status
- Current Profile, between 140 feet below MSL and 1300 feet below MSL
- Mooring Line Tensions and Payout

The IMMS data is stored on the platform both on hard disk and on magneto optical disks. Measured data is electronically mailed to the data processing center on shore for further analysis.

3.1.2 National Data Buoy Center (NDBC)

The wave measurements obtained from the IMMS are compared with the measurements obtained from NDBC data buoys 42040 and 42039 (NOAA archives). These are located in close proximity to the Horn mountain spar. The location of the data buoys relative to the spar is shown in Fig. 6. From the figure it is clear that the NDBC station 42040 is more close to the location of the spar than buoy 42039. Hence we select the metocean data given by the station 42040 which is given in Table 5.

3.1.2.1 Description of the Particulars of NDBC Measurements

The date/time is of the form, 'YYYY MM DD hh', which represents the year, month, day and hour of the measurement in Greenwich Mean Time (GMT), which is five hours ahead of Eastern Standard Time of United States. WD is the dominant wind direction (the direction from which the wind is coming in degrees, clockwise from true N). WSP is wind speed (m/s) averaged over an eight-minute period. GST is the wind gust given in knots. WVHT is the significant wave height in meters. DPD stands for dominant wave period (seconds) and is the period with the maximum wave energy. APD is the average wave period (seconds) of all waves during the 20-minute period. MWD, mean wave direction corresponds to energy of the dominant wave period (DPD). The units are in degrees from true North defined in the same way as the wind direction.

Fig. 6 Location of the Spar and Buoys 42040 and 42039

('O' denotes the spar, 'Δ'denotes 42040 and ' ◺' denotes 42039)

Table 5 Metocean data from NDBC station 42040

YYYY	MM	DD	hh	WD	WSP	GST	WVHT	DPD	APD	MWD
2002	9	26	0	97	18.2	21.9	6	11.11	8.17	164
2002	9	26	1	111	17.1	23.8	6.78	10	8.56	148
2002	9	26	2	113	15.4	18.9	6.11	12.5	7.97	170
2002	9	26	3	122	16.4	21.8	6.27	11.11	8.08	161
2002	9	26	4	122	18.6	22.8	7.12	12.5	8.35	161

3.2 Processing the Full Scale Measurements

3.2.1 Errors and Discrepancies in the Measurements

Measurements are never perfect, and we can always expect measurement errors in the data. The errors in the measurement of IMMS are caused mainly due to low frequency instrumentation drifts and high frequency noise components. Instrument drift errors are results from a gradual and unintentional change in the reference value with respect to which the measurements are made. Although most of the measurement devices are constructed to high-precision standards, they are subject to drifts due to changes in properties of the materials used in the instrument and due to variation of temperature of the working environment.

Another important source of errors in measurements is noise. There are various sources of noise in electronic components. The most fundamental one is due to the random motions of electrons in a conductor. The random motion corresponds to a fluctuating current, and this current will develop a voltage across the resistance of the conductor.

Band pass filters are used to remove the low frequency drift components and high frequency noise components from the measurements. There are various filtering methods available like Bessel filter, Butterworth filter, Chebyshev method and Elliptic filter. A Butterworth digital filtering method (MATLAB 7.0.1, 2004), which is characterized by a unit magnitude response that is almost flat in the band pass, is used. 'Filtfilt' (MATLAB 7.0.1, 2004) function is also used to perform zero phase digital filtering by processing the data in both the forward and backward directions.

3.2.2 Processing the Rotations

The three angular motions of the spar structure namely roll, pitch and yaw are obtained by integrating the measured angular velocities. Prior to integration, the angular velocities are filtered to obtain signals in a frequency range of 0.01Hz to 0.2 Hz. A comparison of raw data and filtered data of roll rates are given in Fig. 7 and Fig. 8 . We

can see from Fig. 7 that the mean drift and the noise component in the raw data are removed in the processed data. A similar process is followed for pitch and the yaw rates.

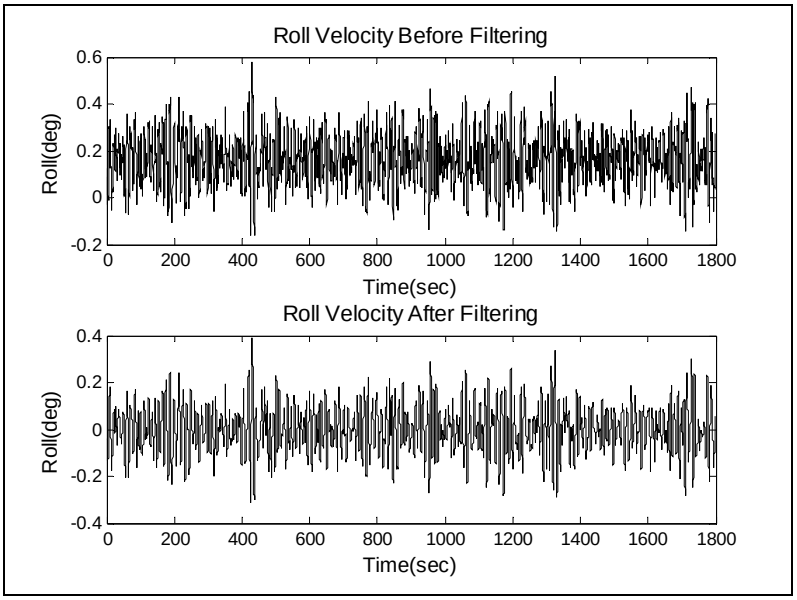

Fig. 7 Comparison of time series before filtering and after filtering

3.2.2.1 Estimation of the Mean Value of Roll and Pitch from Linear Translations

When the spar platform is subjected to small angles of roll and pitch a component of gravitational acceleration occurs in the sway and surge accelerations respectively. Hence we can obtain the mean values of roll and pitch by the equations given (3.1) and (3.2)

$$\beta_m = \frac{\ddot{x}_m}{g} \tag{3.1}$$

$$\alpha_m = \frac{\ddot{y}_m}{g} \tag{3.2}$$

where

$\ddot{x}_m$: mean of surge acceleration

$\ddot{y}_m$: mean of sway acceleration

α_m : mean of roll

β_m : mean of pitch

g : acceleration due to gravity

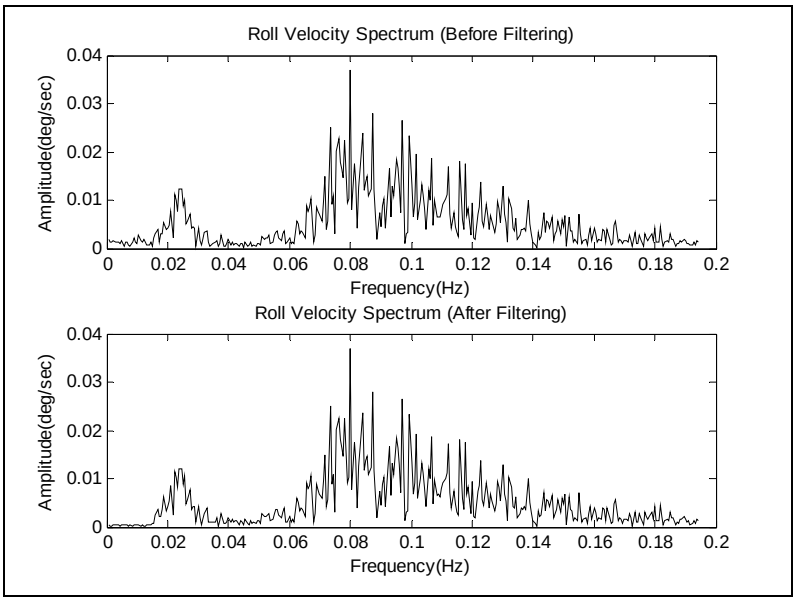

Fig. 8 Comparison of spectrum of raw data and filtered data

3.2.2.2 Integration of Angular Velocities to Obtain the Rotations

The angular velocities have to be integrated once to obtain rotation. The integration is done using Matlab function 'Quadl' (MATLAB 7.0.1, 2004). In this method the time series of angular velocities are fitted by cubic polynomials and these polynomial functions are integrated in each time step. The accuracy of this method is checked by comparing the differentiated rotations with the measured angular velocities. This difference between the above two values for a 30-minutes duration of roll rate

measurements is shown in Fig. 9. The maximum value of the percentage difference is 2.38, which is well within the accuracy limit.

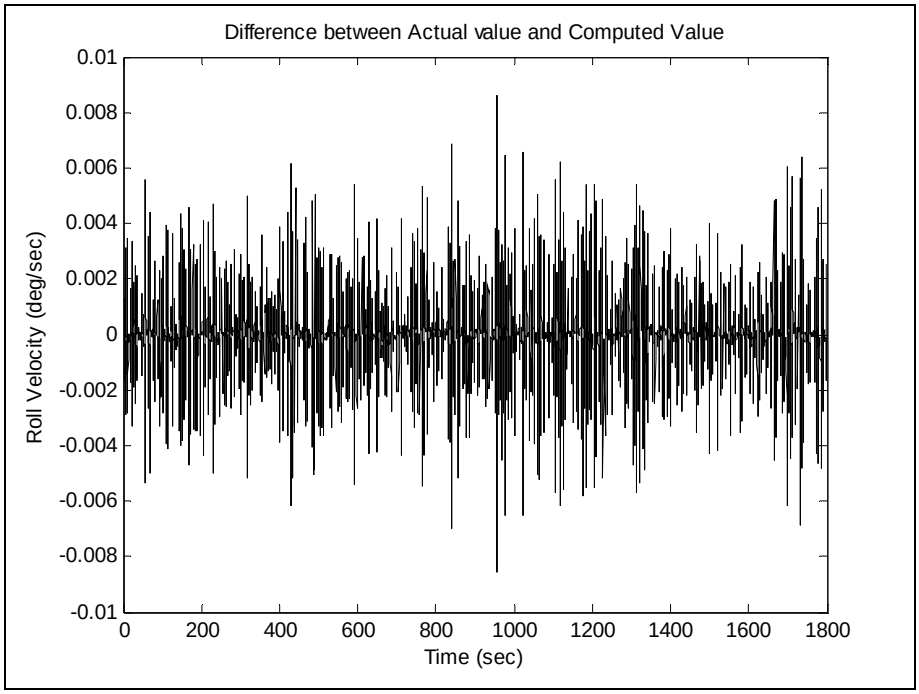

Fig. 9 Difference of roll velocities

3.2.3 Processing Translations

Linear translations mainly consist of two components: high frequency linear translations obtained by double integrating accelerations and low frequency linear translations obtained from GPS signals. Linear translation acceleration measurements are affected by the presence of components of gravity due to pitch and roll motions of the spar. These gravity components must be removed from the linear translations prior to further processing.

The following equations are used to remove the gravity components from the measured accelerations

$$\ddot{x}_f = \ddot{x}_i - g\sin(\beta)$$

$$\ddot{y}_f = \ddot{y}_i - g\sin(\alpha)$$

$$\ddot{z}_f = \ddot{z}_i - g\cos(\alpha)\cos(\beta)$$

where $\ddot{x}_f$: surge acceleration without gravity

$\ddot{y}_f$: sway acceleration without gravity

$\ddot{z}_f$: heave acceleration without gravity

$\ddot{x}_i$: surge acceleration with gravity

$\ddot{y}_i$: sway acceleration with gravity

$\ddot{z}_i$: heave acceleration with gravity

α and β are roll and pitch respectively.

After removing the gravity components, the measured translation accelerations are numerically filtered to remove low frequency and noise components to obtain a bandwidth frequency range of 0.06Hz to 0.2Hz. This process is illustrated in Fig. 10. The GPS signals for the surge and sway directions are low pass filtered to remove noise components. The processed GPS signals have a maximum frequency of 0.06Hz. This filtering is shown in Fig. 11.

The filtered high frequency linear accelerations are integrated twice by using the same method used for integrating angular velocities. Theoretically we should be able to obtain the measured acceleration values by differentiating twice the computed surge motions. So the accuracy of integration can be checked by taking the difference between computed values of acceleration and corresponding measured values .This difference for surge acceleration is shown in Fig. 12. Percentage of difference of the maximum value with respect to the actual value is 3.15, which is well within the accuracy limit.

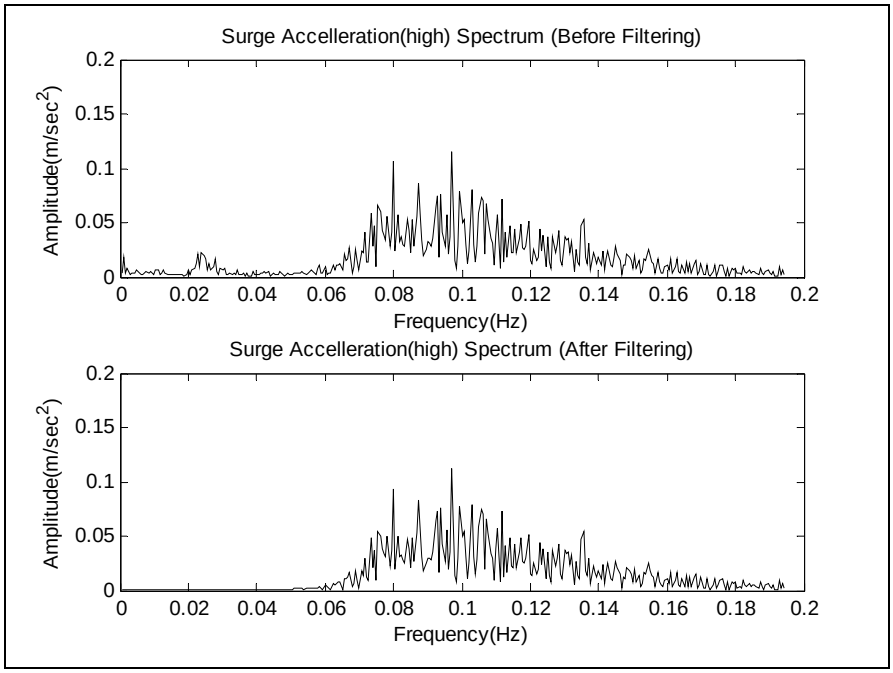

Fig. 10 Comparison of spectrums of surge accelerations before and after filtering

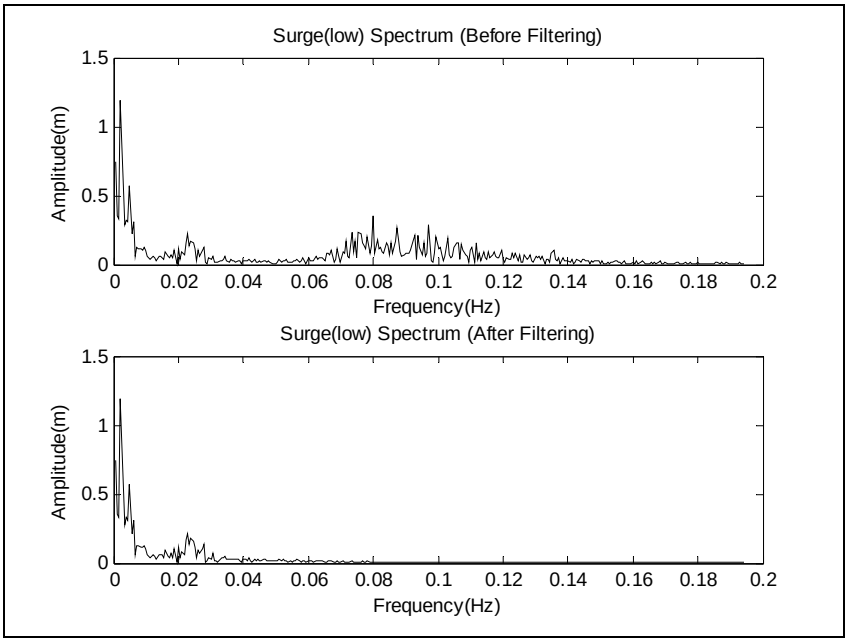

Fig. 11 Comparison of surge spectrums before and after filtering

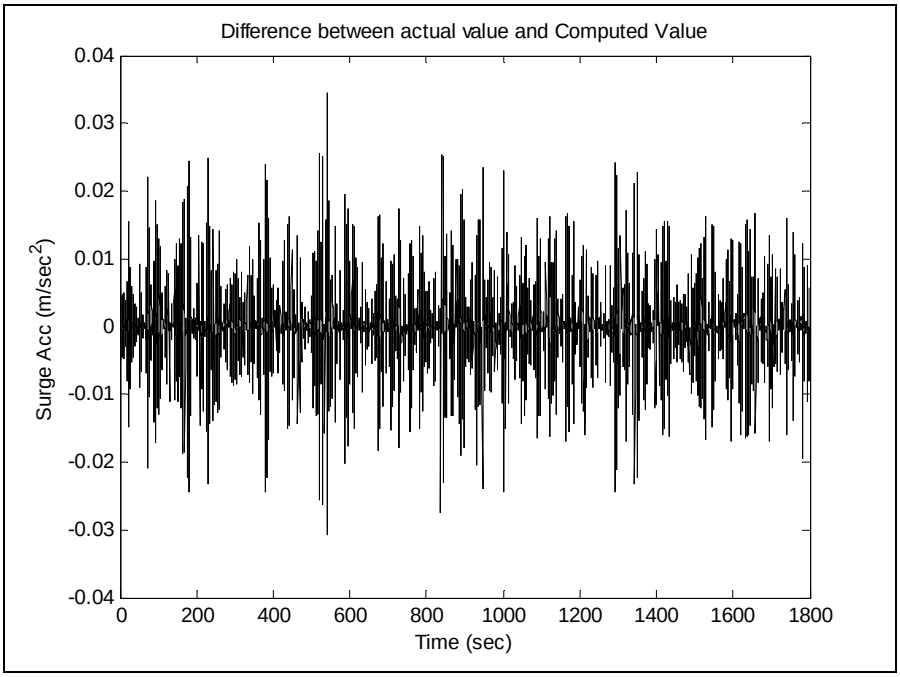

Fig. 12 Difference between surge accelerations

3.2.3.1 Superposing High Frequency and Low Frequency Components

After integrating the linear translation accelerations in surge and sway directions, they are superimposed with the corresponding low frequency components obtained from GPS measurements. The method is demonstrated in Fig. 13., the low frequency components are up to 0.06 Hz while the high frequency components range from 0.06 Hz to 0.2 Hz.

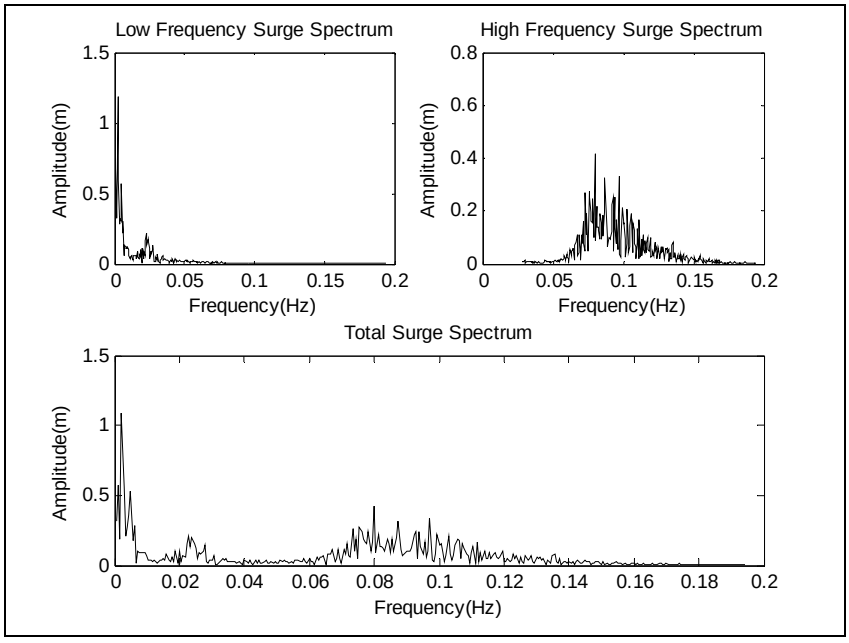

Fig. 13 Superimposing the low and high frequency components

The low frequency components of heave are obtained from the measurements of the draft of the hull. They are up to a maximum frequency of 0.05 Hz. They are superimposed on the corresponding high frequency components having a frequency range of 0.05 Hz to 0.2 Hz.

Final plots of amplitude spectra and time series of all 6 global motions are shown in Fig. 14 through Fig. 25.

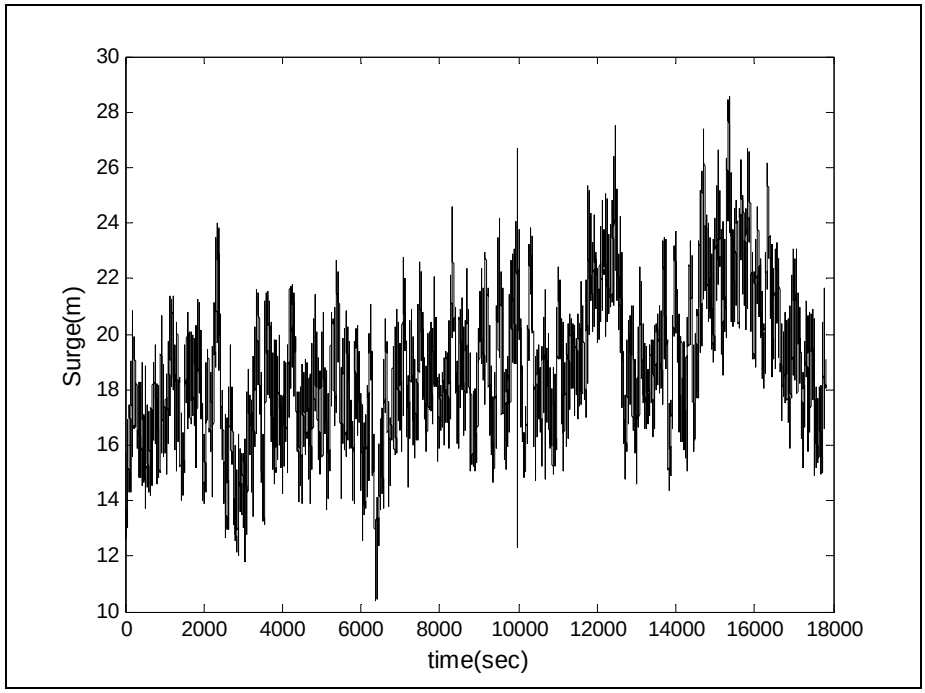

Fig. 14 Time series of surge motions during Hurricane Isidore

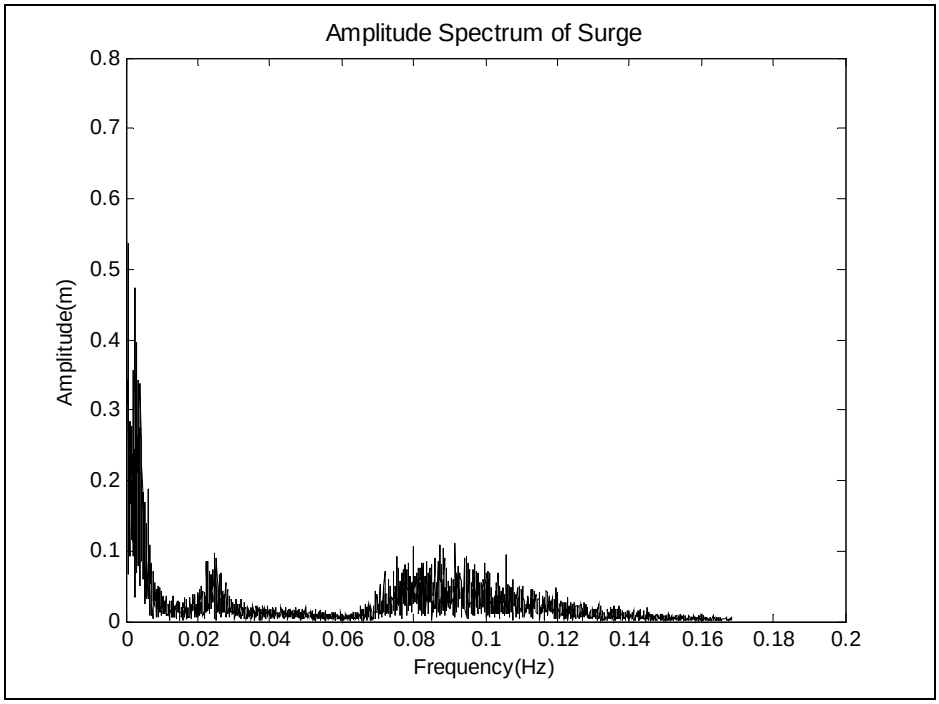

Fig. 15 Amplitude spectrum of surge motions during Hurricane Isidore

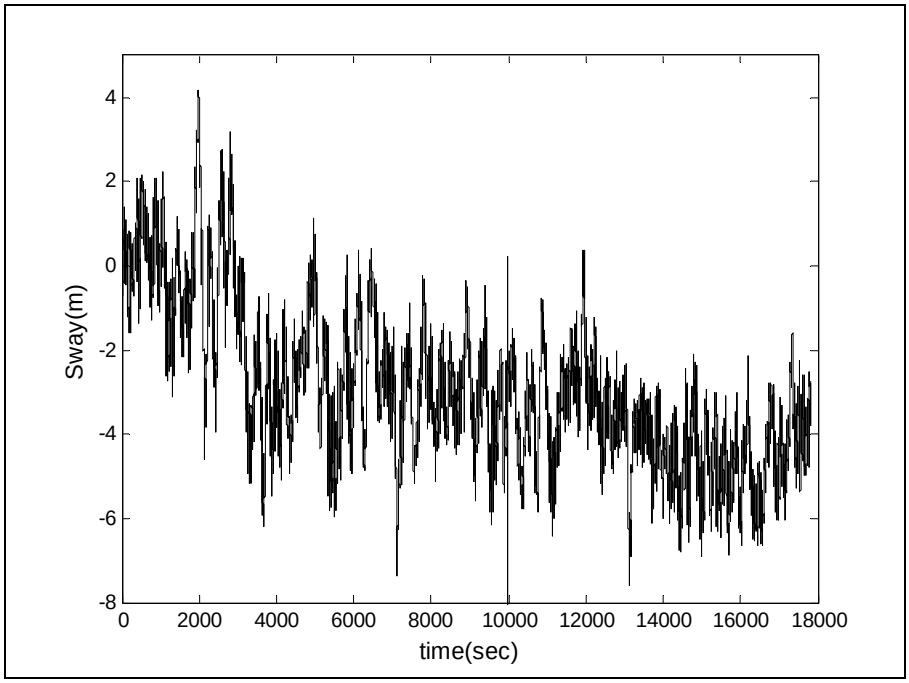

Fig 16 Time series of sway motions during Hurricane Isidore

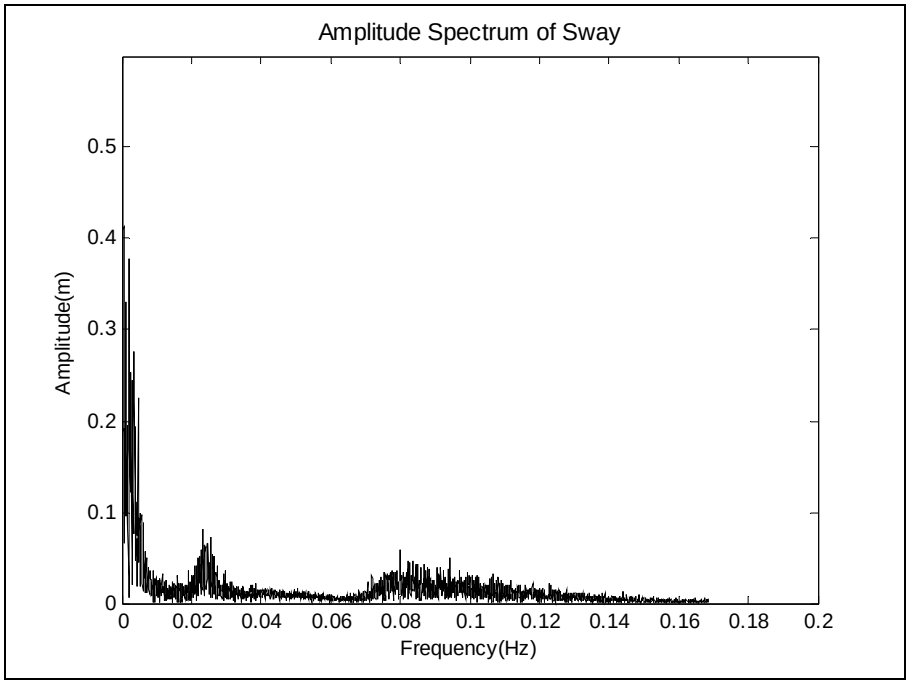

Fig 17 Amplitude spectrum of sway motions during Hurricane Isidore

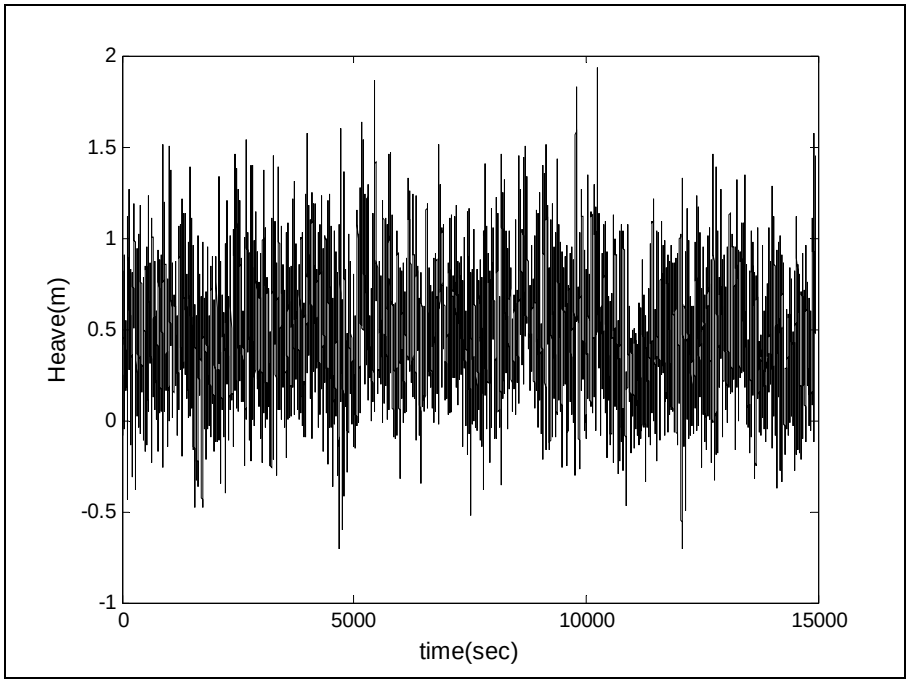

Fig 18 Time series of heave motions during Hurricane Isidore

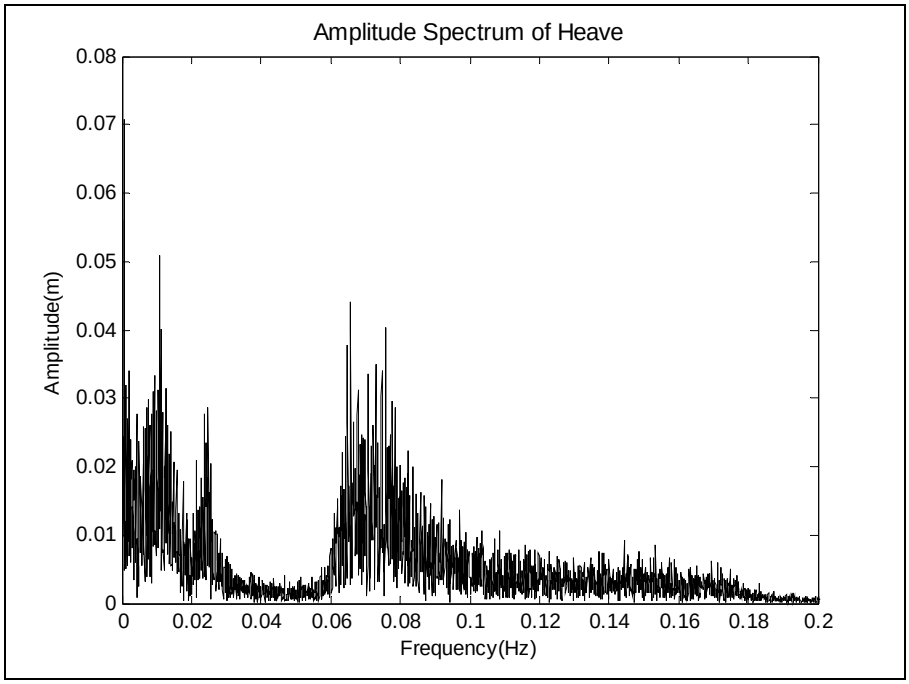

Fig 19 Amplitude spectrum of heave motions during Hurricane Isidore

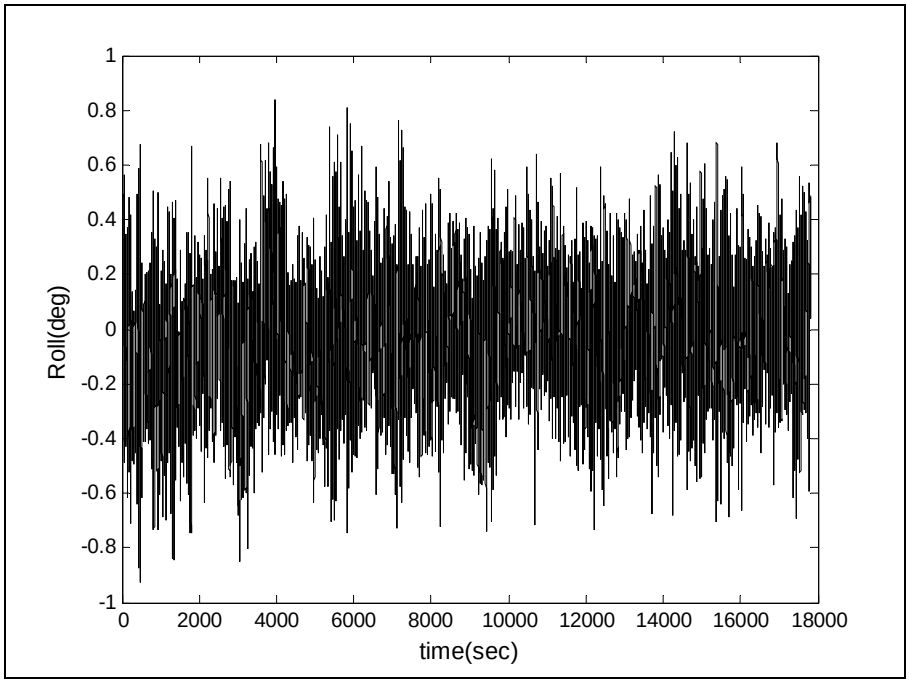

Fig 20 Time series of roll motions during Hurricane Isidore

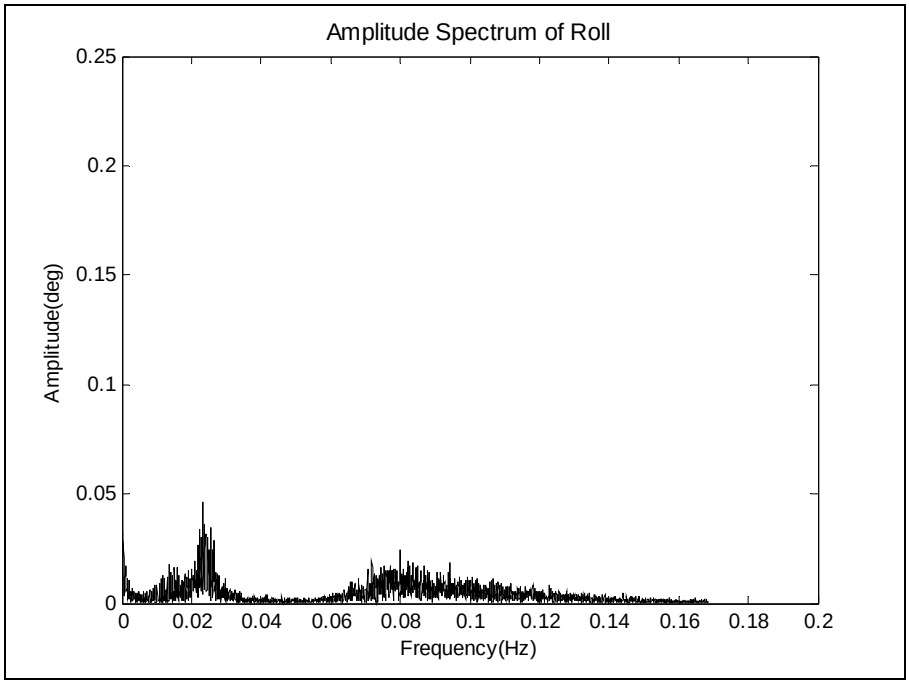

Fig 21 Amplitude spectrum of roll motions during Hurricane Isidore

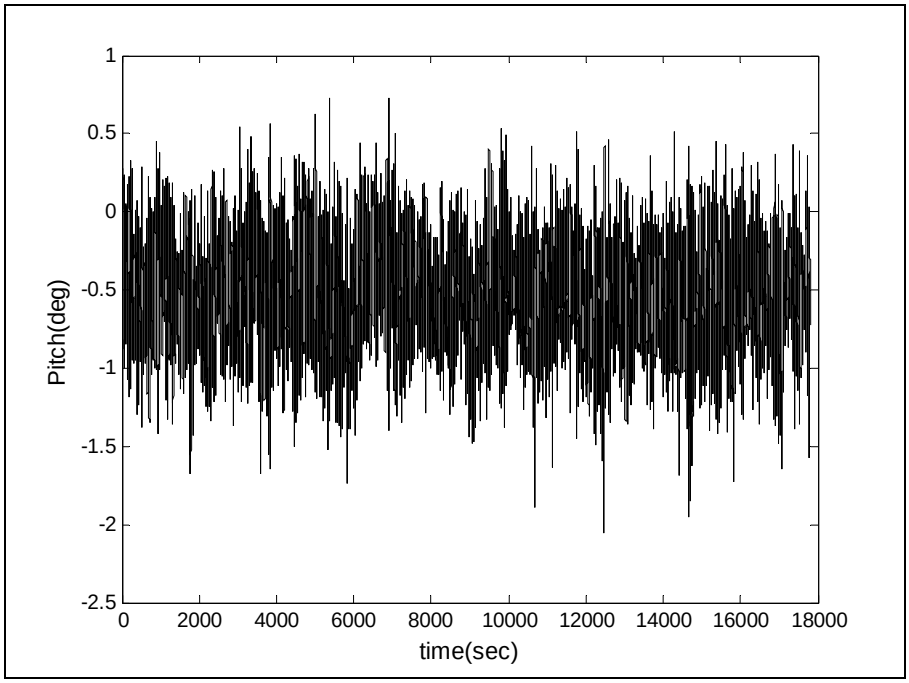

Fig 22 Time series of pitch motions during Hurricane Isidore

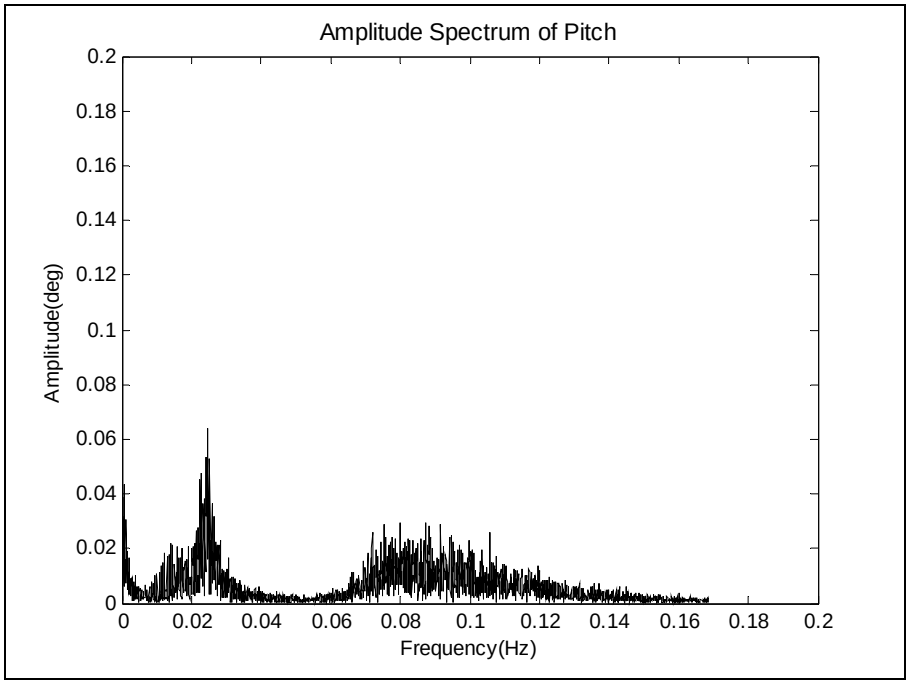

Fig. 23 Amplitude spectrum of pitch motions during Hurricane Isidore

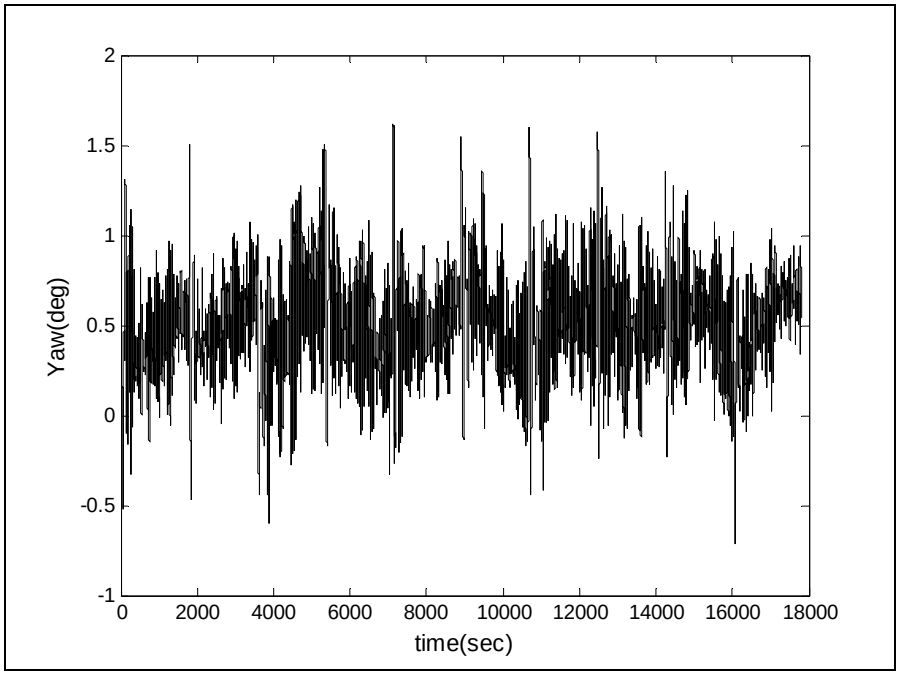

Fig. 24 Time series of yaw motions during Hurricane Isidore

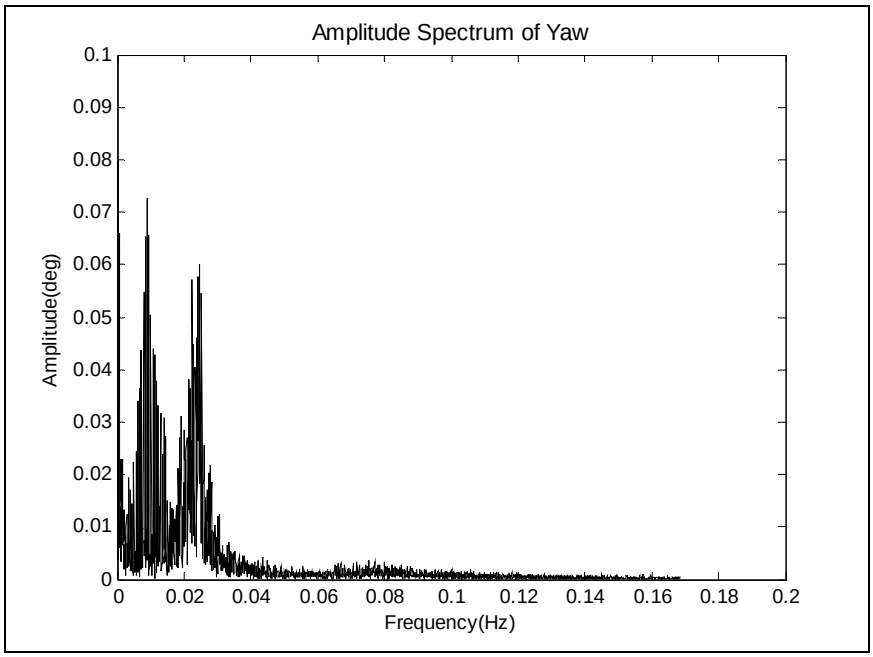

Fig. 25 Amplitude spectrum of yaw motions during Hurricane Isidore

A close scrutiny of Fig. 14 and Fig 16 reveals the fact that the mean of surge and sway varies during the five hour storm period. This is mainly due to the variation of wind and wave directions, which is clear from the NDBC measurements provided in Table 5. Wave directions vary from 97° to 122°, while the wind directions varies from 148° to 170° during the storm. It is difficult to numerically simulate time varying multi directional wind and wave conditions; therefore 30 minute duration of the storm having constant wind and wave directions is selected for comparison with the simulated values. The selected time period of storm is from 2110hrs to 2140hrs on 26th September 2002, Eastern Standard Time of U.S (from 7800 sec to 9600 sec on Fig. 14, Fig 16, Fig 18, Fig 20, Fig 22 and Fig. 24). During this time period we can see from Fig. 14 and Fig 16 that the surge and sway motions have a reasonably constant mean.

We can see from the amplitude spectrum of surge in Fig. 15 that there is significant slow drift motions at the natural frequency of surge (0.0035Hz), which is a typical phenomenon of spar platforms. Apart from this there is a significant surge motion at the wave frequency of 0.082Hz. The coupling effect of pitch motions in surge motions is also evident in the figure at the pitch natural frequency of 0.025Hz.

The amplitude spectrum of sway shown in Fig 17 is very similar to the surge spectrum. The coupling effect of roll motions in sway motions is evident at the roll natural frequency of 0.024Hz. Slow drift motions and wave frequency motions are also significant in the sway direction.

Even though the wave frequency motions are predominant in heave, significant resonant frequency motion also exists at 0.01Hz and 0.024 Hz. This peak at 0.024 Hz is due to the coupling effect of roll and pitch on heave.

Roll and pitch motions illustrated in Fig 21 and Fig. 23 respectively behave similarly. The resonant frequency motions of roll are evident at 0.024Hz and corresponding motion exists in pitch at 0.025Hz. Both spectra have significant peaks at the wave frequency.

Amplitude spectrum of yaw motions is illustrated in Fig. 25. Low frequency motions are predominant in yaw at its natural frequency (0.017Hz). There is a significant peak at 0.025 Hz due to the coupling effect of roll and pitch on yaw. The wave frequency motions are comparatively very low in yaw.

3.2.4 Processing Mooring Line Tensions

The mooring line tensions are low pass filtered to remove frequency noise components to get signals in the frequency range of 0 to 0.25Hz. The time series and amplitude spectrum of mooring line no.1 tensions are illustrated in Fig. 26 and Fig. 27.

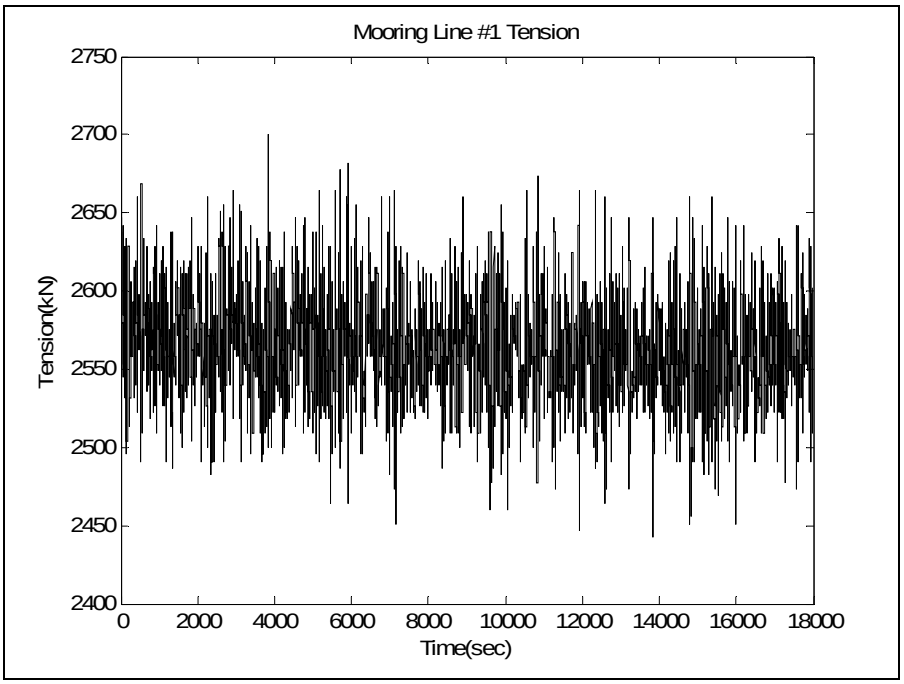

Fig. 26 Time series of mooring line #1 tension during Hurricane Isidore

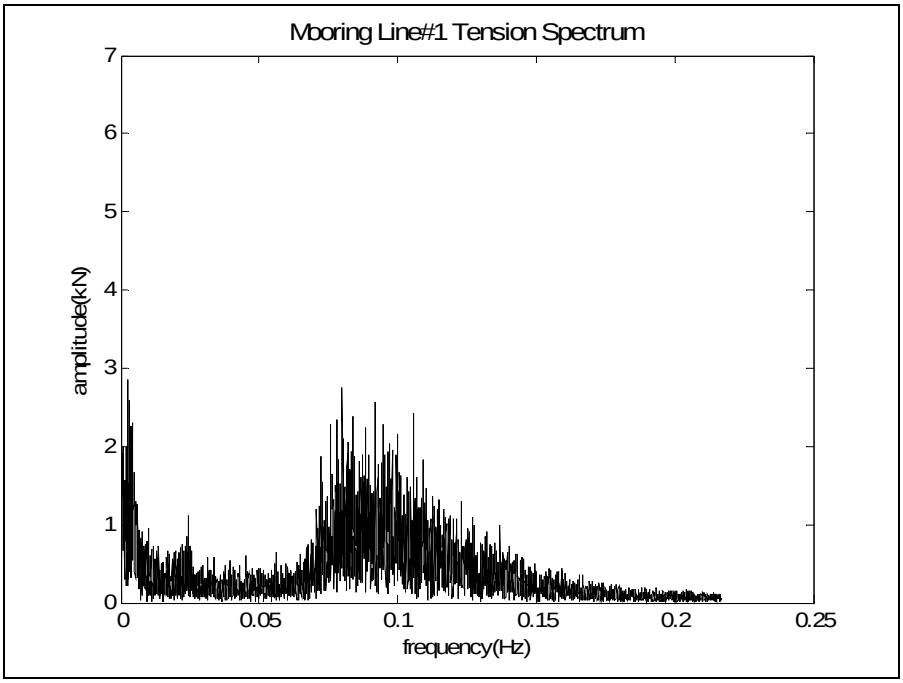

Fig. 27 Amplitude spectrum of mooring line #1 tension during Hurricane Isidore

3.2.5 Metocean Data

The wave and current measurements obtained from IMMS system is compared with the NDBC measurements. They were found to be similar. The final values of metocean conditions used for numerical simulation are shown in Table 6. For computation purposes we assume the current to be steady and the irregular waves to be unidirectional. In the numerical model, a JONSWAP spectrum is used to generate the irregular waves and an API wind spectrum is used for the generation of time varying wind force. Directions of the wind, wave and current are illustrated in Fig. 28. The shear current profile mostly prevalent at the time of Hurricane Isidore is shown in Fig. 29.

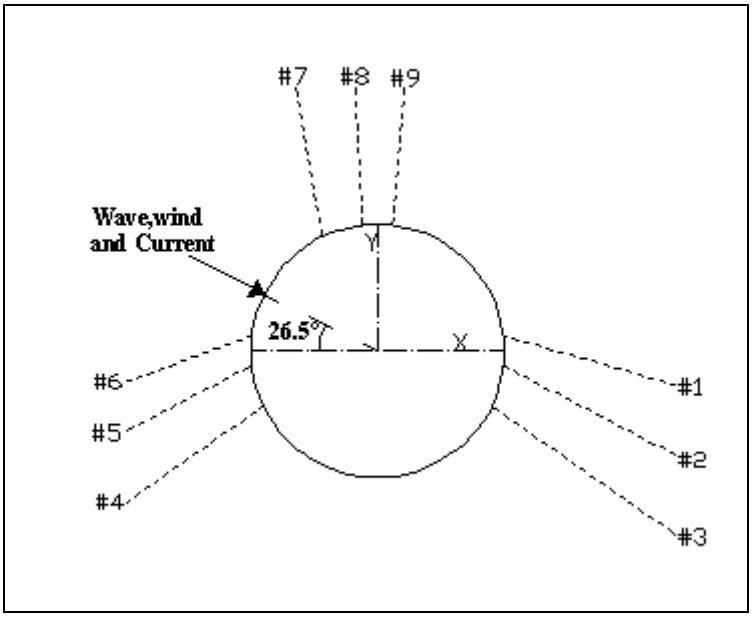

Fig. 28 Direction of current, wind and wave

Table 6 Metocean data

Wave	Hs (m)	6.3
	Tp (sec)	12.2
	Peak shape factor	1.3
Wind	Speed at 10m from sea level (m/sec)	19.3
Current	**Depth from water surface (m)**	**Speed (m/sec)**
	0	0.256
	-43.5864	0.201
	-59.7408	0.134
	-75.5904	0.253
	-107.594	0.186
	-171.602	0.104
	-251.765	0.037
	-363.626	0.073
	-1645.92	0.043

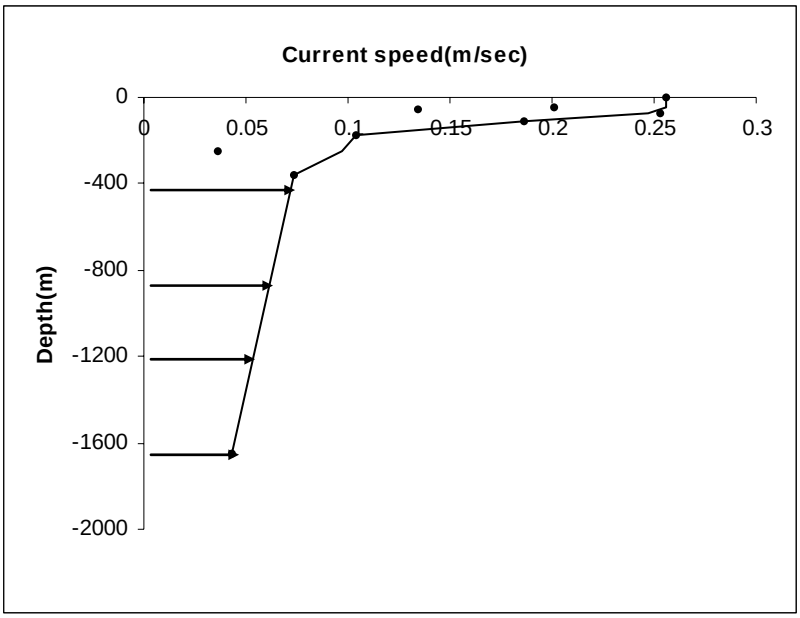

Fig. 29 Shear current profile

4. NUMERICAL SIMULATION

4.1 Modeling the Hull

Since the truss spar basically consists of slender members relative to the wavelength of the storm waves, the Morison equation is used to compute the drag and inertia forces on the hard tank, soft tank, floatation tank, truss elements, truss legs, heave plates and braces of the hull structure. In order to have high accuracy of the loads acting on the structure, a number of integration points are specified for each element. The vertical exciting forces on the heave plates are approximated by a set of thin disks to simulate the drag and inertia effects. The details of the added mass and drag coefficients used for the numerical simulations are given in Table 8 in section 4.5.

4.2 Modeling the Mooring Lines and Risers

Risers and mooring lines are modeled as extensible slender rods. The computation and understanding of dynamics of these structures require knowledge of nonlinearities arising from large deformation. In a classical theory of rods, the behavior of long bars is described in terms of the position of the centerline of the bar. The description of the motion equation of long bars in this study follows that presented by Nordgren (1974), Garrett (1982), Paulling and Webster (1986), Ma and Webster (1994) and Chen (2002).

4.2.1 Equation of Motions

Assuming no torque and applied external moment, one can derive the linear momentum conservation equation with respect to a position vector $\vec{r}(s,t)$ that is a function of arc length (s) and time (t).

$$-(B\mathbf{r}'')'' + (\lambda\mathbf{r}')' + \mathbf{q} = \rho\ddot{\mathbf{r}} \tag{4.1}$$

$$\lambda = T - B\kappa^2 \tag{4.2}$$

where r(s,t) is a position vector of s, the arc length (before deformation) along the rod, and time t, B the bending rigidity, λ Lagrange multiplier, $\vec{q}$ the distributed external

force per unit length, ρ the mass per unit length, $\vec{T}(s,t)$ the local tension and κ the local curvature of the rod. Prime and dot denote spatial derivative and time derivative, respectively.

The local tension is given by the equation (4.3) and the local curvature is given by the equation (4.4).

$$T(s,t) = \mathbf{r}' \cdot (-(B\mathbf{r}'')' + \lambda \mathbf{r}') \tag{4.3}$$

$$\kappa^2 = -\mathbf{r}' \cdot \mathbf{r}''' \tag{4.4}$$

If the rod is assumed to be inextensible, the following condition must be satisfied.

$$\mathbf{r}' \cdot \mathbf{r}' = 1 \tag{4.5}$$

The external forces $\vec{q}$ applied on a rod consist of gravitational, hydrostatic and hydrodynamic forces.

$$\begin{aligned} \vec{q} = &(\rho_f A_f - \rho_i A_i - \rho_t A_t) g e_y + \rho_f A_f (I + C_{Mn} N + C_{Mt} T) a_f \\ &+ \frac{1}{2} \rho_f D_f C_{Dn} N(v_f - \dot{r}) \left| N(v_f - \dot{r}) \right| \\ &+ \frac{1}{2} \rho_f D_f C_{Dt} T(v_f - \dot{r}) \left| T(v_f - \dot{r}) \right| \end{aligned} \tag{4.6}$$

In the above equations:

$\rho_f(s)$ = the mass density of the sea water,

$\rho_i(s)$ = the mass density of the fluid inside tube,

ρ_t(s) = the mass density of the tube,

$D_f(s)$ = the diameter of the rod,

$A_f(s)$ = the outer cross-section area of the rod,

$A_i(s)$ = the inner cross-section area of the rod,

$A_t(s)$ = the structural cross-section area of the rod,

$\mathbf{v}_f$ = the velocity of the sea water (current and wave),

$\mathbf{a}_f$ = the acceleration of the sea water (current and wave),

C_{Mn} = normal added-mass coefficient,

C_{Mt} = tangential added-mass coefficient,

C_{Dn} = normal drag coefficient,

C_{Dt} = tangential drag coefficient,

T, **N** = transfer matrices,

I = identity matrix,

where the subscripts *f*, *i* and *t* denote the sea water, the fluid inside the tube and the tube itself. **T** and **N** are defined by:

$$\mathbf{T} = \mathbf{r}'^{T}\mathbf{r}' \tag{4.7}$$

$$\mathbf{N} = \mathbf{I} - \mathbf{T} \tag{4.8}$$

In equations (4.1), (4.5). the unknowns are r and $\tilde{\lambda}$. The Procedures for the numerical implementation of above equations is detailed in Garret (1982). The Galerkins method is used to discretize the partial differential equations of motion for (4.1) and (4.5) in space. This method results in a set of nonlinear second order ordinary differential equations in time domain. Shape functions are used to solve them. The non linear differential equations are numerically integrated in the time domain using Newmark-β method (Argyris and Mlejnek (1991) , Wood (1990)).

4.3 Theory of Coupled Dynamic Analysis

4.3.1 6-DOF Nonlinear Motion Equations of a Rigid Body

The six Degree Of Freedom (6-DOF) nonlinear motion equations are derived for the hull structure. Hydrodynamic forces on the body are derived using the Morison equation. Wave kinematics used in the Morison equation are derived using the Hybrid Wave Model (HWM). These motion equations are coupled to the dynamic equations of slender rods through hinged boundary conditions. The static coupling problem is solved using Newton's method while the dynamic coupling method is solved using Newmark-β time integration scheme with an iterative procedure.

Two coordinate systems are employed in the derivation of motion equations of a floating rigid body as shown in Fig. 30. Coordinate system $\hat{o}\hat{x}\hat{y}\hat{z}$ is a space-fixed coordinate system, while *oxyz* is the body-fixed coordinate system moving with the body. The origin *o* can be the center of gravity or any point fixed on the body. The body-fixed coordinate *oxyz* coincides with $\hat{o}\hat{x}\hat{y}\hat{z}$ when the body is at its initial position. A third coordinate system *OXYZ* which is a spaced-fixed coordinate system with the *OXY* plan lying on the free surface and *Z*-axis positive upward is also introduced as a reference coordinate system. Incoming waves are shown in this space-fixed reference coordinate system.

Newton's second law may be written in terms of the rate of change of linear and angular momentum, respectively, as:

$$\frac{d\hat{\mathbf{L}}}{dt} = \hat{\mathbf{F}} \tag{4.9}$$

$$\frac{d\mathbf{H}_g}{dt} = \mathbf{M}_g \tag{4.10}$$

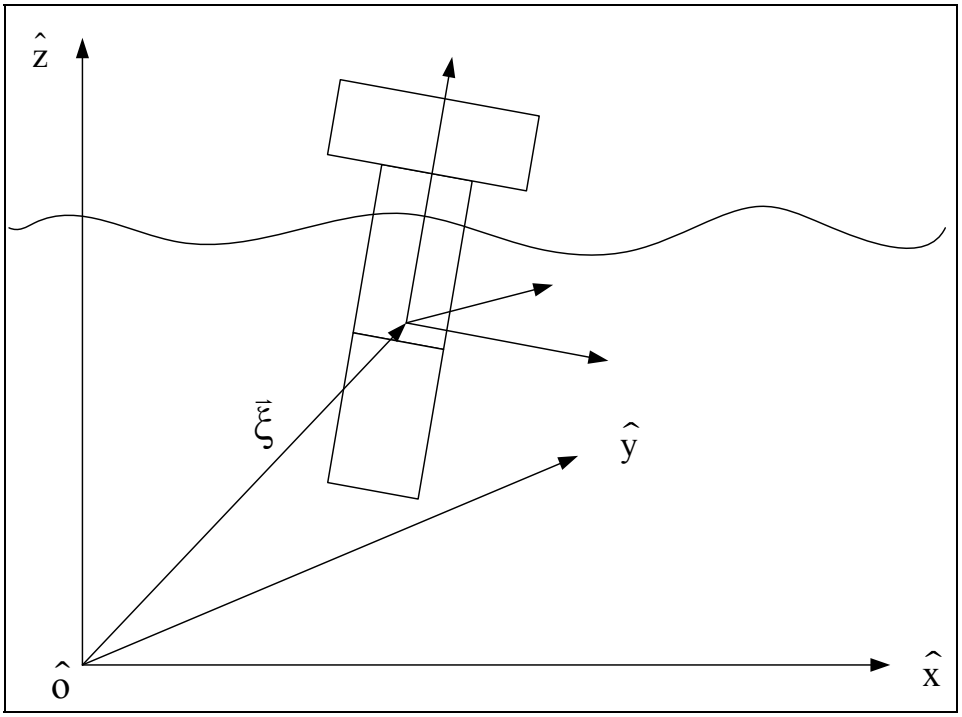

Fig. 30 Coordinate system for rigid body motions

The linear momentum $\hat{\mathbf{L}}$ is expressed as:

$$\hat{\mathbf{L}} = m\hat{\mathbf{v}}_g \tag{4.11}$$

where m is the mass of the rigid body, $\hat{\mathbf{v}}_g$ is the velocity of the center of gravity.

It is convenient to express $\mathbf{H}_g$ in the body-fixed coordinate system as shown in equation (4.12)

$$\mathbf{H}_g = \mathbf{I}_g\boldsymbol{\omega} \tag{4.12}$$

where $\mathbf{I}_g$ is the moment of inertia matrix with respect to center of gravity expressed in the body-fixed coordinate system *oxyz*. Vector $\boldsymbol{\omega}$ is the angular velocity also expressed in the body-fixed coordinate system *oxyz*. The relationship between $\boldsymbol{\omega}$ and the derivatives of the Euler angles is given by:

$$\boldsymbol{\omega} = \mathbf{B}\frac{d\boldsymbol{\alpha}}{dt} \tag{4.13}$$

where $\boldsymbol{\alpha} = (\alpha_1, \alpha_2\ \alpha_3)^t$ are the Euler angles in the roll-pitch-yaw sequence and

$$\mathbf{B} = \begin{bmatrix} \cos\alpha_3 \cos\alpha_2 & \sin\alpha_3 & 0 \\ -\sin\alpha_3 \cos\alpha_2 & \cos\alpha_3 & 0 \\ \sin\alpha_2 & 0 & 1 \end{bmatrix} \tag{4.14}$$

The relationship between $\frac{d\boldsymbol{\omega}}{dt}$ and the second derivatives of the Euler angles is given by:

$$\frac{d\boldsymbol{\omega}}{dt} = \mathbf{B}\frac{d^2\boldsymbol{\alpha}}{dt^2} + \boldsymbol{\alpha}_q \tag{4.15}$$

Where $\boldsymbol{\alpha}_q$ is given by equation (4.16).

$$\boldsymbol{\alpha}_q = \mathbf{Q}\frac{d\boldsymbol{\alpha}}{dt} = \begin{bmatrix} -\cos\alpha_3 \sin\alpha_2\alpha_{2t} - \sin\alpha_3 \cos\alpha_2\alpha_{3t} & \cos\alpha_3\alpha_{3t} & 0 \\ \sin\alpha_3 \sin\alpha_2\alpha_{2t} - \cos\alpha_3 \cos\alpha_2\alpha_{3t} & -\sin\alpha_3\alpha_{3t} & 0 \\ \cos\alpha_2\alpha_{2t} & 0 & 0 \end{bmatrix} \begin{Bmatrix} \alpha_{1t} \\ \alpha_{2t} \\ \alpha_{3t} \end{Bmatrix} \tag{4.16}$$

Then the translational and rotational motion equations are respectively given by:

$$m\hat{\mathbf{a}}_g = \hat{\mathbf{F}} \tag{4.17}$$

$$\mathbf{I}_g \frac{d\boldsymbol{\omega}}{dt} + \boldsymbol{\omega} \times \mathbf{I}_g\boldsymbol{\omega} = \mathbf{M}_g \tag{4.18}$$

where $\hat{\mathbf{a}}_g$ is the acceleration at the center of gravity and $\mathbf{M}_g$ is the moment defined with respect to the body-fixed coordinate system. Furthermore, more general motion equations with respect to *o* are derived. The acceleration at the center of gravity

expressed in the $\hat{o}\hat{x}\hat{y}\hat{z}$ coordinates is:

$$\hat{\mathbf{a}}_g = \hat{\mathbf{a}}_o + \mathbf{T}^t\left(\frac{d\boldsymbol{\omega}}{dt} \times \mathbf{r}_g + \boldsymbol{\omega} \times (\boldsymbol{\omega} \times \mathbf{r}_g)\right) \tag{4.19}$$

$$\mathbf{M}_g = \mathbf{M}_o - \mathbf{r}_g \times \mathbf{T}\hat{\mathbf{F}} \tag{4.20}$$

where

$\hat{\mathbf{a}}_o = \frac{d^2\boldsymbol{\xi}}{dt^2}$, is the acceleration at point *o* of the body expressed in $\hat{o}\hat{x}\hat{y}\hat{z}$,

$\boldsymbol{\xi} = (\xi_1, \xi_2, \xi_3)^t$, is the displacement at point *o* of the body expressed in $\hat{o}\hat{x}\hat{y}\hat{z}$,

$\boldsymbol{\omega} = (\omega_1, \omega_2, \omega_3)^t$, is the angular velocity expressed in *oxyz*,

$\mathbf{r}_g = (x_g, y_g, z_g)^t$, is the vector of the center of gravity (mass) of the body expressed in *oxyz*,

$\mathbf{I}_o$ is the moment of inertia of the body with respect to *o* expressed in *oxyz*,

$\hat{\mathbf{F}}$ is the total forces applied on the body expressed in $\hat{o}\hat{x}\hat{y}\hat{z}$,

$\mathbf{M}_o$ is the total moments with respect to *o,* origin of the *oxyz* coordinates

Substituting equations(4.19) and (4.20) into equations (4.17) and (4.18), we get the translational motion equations of a rigid body expressed in the $\hat{o}\hat{x}\hat{y}\hat{z}$ (spaced-fixed) coordinate system and the rotational motion equations expressed in the *oxyz* (body-fixed) coordinate system with respect to *o* as follows

$$m\frac{d^2\boldsymbol{\xi}}{dt^2} + m\mathbf{T}^t\left(\frac{d\boldsymbol{\omega}}{dt} \times \mathbf{r}_g\right) + m\mathbf{T}^t(\boldsymbol{\omega} \times (\boldsymbol{\omega} \times \mathbf{r}_g)) = \hat{\mathbf{F}} \tag{4.21}$$

$$\mathbf{I}_o\frac{d\boldsymbol{\omega}}{dt} + \boldsymbol{\omega} \times \mathbf{I}_o\boldsymbol{\omega} + m\mathbf{r}_g \times \left(\mathbf{T}\frac{d^2\boldsymbol{\xi}}{dt^2}\right) = \mathbf{M}_o \tag{4.22}$$

where

T is a transfer matrix between the body-fixed coordinate system and the space-fixed coordinate system expressed as:

$$\mathbf{T} = \begin{bmatrix} \cos\alpha_3 \cos\alpha_2 & \sin\alpha_3 \cos\alpha_1 + \cos\alpha_3 \sin\alpha_2 \sin\alpha_1 & \sin\alpha_3 \sin\alpha_1 - \cos\alpha_3 \sin\alpha_2 \cos\alpha_1 \\ -\sin\alpha_3 \cos\alpha_2 & \cos\alpha_3 \cos\alpha_1 - \sin\alpha_3 \sin\alpha_2 \sin\alpha_1 & \cos\alpha_3 \sin\alpha_1 + \sin\alpha_3 \sin\alpha_2 \cos\alpha_1 \\ \sin\alpha_2 & -\cos\alpha_2 \sin\alpha_1 & \cos\alpha_2 \cos\alpha_1 \end{bmatrix} \quad (4.23)$$

T is an orthogonal matrix with the property $\mathbf{T}^t=\mathbf{T}^{-1}$.

The relationship between space-fixed coordinates $\hat{\boldsymbol{X}} = (\hat{x}, \hat{y}, \hat{z})^t$ and body-fixed coordinates $\boldsymbol{X} = (x, y, z)^t$ is given by the equation

$$\hat{\boldsymbol{X}} = \boldsymbol{\xi} + \mathbf{T}^t \boldsymbol{X} \quad (4.24)$$

The displacements of the truss spar are measured at the cellar deck which is to be translated to the center of gravity, **g** of the structure before making comparisons. As shown in figure Fig. 31, the body fixed coordinates at the position of the measuring sensors is $\boldsymbol{X_m} = (x_m, y_m, z_m)^t$ and the body fixed coordinates at the center of gravity is $\boldsymbol{X_g} = (x_g, y_g, z_g)^t$ and let ***S*** be the distance between the two points, given by the equation (4.25)

$$\boldsymbol{S} = \boldsymbol{X_g} - \boldsymbol{X_m} \quad (4.25)$$

From equation(4.24), we can write

$$\hat{\boldsymbol{X}}_{\boldsymbol{g}} = \boldsymbol{\xi}_g + \mathbf{T}^t \boldsymbol{X}_{\boldsymbol{g}} \quad (4.26)$$

$$\hat{\boldsymbol{X}}_{\boldsymbol{m}} = \boldsymbol{\xi}_m + \mathbf{T}^t \boldsymbol{X}_{\boldsymbol{m}} \quad (4.27)$$

where

$\boldsymbol{\xi}_g$ is the displacement at the center of gravity g, of the body expressed in $\hat{o}\hat{x}\hat{y}\hat{z}$

ξ_m is the displacement at the measuring location m, of the body expressed in $\hat{o}\hat{x}\hat{y}\hat{z}$

$$\boldsymbol{S} = \boldsymbol{\xi}_g - \boldsymbol{\xi}_m \tag{4.28}$$

Subtracting equation (4.26) from (4.27) we get

$$\hat{\boldsymbol{X}}_g = \hat{\boldsymbol{X}}_m - \boldsymbol{S} + \mathbf{T}' \boldsymbol{S} \tag{4.29}$$

$\hat{\boldsymbol{X}}_g$ is the translations motions of center of gravity with respect to the space fixed coordinates.

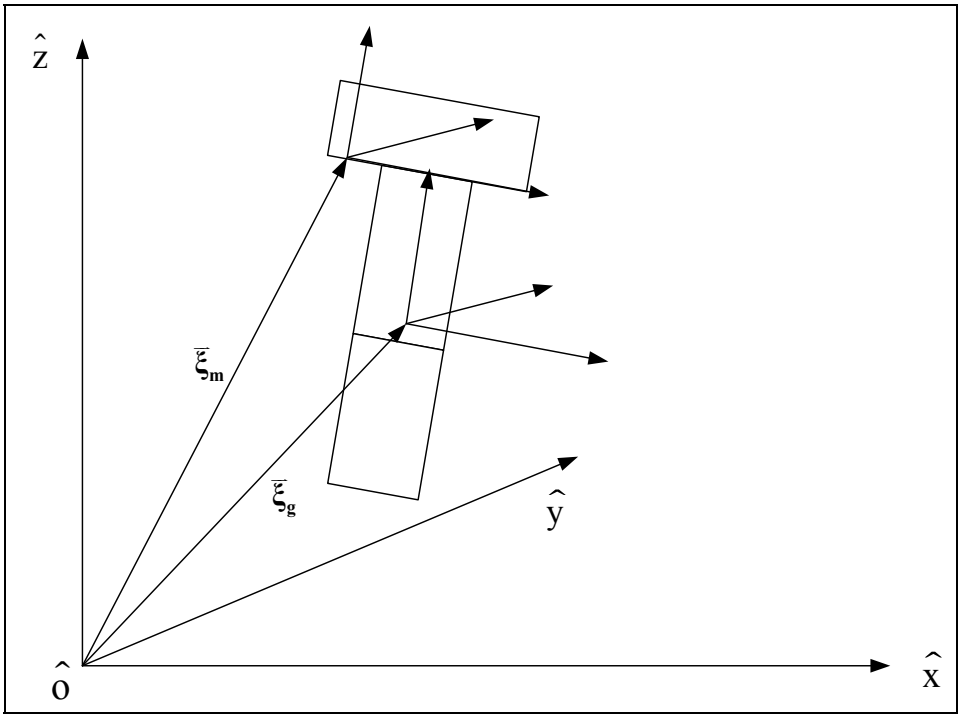

Fig. 31 Location of the body fixed coordinates at points g and m

4.3.2 Coupled Dynamic Analysis

Motion equations of the hull and dynamic equations of its mooring/riser systems

Z_m

m

Z_g

are integrated by imposing appropriate boundary conditions at their connection points (fairleads or porches). *O'X'Y'Z'* is a space-fixed coordinate system for slender structures (mooring lines, tendons, risers), with origin at the still water surface and Y' axis positive upward. *OXYZ* is a space-fixed coordinate system for the hull, with origin at the still water surface and *Z* axis positive upward. *O'* and *O* are coincident. *oxyz* is a body-fixed coordinate system moving with the body (Fig. 32).

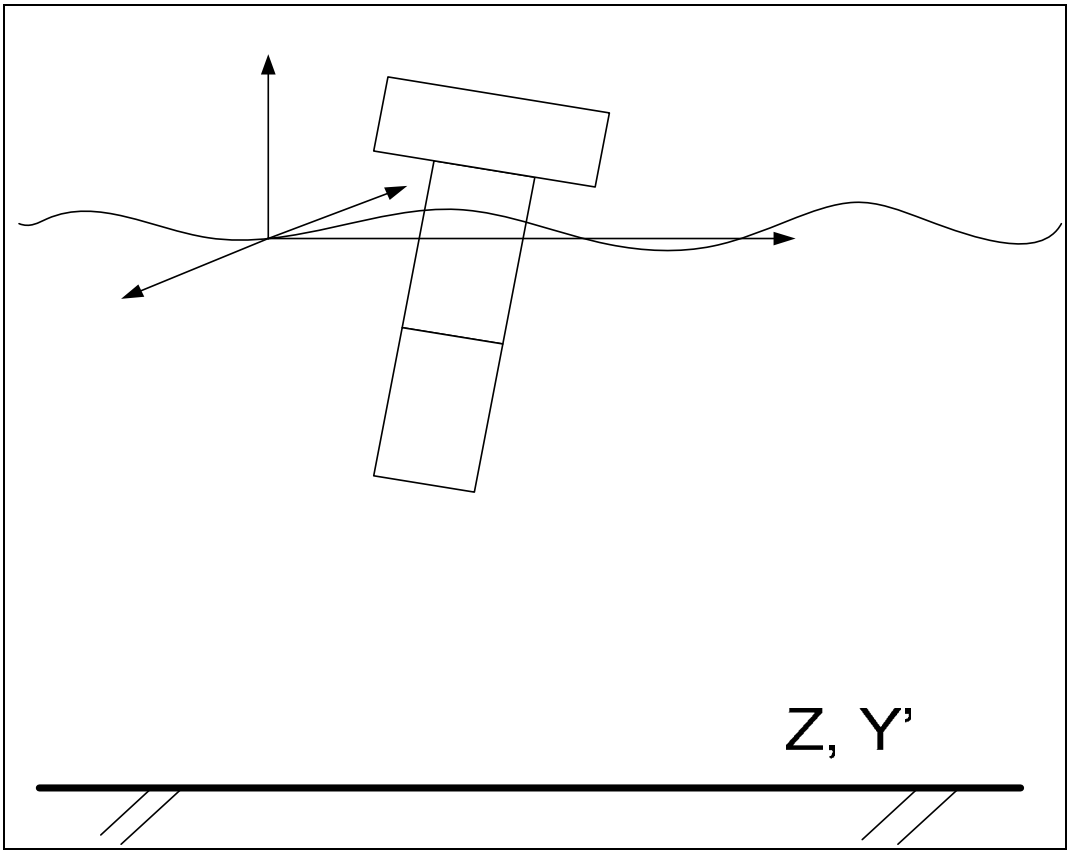

Fig. 32 Coordinate system for structure and mooring system

Y

The coordinate of the connection point on the hull as expressed in body-fixed coordinate system is $\boldsymbol{x}_{cl}$. The coordinate of the connection point of *lth* mooring line as

O,O'

Z'

expressed in $O'X'Y'Z'$ is $\boldsymbol{r}_{0l.}$ The relationship between them is:

$$\mathbf{r}_{0l} = \mathbf{L}^t(\mathbf{T}^t\mathbf{x}_{cl} + \mathbf{X}_{\hat{o}} + \boldsymbol{\xi}) \tag{4.30}$$

where **L** is the transfer matrix between $OXYZ$ and $O'X'Y'Z'$:

$$\begin{Bmatrix} \boldsymbol{X} \\ \boldsymbol{Y} \\ \boldsymbol{Z} \end{Bmatrix} = \boldsymbol{L}\begin{Bmatrix} \boldsymbol{X}' \\ \boldsymbol{Y}' \\ \boldsymbol{Z}' \end{Bmatrix} \tag{4.31}$$

$$\boldsymbol{L} = \begin{Bmatrix} 1 & 0 & 0 \\ 0 & 0 & -1 \\ 0 & 1 & 0 \end{Bmatrix} \tag{4.32}$$

Since the fairlead (or porch) is at s=0, the generalized forces and moments applied on at the fairlead or porch of lth mooring line/riser is given by

$$\mathbf{f}_1 = -\left\{\tilde{\lambda}\mathbf{r}'(0) - (B\mathbf{r}''(0))'\right\} = -\mathbf{F}(0) \tag{4.33}$$

$$\mathbf{f}_2 = -\frac{1}{L}B\mathbf{r}''(0) \tag{4.34}$$

For hinged boundary conditions, no moment is transferred. Hence, $\mathbf{f}_2$ is equal to zero and forces applied on the hull at lth fairlead are,

$$\mathbf{F}_l = \mathbf{F}(0) = -\mathbf{f}_1 = -(f_{11}, f_{12}, f_{13})_l \tag{4.35}$$

If the mooring/riser system consists of L individual mooring lines/risers, the total forces applied on the hull are the summation of forces and moments of each mooring line/riser applied on the structure at the fairlead or porch. The forces and moments of the

mooring system applied on the hull can be expressed as:

$$\mathbf{F}_M = \sum_{l=1}^{L} (\mathbf{L}\mathbf{F}_l) \tag{4.36}$$

$$\mathbf{M}_M = \sum_{l=1}^{L} \left[\mathbf{r}_{cl} \times (\mathbf{T}\mathbf{L}\mathbf{F}_l) + \mathbf{T}\mathbf{L}\tilde{\mathbf{M}}_l \right] \tag{4.37}$$

It should be noted that $\mathbf{F}_M$ is expressed in the space-fixed coordinate system $\hat{o}\hat{x}\hat{y}\hat{z}$, and $\mathbf{M}_M$ is expressed in the body-fixed coordinate system *oxyz*. When hinged boundary conditions are applied, $\tilde{\mathbf{M}}_l = 0$.

4.4 Estimating the Natural Periods and Decay Rates

Decay tests are conducted for all the six degrees of freedom(6-DOF) to estimate the decay rates and natural periods. A detailed procedure for the calculation of decay rates and natural periods is described below.

4.4.1 Estimation of Damping Ratio

The damping ratio in all six degrees of freedom (6-DOF) can be obtained by conducting free decay tests in each degree of freedom. A heave decay test is shown in Fig. 33. Each damped free vibration can be approximately expressed by equation (4.38)

$$m\ddot{X} + b_1\dot{X} + b_2\dot{X}\left|\dot{X}\right| + kX = 0 \tag{4.38}$$

where:

m = total mass (ship mass + added mass)

b_1 = linear damping coefficient in mode X

b_2 = quadratic damping coefficient in mode X

k = restoring coefficient in mode X

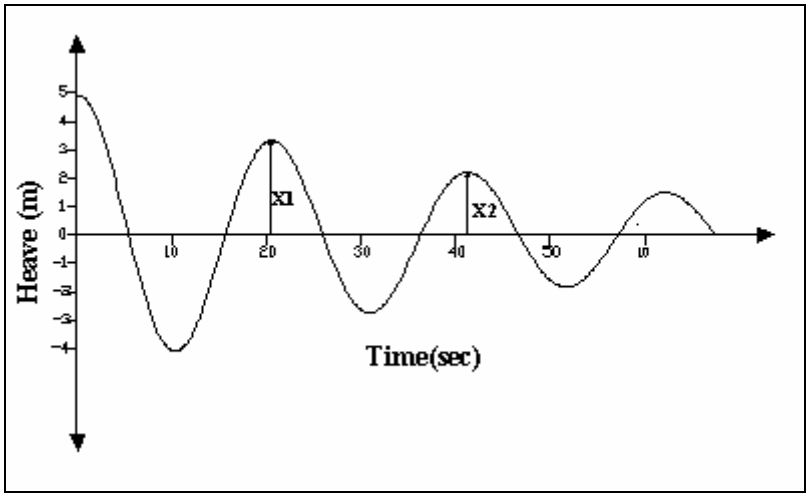

Fig. 33 Heave decay test

The linear and quadratic damping coefficients are found in the following way. When the decrease of motion amplitude divided by the mean motion amplitude is plotted versus the mean motion amplitude as shown in Fig. 34

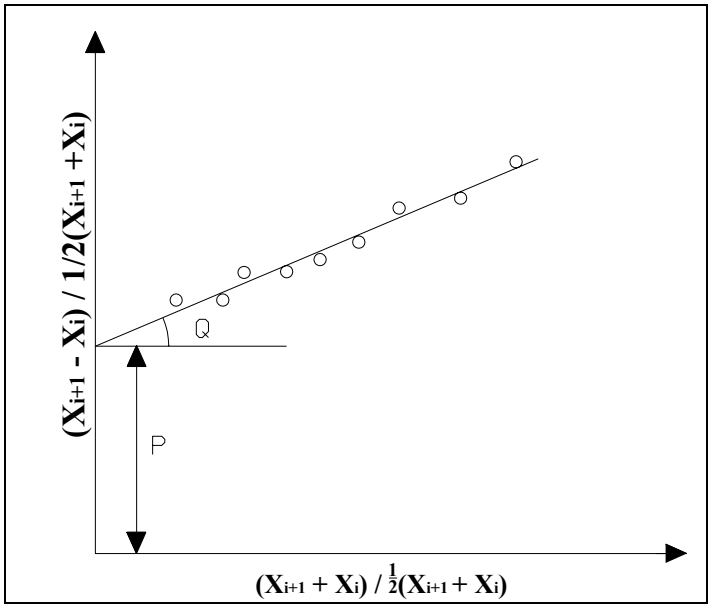

Fig. 34 Estimation of damping coefficients

Intercept of the line on Y axis, P indicates the linear damping parameter while the slope of the line, Q indicates the quadratic damping parameter. Theses damping coefficients for the global motions are provided in Table 7

Natural period, T_n is obtained by taking average of the period of seven consecutive cycles of the free vibration test are also provided in Table 7.

Table 7 Decay test results

Global Motion	**Natural Period, T_n (sec)**	**Linear Damping ,P**	**Quadratic Damping,Q**
Surge	288.92	0.0077	0.0158
Sway	290.0	0.0079	0.0164
Heave	20.8	0.0379	0.0186
Roll	40.78	0.0129	0.0076
Pitch	37.82	0.0145	0.0154
Yaw	44.87	0.0120	0.0131

4.5 Estimation of the Hydrodynamic Coefficients

A review of various studies on the related model tests is conducted to accurately predict the hydrodynamic coefficients of hard tank, truss members, heave plates, soft tank, mooring lines and risers. This includes Magee et al., (2000); Igor Prislin et al., (1998); Sarpkaya, T. and M. Isaacson, (1981) . In addition a number of iterations of decay tests by varying hydrodynamic coefficients were performed so that the natural periods of all the global motions are approximately same as those obtained from the measurement data. A set of hydrodynamic coefficients used for our numerical simulation is given in Table 8

4.6 Static Analysis

Static analysis of the coupled system is performed by applying a steady force on the spar in the surge and sway directions respectively. The offset of the system along with the restoration forces of the coupled system are computed using the numerical code COUPLE. The static stiffness curves in the surge and sway directions are illustrated in Fig. 35 and Fig. 36 respectively**.**

Analyzing the figures we can conclude that the stiffness of the mooring and riser system is high in sway direction. This is can be explained by analyzing the mooring and riser configurations given in Fig. 3 and Fig. 4**.** Mooring lines 7, 8 and 9 and the steel catenary risers are directly contributing to the stiffness in sway direction while mooring lines 1, 2, 3, 4, 5 and 6 contribute both to the sway stiffness and the surge stiffness.

Table 8 Hydrodynamic coefficients of hull members, mooring lines and risers

Structural members	**Hydrodynamic coefficients**	
	Drag Coeff. (C_D)	**Added mass coeff. (C_m)**
Hard tank	1.2	1.0
Truss members	1.0	0.8
Soft tank	1.2	1.0
Floatation tank	1.2	1.0
Heave plates (axial)	6.0	2.0
Mooring chain (axial)	2.45	2.0
Mooring wire (axial)	1.2	1.0
Risers (axial)	1.0	1.0

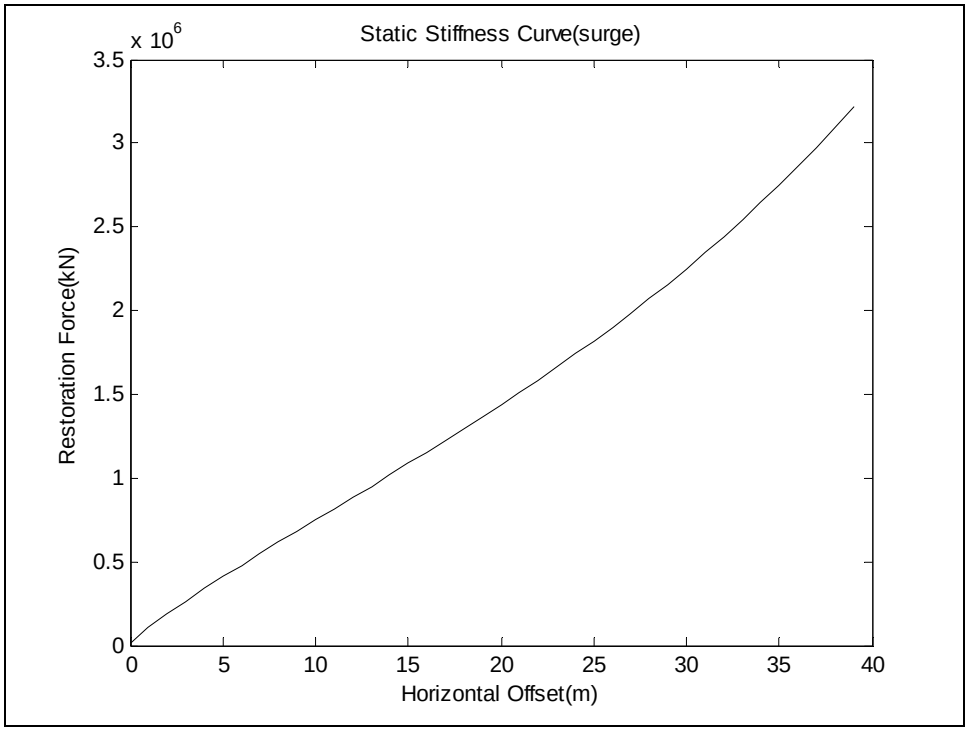

Fig. 35 Static Stiffness Curve in the Surge direction

Analyzing figures we can conclude that the stiffness of the mooring and riser system is high in sway direction. This is can be explained by analyzing the mooring and riser configurations given in Fig. 3 and Fig. 4**.** Mooring lines 7, 8 and 9 and the steel catenary risers are directly contributing to the stiffness in sway direction while mooring lines 1, 2, 3, 4, 5 and 6 contribute both to the sway stiffness and the surge stiffness.

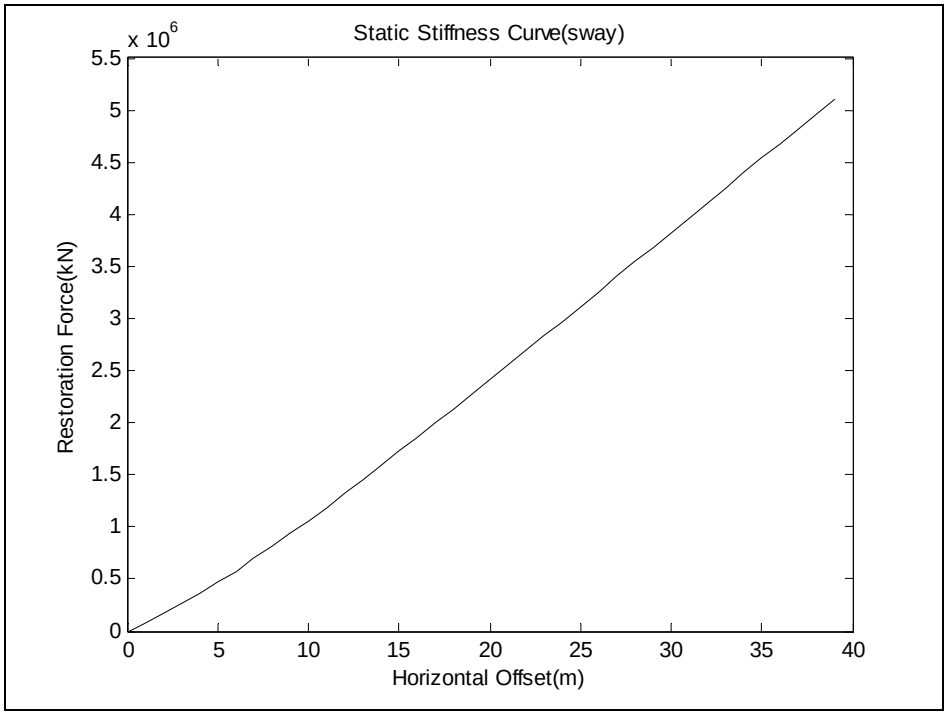

Fig. 36 Static stiffness curve in the Sway direction

In addition to the static analysis in surge and sway directions, we also compute the static stiffness using the numeric code by applying steady force at an angle of 45 degrees to the x-axis. This static stiffness curve is compared with a static stiffness curve computed by taking the vector sum of the surge and sway stiffness. This comparison results are shown in Fig. 37. We can see that the vector summation over predicts the restoration force compared to the coupled analysis. This is due to the fact that the asymmetric mooring system has a slight sway motion along with the surge motion when a force is applied in the x-direction. Similarly mooring system has a slight surge motion along with the sway motion when a force is applied in the y-direction. These slight motions leads to an increase in the surge and sway stiffness. Therefore the vector summation of surge and sway stiffness is more than that of the coupled analysis.

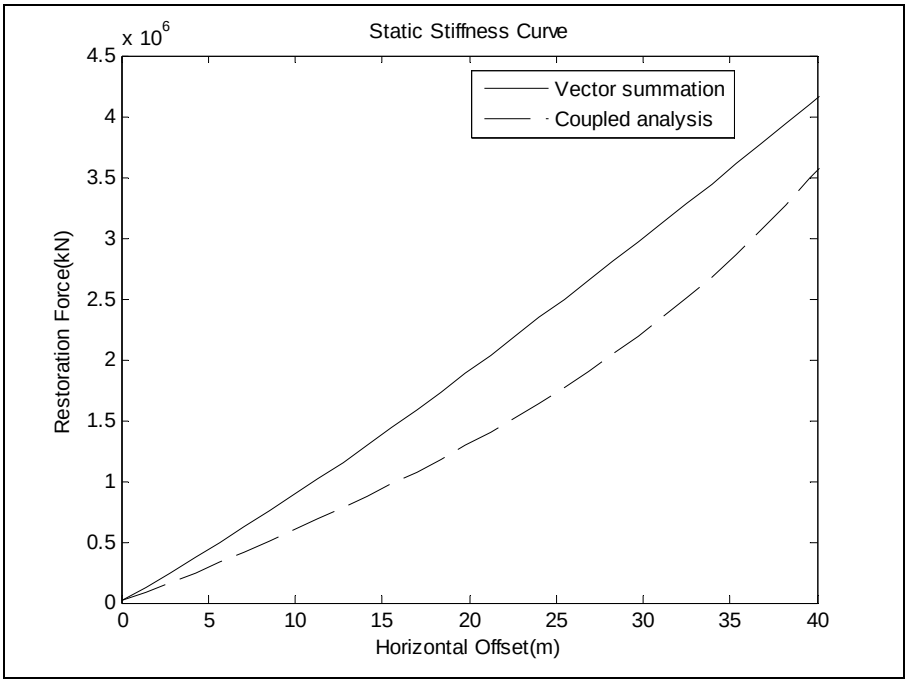

Fig. 37 Static stiffness curve (45º clockwise to +ve X axis)

5. SIMULATION RESULTS AND FIELD MEASUREMENTS

Coupled time domain simulation of the spar interacting with the mooring system, steel catenary risers and top tensioned risers was performed for a three-hour storm duration. The statistics and energy spectra of the global motions of the spar at the center of gravity and the mooring line tensions at the fairlead obtained from the numerical simulation are compared with the corresponding field measurements.

5.1 Global Motions

Various statistics of global motions such as maximum, minimum, mean, standard deviation and root mean square (RMS) of the simulation in three-hour storm duration are compared with the corresponding field measurements.

Comparisons between simulated and measured maximum values of the translation motions are shown in Fig. 38. The corresponding comparison results of rotations are shown in Fig. 39. The maximum of simulated surge is 3.9% higher than that of the corresponding field measurement. This discrepancy is mainly due to the variation in the direction of wave and wind during the storm. The maximum of sway, heave, roll and yaw match very well with that of the field measurements. But it is clear that the maximum pitch is appreciably larger than the corresponding field data. This discrepancy is due to the fact that the multi-contact coupling between the top tensioned risers and guide frames inside of the spar moon pool was not simulated in the model. The coulomb damping between the buoyancy cans and riser guide frames inside the moon pool were also not considered during simulation.

Comparisons between simulated and measured minimum values of the translation motions are shown in Fig. 40. The corresponding results of rotations are shown in Fig. 41. The trends between the comparison of minimum values of all global motions behave similar to those of the maximum values. The surge and pitch motions are over predicted while other simulated motions match well with the field measurements.

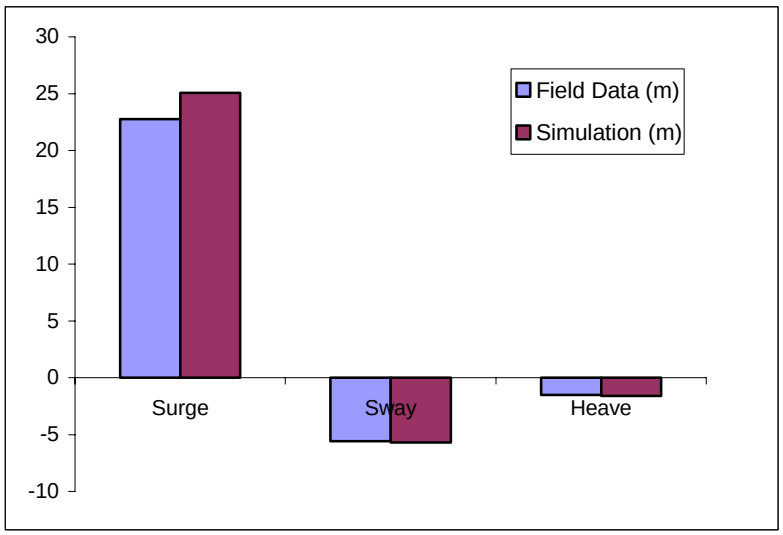

Fig. 38 Comparison of maximum values of translations

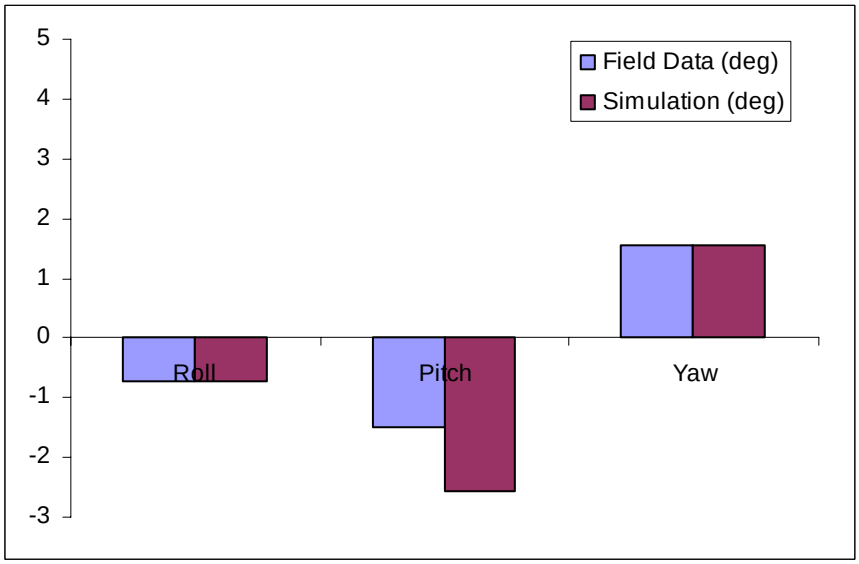

Fig. 39 Comparison of maximum values of rotation

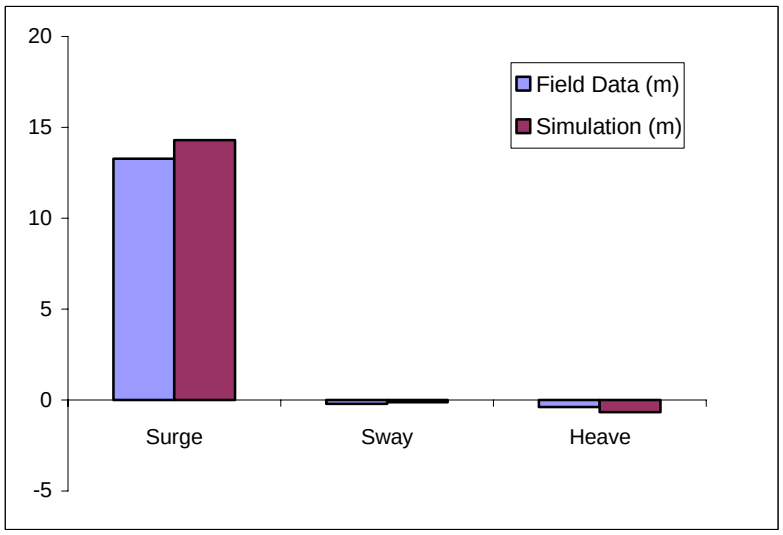

Fig. 40 Comparison of minimum values of translation motions

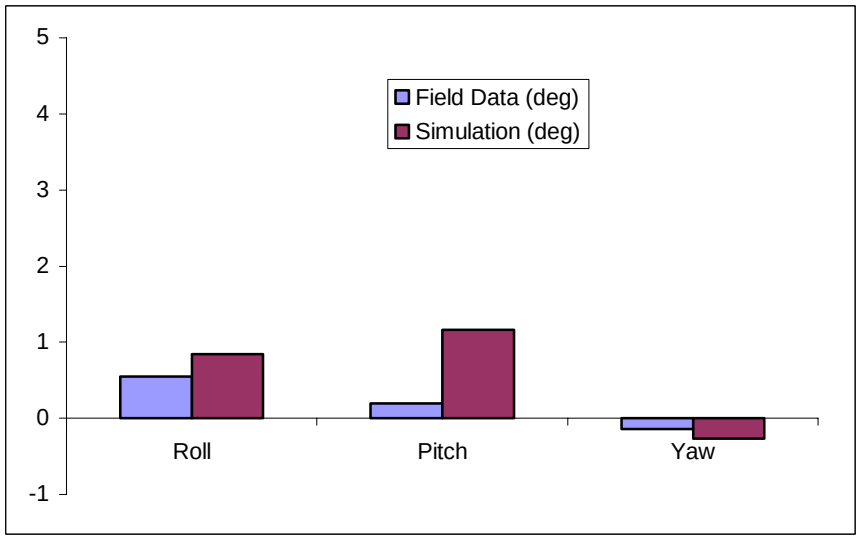

Fig. 41 Comparison of minimum values of rotations

Comparisons between the simulated and measured mean values of the translation motions are shown in Fig. 42 and the mean values of rotations in Fig. 43. The mean values of all translations and rotations match very well with field data.

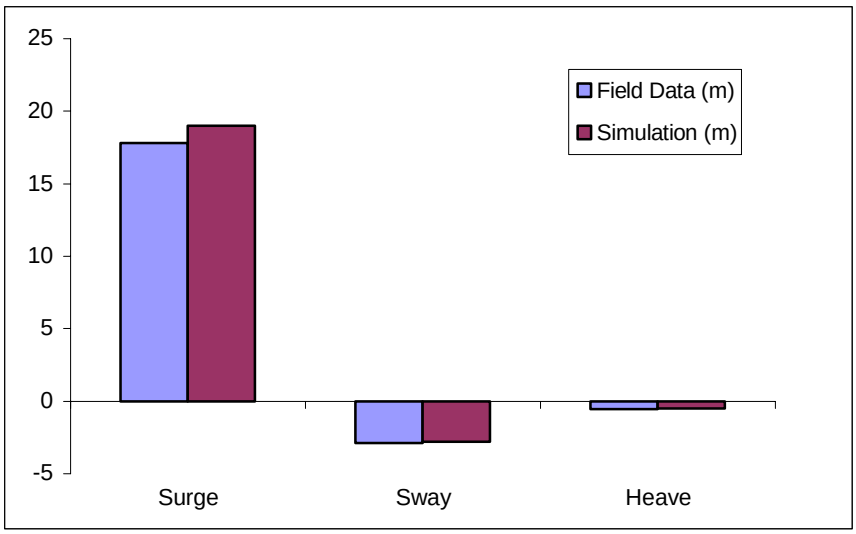

Fig. 42 Comparison of mean values of translation motions

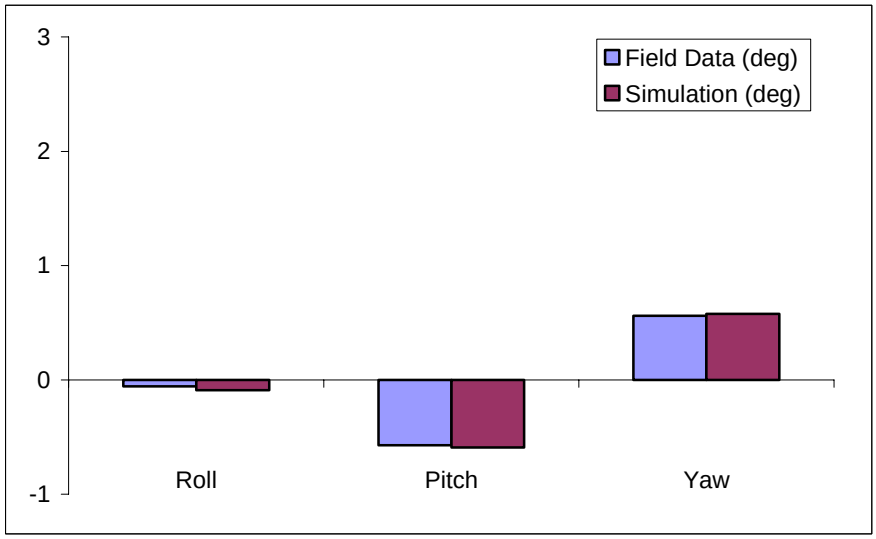

Fig. 43 Comparison of mean values of rotations

5.1.1 Root Mean Square Values (RMS)

Comparisons between the simulated and measured root mean square values of the translation are shown in Fig. 44 and the corresponding results of rotations are shown

in Fig. 45. The root mean square values of both translations and rotations show a good between the simulations and the field measurements. From the figures it is clear that the trends of the RMS values follow those of the mean values, which is expected because the magnitude of all motions are dominated by their corresponding mean values.

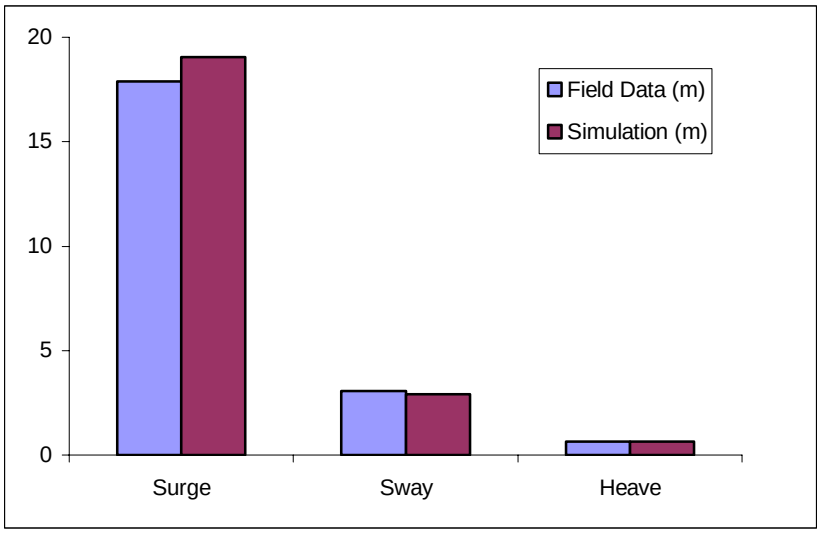

Fig. 44 Comparison of RMS values of translation motions

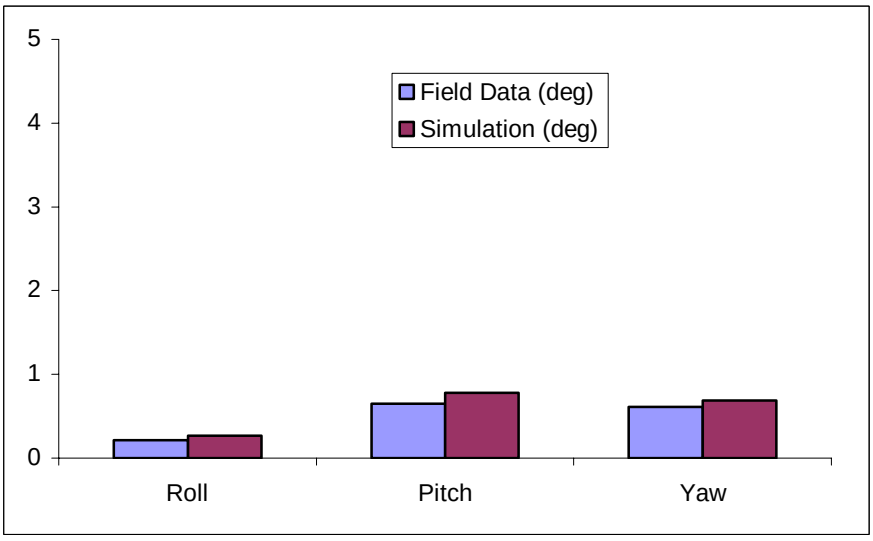

Fig. 45 Comparison of RMS values of rotations

5.1.2 Standard Deviation of Low and High Frequency Motions

For the purpose of comparison we chose the separation point between high frequency motions and low frequency motions at 0.04Hz. The high frequency range covers the range of the wave frequency duw to the local wind generated waves and the long period storm waves while the low frequency range covers the low-frequency slow drift motions of the spar. The standard deviations low frequency motions (LFSTD) are shown in Fig. 46 and Fig. 47. From these figures it is clear that the low frequency components of all translation motions are slightly under predicted with a maximum relative difference of 15%, while the LFSTD value of pitch is over predicted with a deviation of 44% from the field measurements. These discrepancies are due to the non-stationarity of the current and wave direction. Lack of buoyancy can model in the simulations also lead to the discrepancies in rotations. The standard deviations high-frequency motions (HFSTD) are shown in Fig. 48 and Fig. 49. The predicted wave frequency motions are appreciably larger than the field measurements for pitch and yaw motions. These discrepancies exist due to the fact that the effect of directional wave spreading is not considered in the simulations.

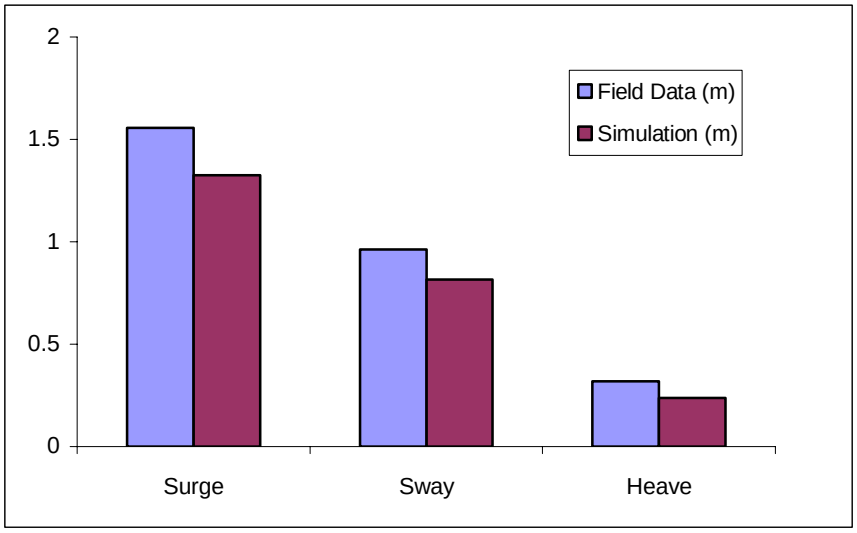

Fig. 46 Comparison of LFSTD values of translations

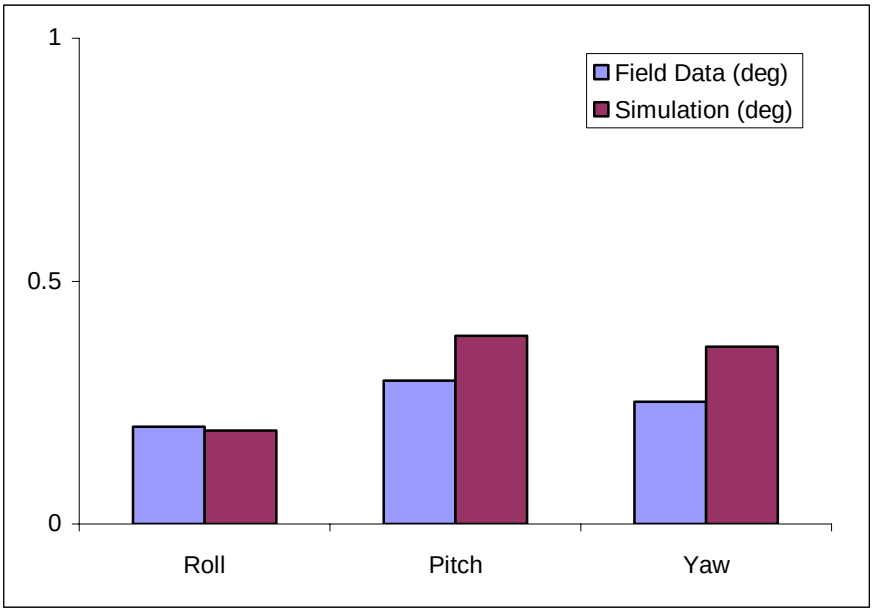

Fig. 47 Comparison of LFSTD values of rotations

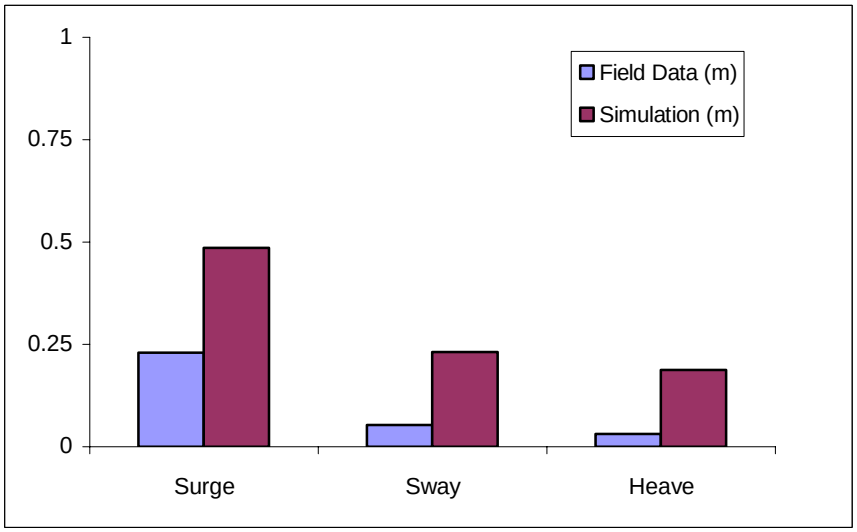

Fig. 48 Comparison of HFSTD values of translations

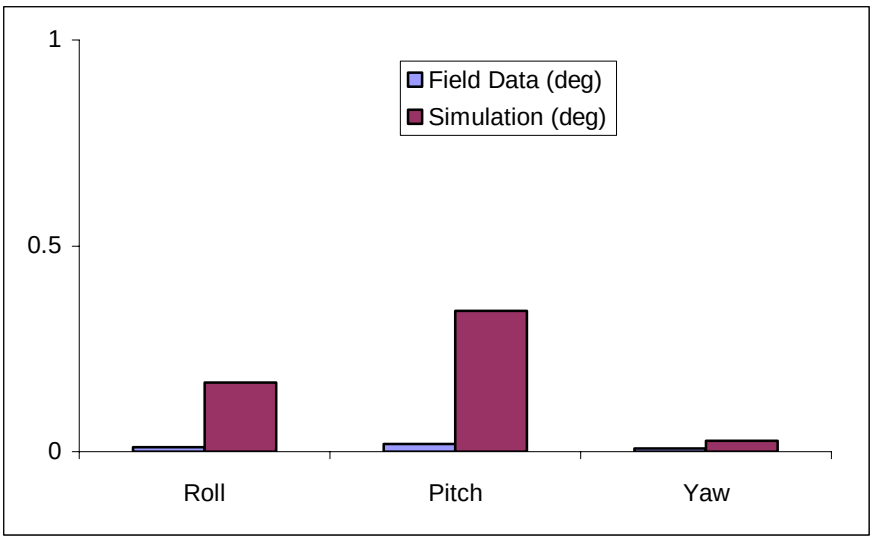

Fig. 49 Comparison of HFSTD values of rotations

5.2 Comparison of the Spectra of Global Motions

Energy spectra of global motions of simulation results are compared with that of the field measurements in Fig. 50 through Fig. 55. Energy spectra of all global motions clearly show the energy in low-frequency slow-drift motions as well as the high frequency wave motions. We can see from the figures that slow-drift motions and wave frequency motions of surge and sway matches very well with those of the field measurements.

The peak at the resonant frequency of heave motion is appreciably high in comparison with the field measurements. Motions at natural frequency as well as the wave frequency of roll are slightly over predicted. The peak at resonant frequency is over predicted by the simulations for both yaw motions and the pitch motions.

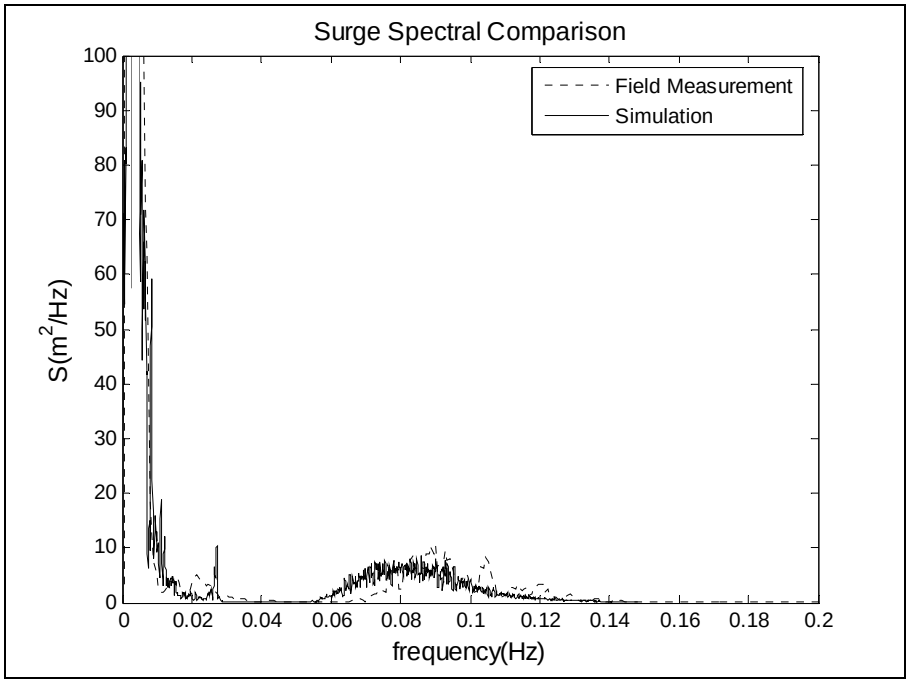

Fig. 50 Comparison of surge energy spectra

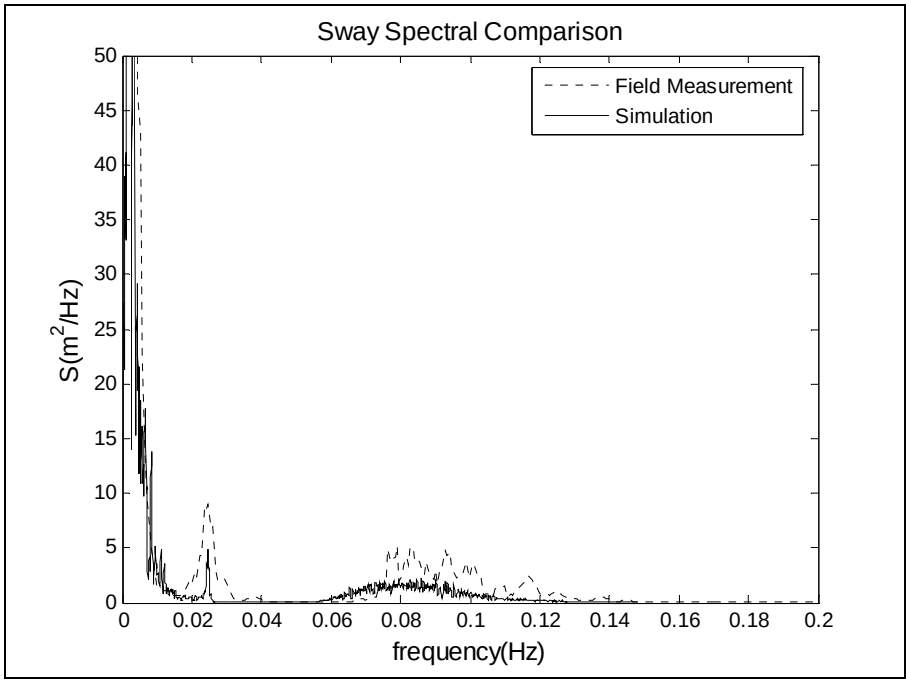

Fig. 51 Comparison of energy spectra of sway motions

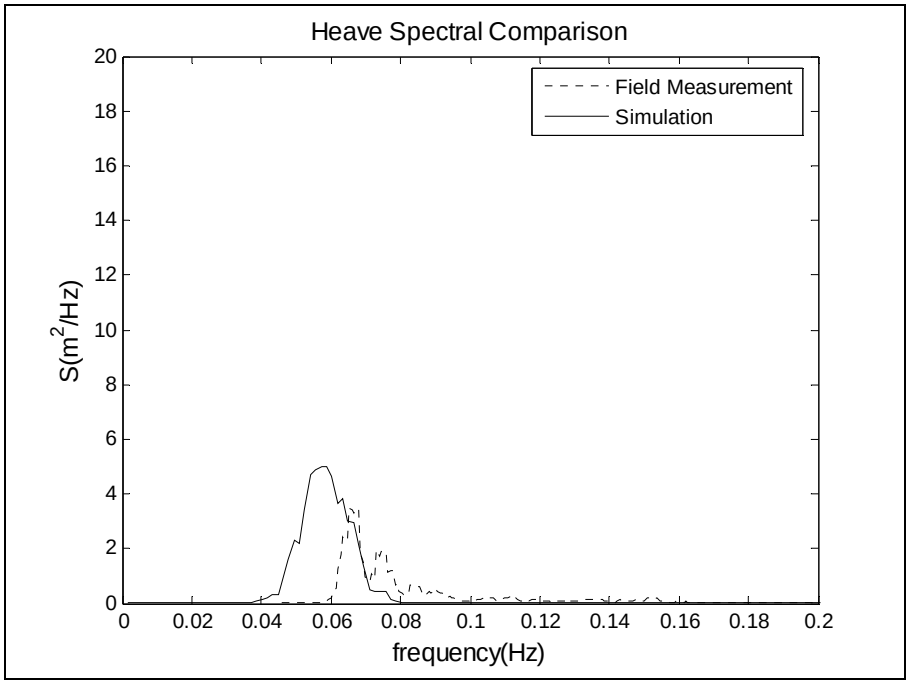

Fig. 52 Comparison of energy spectra of heave motions

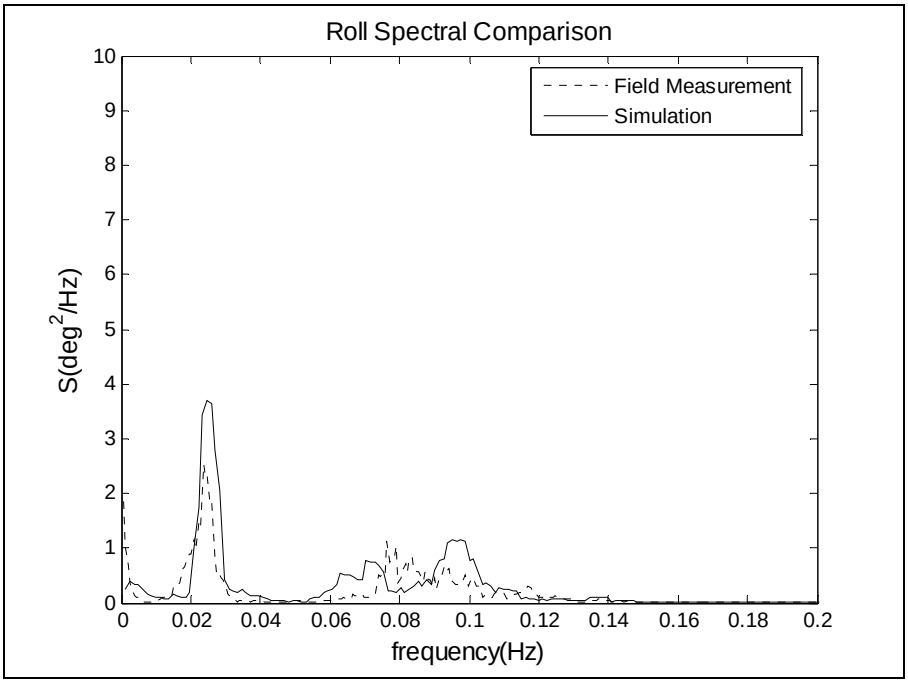

Fig. 53 Comparison of energy spectra of roll motions

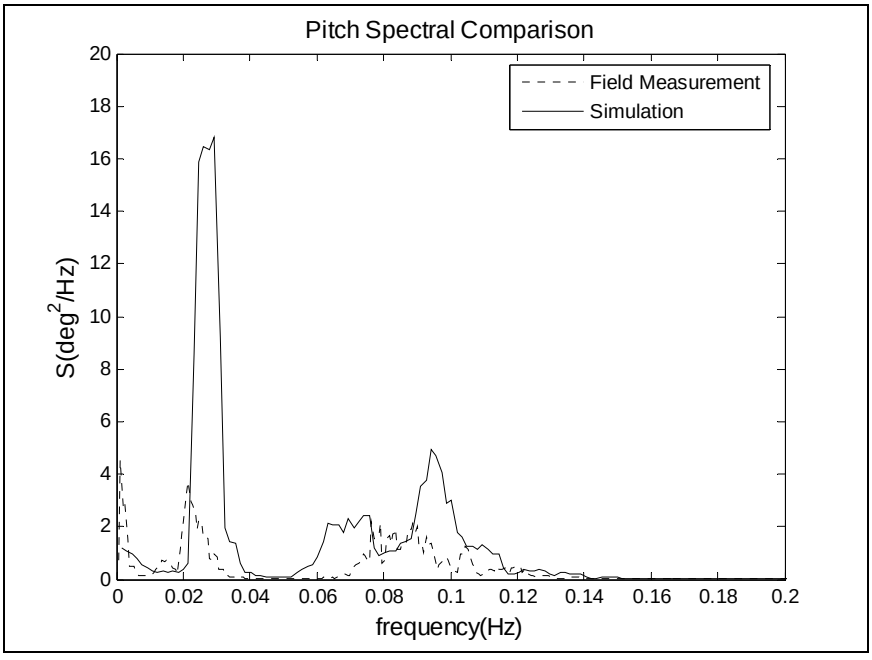

Fig. 54 Comparison of energy spectra of pitch motions

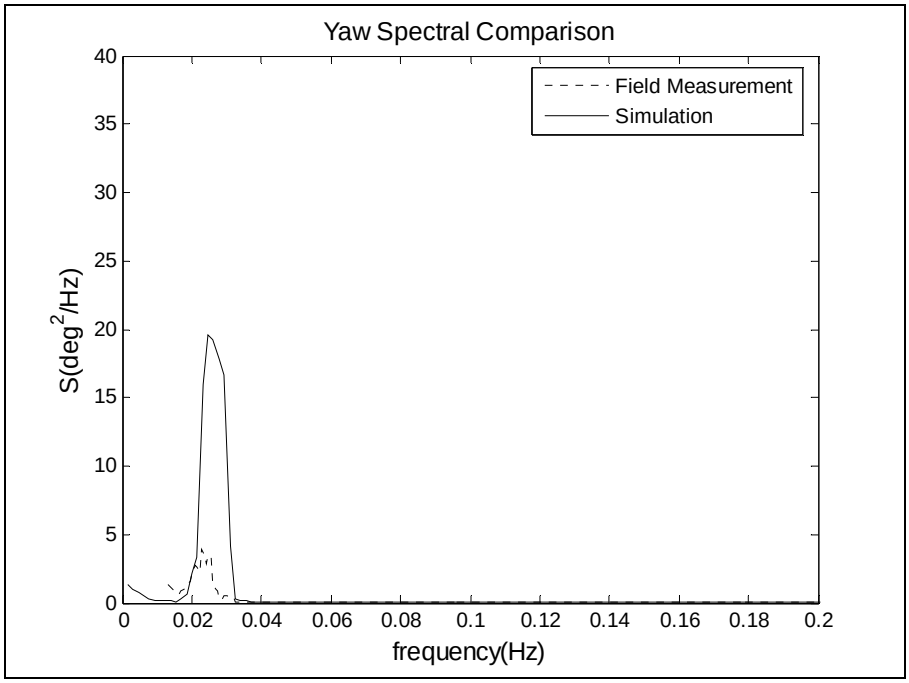

Fig. 55 Comparison of energy spectra of yaw motions

5.3 Mooring Line Tensions

The mooring line tensions at the fairlead are analyzed. The sensing devices to measure the mooring line tensions are located at the chain jack which is about 66.75 meters above the fairlead. In order to make a fair comparison in the numerical results, we have to add the weight of the mooring chain between the chain jack and the fairlead to the fairlead tensions. Apart from this the Coulomb friction at the fairlead has to be computed and added to the simulated tensions.

5.3.1 Estimation of Coulomb Friction at the Fairlead

A sketch of a typical fairlead is shown in Fig. 56. When the chain moves along the roller, Coulombs dynamic friction acts on the bearing. The equilibrium of the moments and the horizontal forces were derived by Tahar et al. (2005),

$$\sum M_o = 0 \Rightarrow -\mu N r + T_{outboard} R - T_{inboard} R = 0 \tag{5.1}$$

$$\sum F_x = 0 \Rightarrow T_{outboard} \sin\gamma - N\cos(\gamma/2) - \mu N \sin(\gamma/2) = 0 \tag{5.2}$$

where

μ	=	Dynamic friction coefficient
R	=	Guide roller radius
r	=	Bearing radius
N	=	Normal force at bearing contact
γ	=	Departure angle of mooring line from vertical
$T_{inboard}$	=	Mooring tension inboard fairlead
$T_{outboard}$	=	Mooring line tension outboard fairlead
Mo	=	Moment with respect to origin
Fx	=	Force in x- direction,

Solving (5.1) and (5.2), we get

$$T_{inboard} = T_{outboard}\left[1 - \frac{\mu r}{R}\frac{\sin(\gamma)}{\cos(\frac{\gamma}{2}) + \mu \sin\left(\frac{\gamma}{2}\right)}\right] \tag{5.3}$$

$T_{outnoard}$ is tension at the fairlead . Using equation(5.3), we can compute $T_{inboard}$

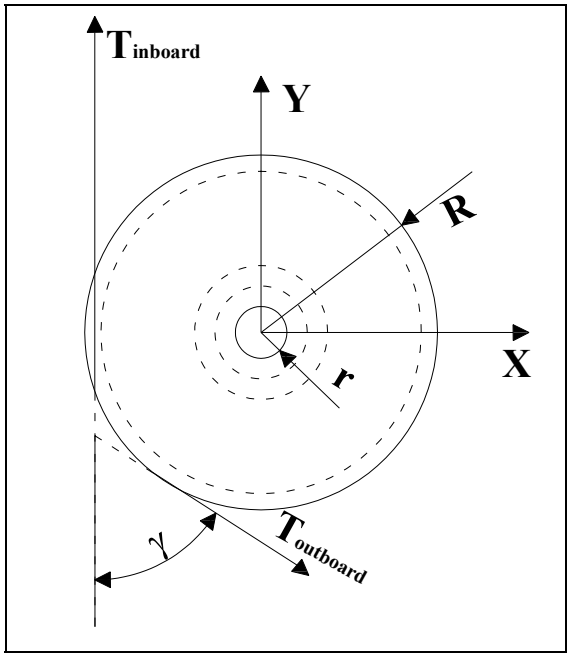

Fig. 56 Free body diagram of a typical fairlead

5.4 Comparison of Mooring Line Tensions

Various statistics of measured mooring line tensions at the chain jack are compared with the corresponding simulation results.

The comparison of maxima of simulated mooring line tensions with those of the field measurements is shown in Fig. 57. We can see from the figure that the maximum values compare very well with that of the field measurements for least loaded mooring lines, while the simulation over predicts the maximum tensions for heavily loaded mooring lines

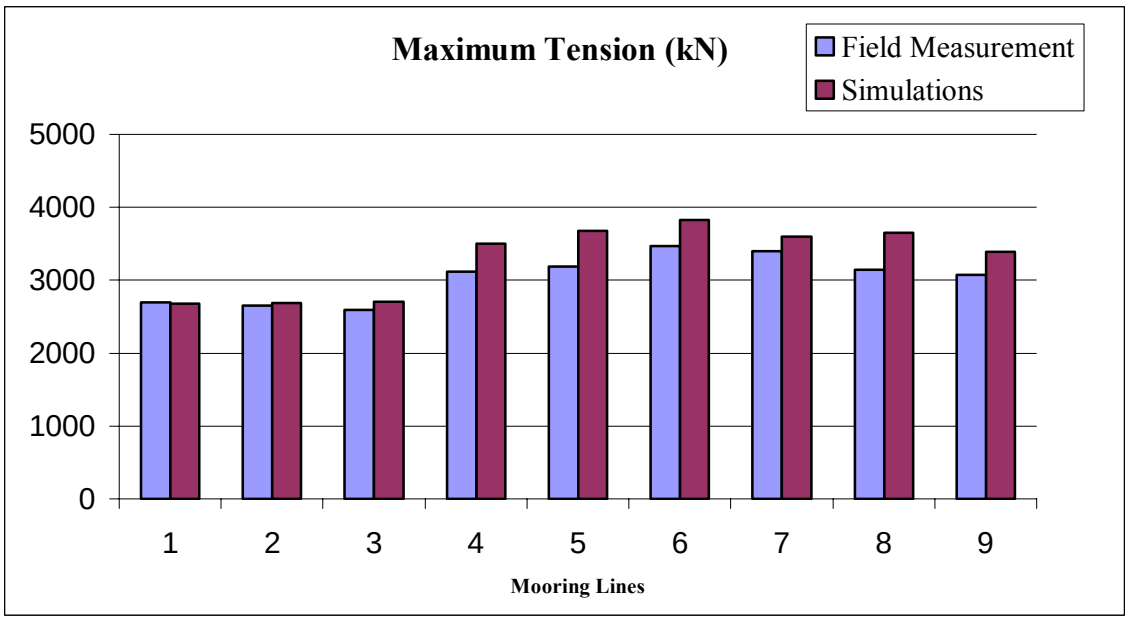

Fig. 57 Comparison of maximum tensions of mooring lines at chain jack

The comparison of mean values of simulated mooring line tension with that of the field measurements is shown in Fig. 58. We can see from the figure that the mean values match very well with those of the field measurements for all mooring lines.

The comparison of minimum values of simulated mooring line tension with those of the field measurements is illustrated in Fig. 59. We can see from the figure that the minimum values also compare very well with that of the field measurements for all mooring lines.

The comparison of Root Mean Square (RMS) values of simulated mooring line tension with that of the field measurements is shown in Fig. 60. We can see from the figure that similar to the mean and the maxima, the RMS values also compare very well with those of the field measurements for all mooring lines. Since the mean tensions are significantly higher than the corresponding dynamic tensions, the trends of RMS of the tensions mainly follow those of the corresponding mean tensions.

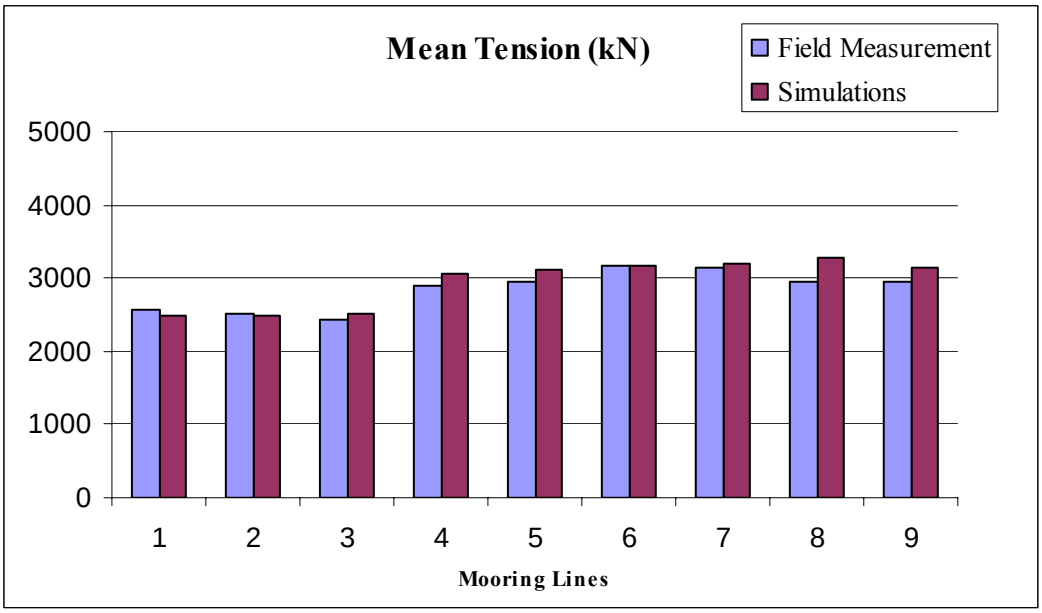

Fig. 58 Comparison of mean of mooring tensions at chain jack

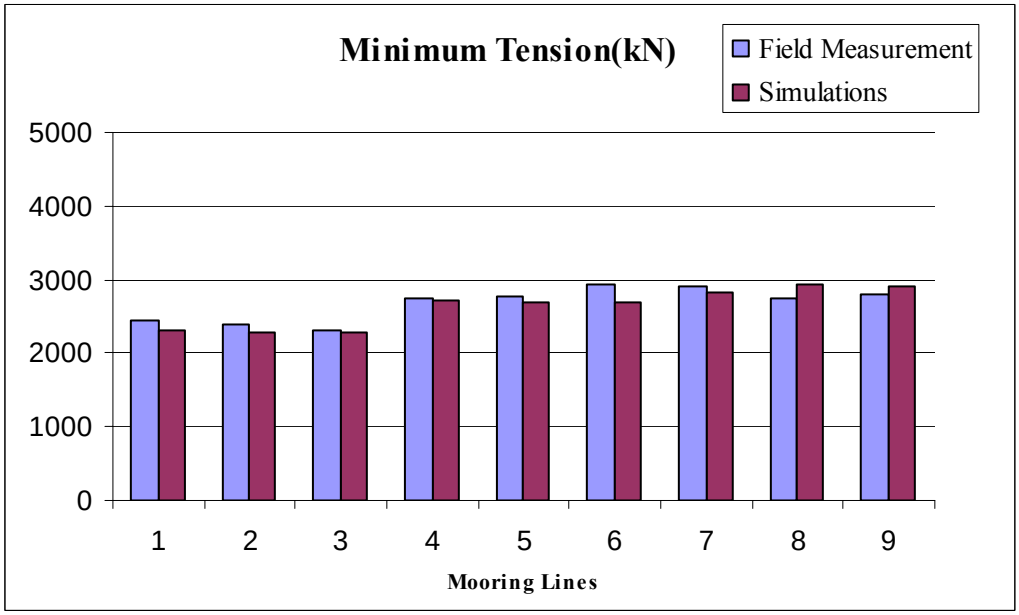

Fig. 59 Comparison of minimum value of mooring tensions at chain jack

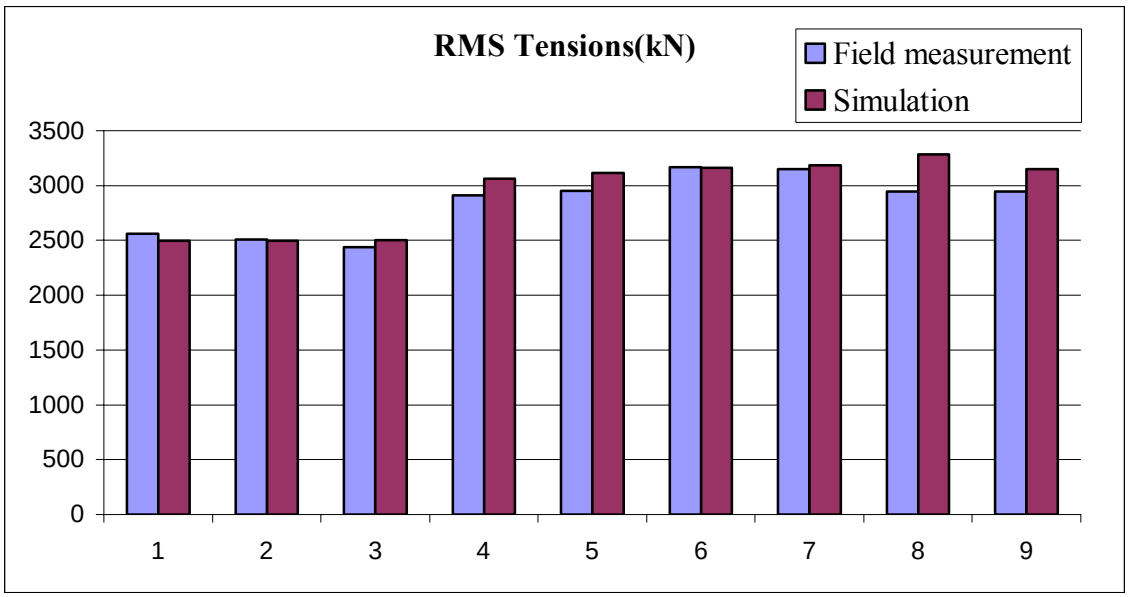

Fig. 60 Comparison of RMS values of mooring tensions at chain jack

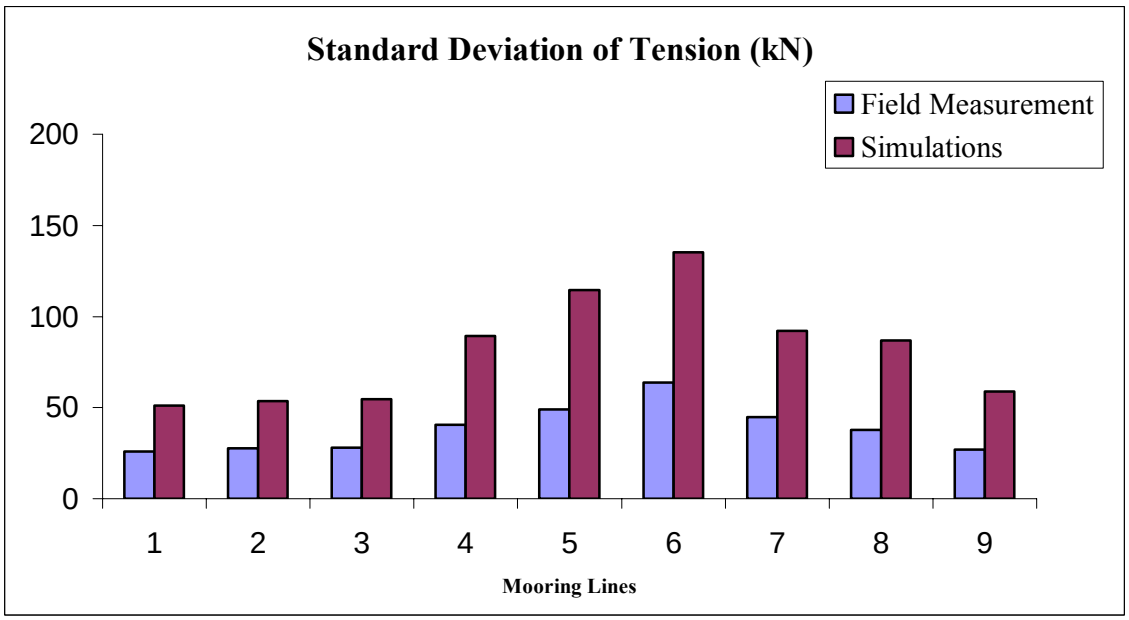

Fig. 61 Comparison of standard deviations of tensions of mooring lines at chain jack

The comparison of standard deviations of simulated mooring line tension with those of the field measurements is shown in Fig. 61. The standard deviations of simulated mooring line tensions are significantly over predicted in comparison with the field measurements. This might be due to various reasons described below:

- Discrepancies in global motions

  The comparison of simulated and measured global motions showed that there are appreciable discrepancies in pitch and yaw motions due to the lack of modeling friction between buoyancy cans and riser guide frames in the simulations. These discrepancies might be a reason for the deviations in mooring line tensions.

- Uncertainties in the fairlead friction coefficients

  From equation (5.3) it is clear that higher friction coefficients reduce the dynamic tensions to a larger extent and reduce the differences in the standard deviation.

- Uncertainties in the measurement of dynamic tension

  The inability of the measuring devices to accurately measure the high frequency mooring tensions might be another reason in this variation of standard deviations.

- Uncertainties in the simulation of metocean loads

  We have assumed that the wind, wave and current come from a fixed direction. But in reality the wind direction itself changed 25 degrees during the three hour duration of storm. It is difficult to simulate the variations of direction of wind and waves in the numerical code.

5.5 Interaction of Risers with the Hull Structure

As field development reaches deeper and deeper, the length of risers has increased enormously leading to a large riser mass relative to the hull mass. As a result inertia and damping effect on risers influence the global performance of the hull

structure. A comparative study was conducted to determine the variations in global motions and mooring line tensions of the Horn Mountain among three cases.

1. Coupled analysis of truss spar interacting with mooring lines

   The forces and moments due to the top tensions of the steel catenary risers are applied to the spar as steady forces and moments.
2. Coupled analysis of truss spar interacting with the mooring lines along with the steel catenary risers
3. Coupled analysis of truss spar interacting with the mooring lines along with the steel catenary risers and top tension risers

5.5.1 Global Motions

The comparative study of various statistics of the global motions is illustrated in Fig. 62 through Fig. 69 for all the above mentioned cases. We can observe from the figures that case 2 and case 3 simulations provide similar results while case 1 yields different results.

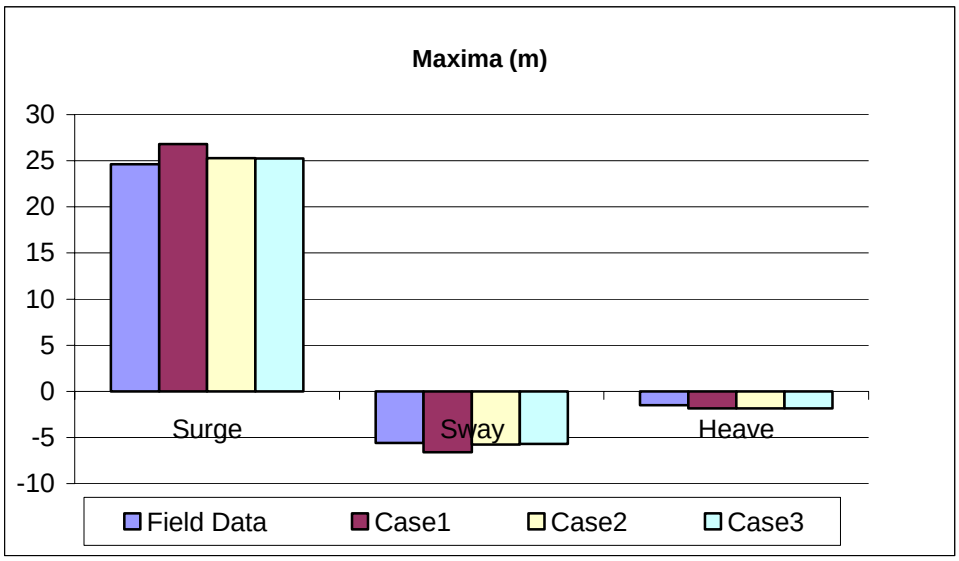

Fig. 62 Maximum values of translations of various coupled analysis cases

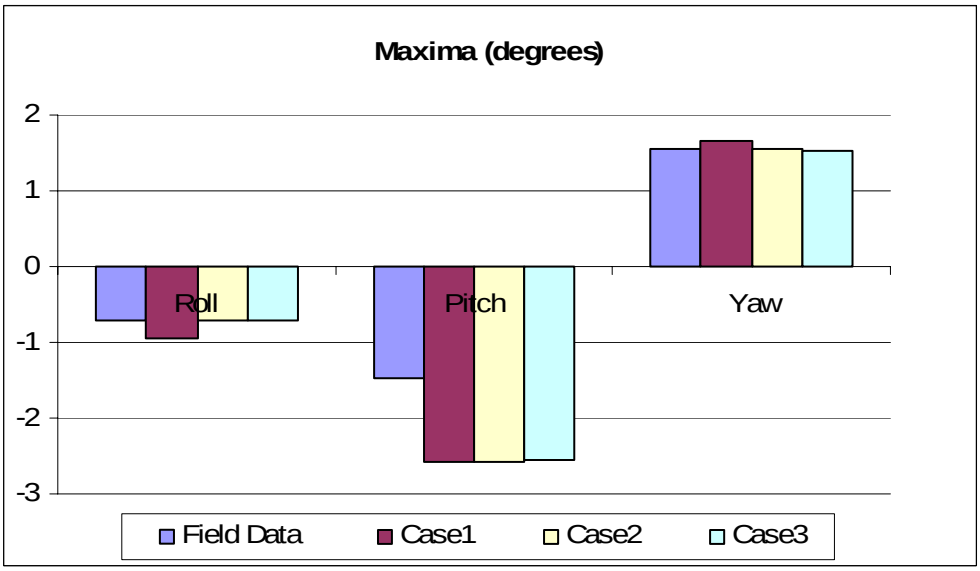

Fig. 63 Maximum values of rotations of various coupled analysis cases

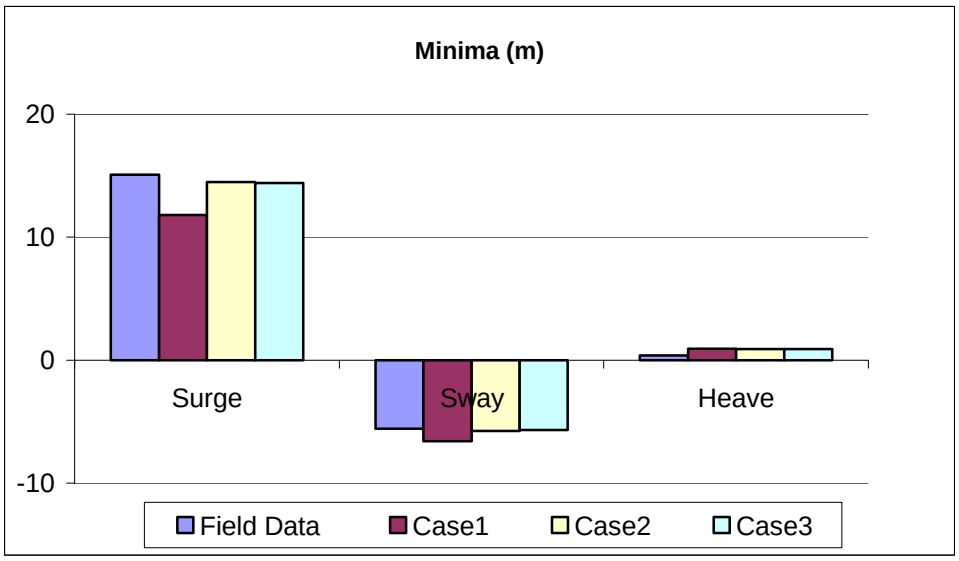

Fig. 64 Minimum values of translations of various coupled analysis cases

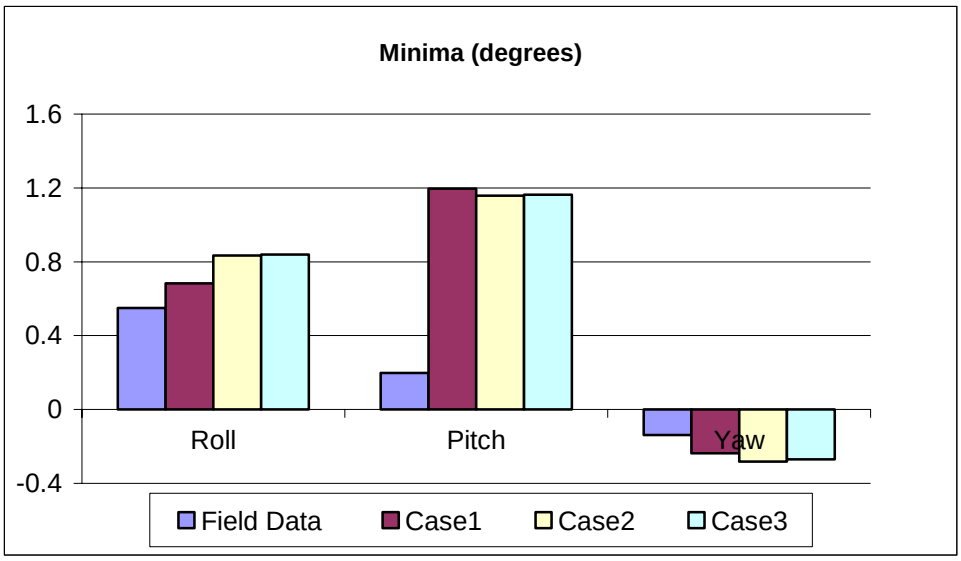

Fig. 65 Minimum values of rotations of various coupled analysis cases

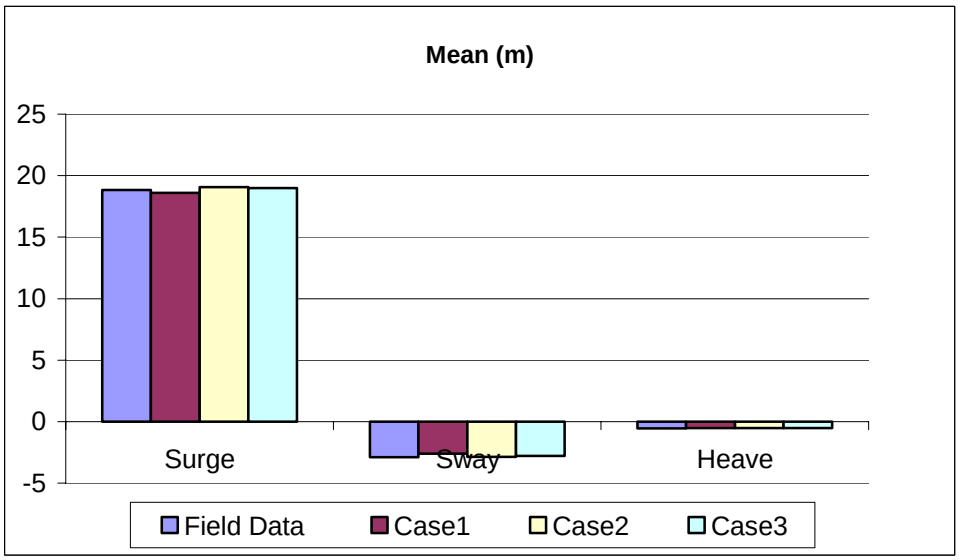

Fig. 66 Mean values of translations of various coupled analysis cases

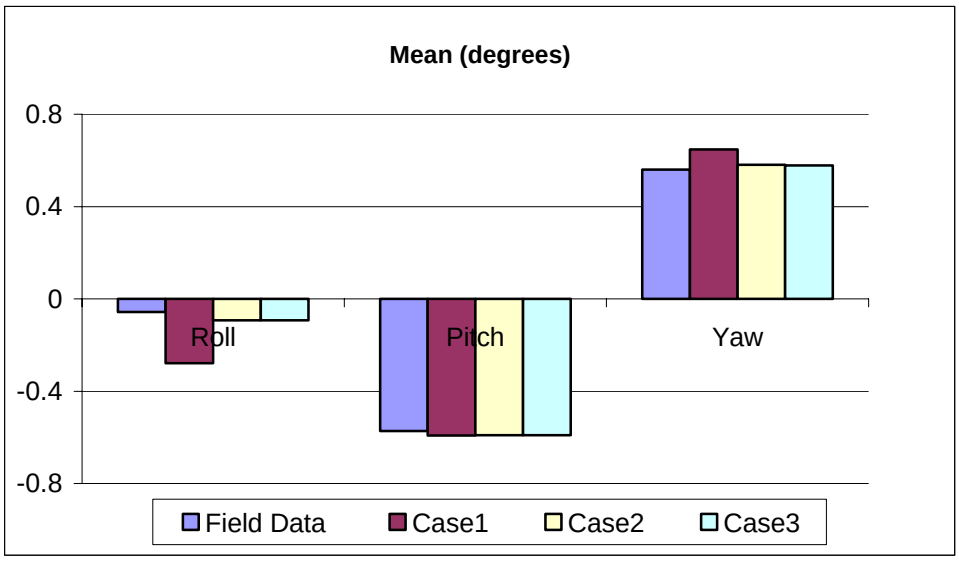

Fig. 67 Mean values of rotations of various coupled analysis cases

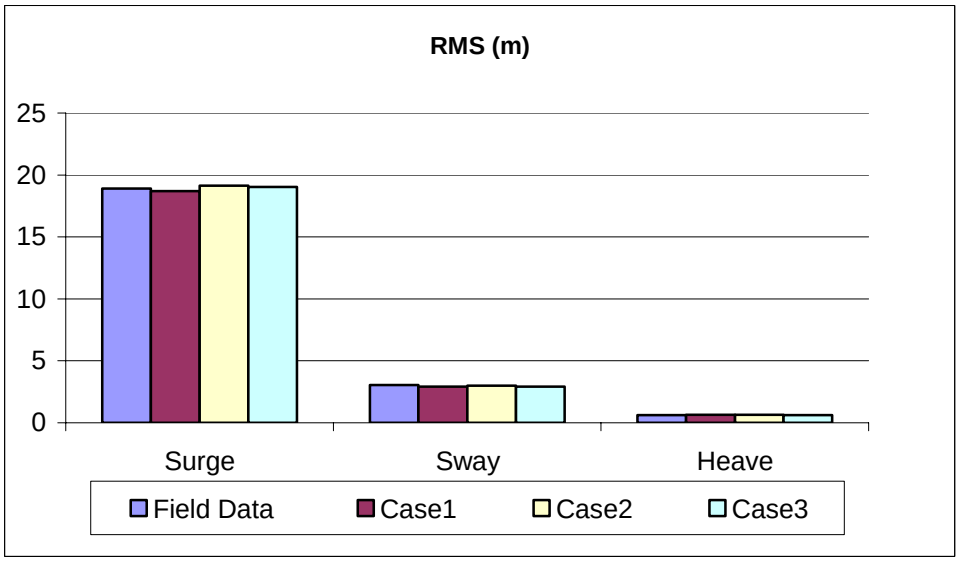

Fig. 68 RMS values of translations of various coupled analysis cases

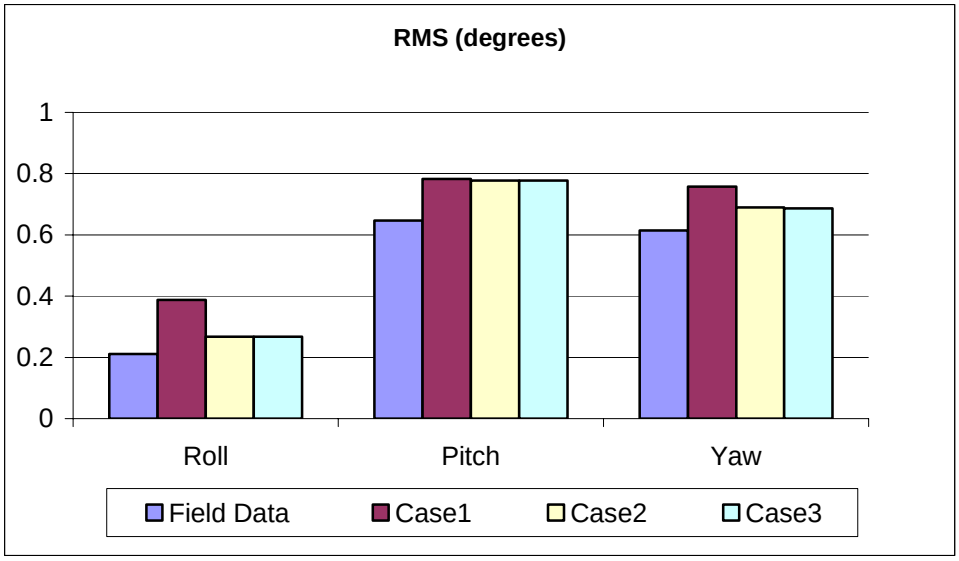

Fig. 69 RMS values of rotations of various coupled analysis cases

5.5.2 Mooring Line Tensions

The comparative study of various statistics of the mooring line tensions at the chain jack are provided in Table 9, for all the three cases. We can see that the mooring line tensions for all the three cases are approximately same.

Table 9 Statistical parameters of mooring line tensions of various coupled cases

Parameters	Case1	Case2	Case3	Field measurement
Mooring Line 1				
Maximum (kN):	2705.1233	2701.1533	2680.7833	2700.0708
Minimum (kN):	2306.0633	2296.3933	2297.9733	2442.0739
Mean (kN):	2495.8147	2492.5447	2493.2281	2562.2872
Std (kN):	51.5665	51.2881	51.0996	25.9522
RMS (kN):	2496.3474	2493.0723	2493.7517	2562.4186
Mooring Line 2				
Maximum (kN):	2714.6933	2710.1433	2691.8733	2655.5885
Minimum (kN):	2296.3533	2285.9233	2288.0433	2384.247

Table 9 Continued.

Parameters	Case1	Case2	Case3	Field measurement
Mean (kN):	2496.6259	2493.121	2493.8636	2508.6285
Std (kN):	54.0027	53.6445	53.4455	27.5643
RMS (kN):	2497.2099	2493.6981	2494.4362	2508.7799
Mooring Line 3				
Maximum (kN):	2726.6433	2721.5233	2704.8133	2588.8652
Minimum (kN):	2299.9333	2288.9533	2291.4033	2299.7308
Mean (kN):	2505.8211	2502.1353	2502.9151	2436.8422
Std (kN):	55.2195	54.7638	54.57	27.8467
RMS (kN):	2506.4295	2502.7345	2503.5099	2437.0013
Mooring Line 4				
Maximum (kN):	3492.1733	3505.9933	3501.9933	3118.2036
Minimum (kN):	2728.8733	2728.8733	2729.8233	2731.2083
Mean (kN):	3059.2318	3062.7482	3062.039	2909.5706
Std (kN):	89.5348	89.1987	89.3607	40.7113
RMS (kN):	3060.5417	3064.0468	3063.3426	2909.8554
Mooring Line 5				
Maximum (kN):	3674.7233	3686.1033	3681.4633	3184.927
Minimum (kN):	2701.0533	2698.4233	2699.4033	2766.7941
Mean (kN):	3110.3943	3115.9201	3114.7951	2950.9399
Std (kN):	114.7984	114.5502	114.3742	48.9543
RMS (kN):	3112.512	3118.0176	3116.8942	2951.3459
Mooring Line 6				
Maximum (kN):	3828.4533	3835.8433	3829.4833	3469.6132
Minimum (kN):	2681.4933	2675.8633	2676.6833	2931.3783
Mean (kN):	3150.2824	3157.7232	3156.1618	3169.6217
Std (kN):	135.8222	135.2357	135.1348	63.7274
RMS (kN):	3153.2089	3160.6177	3159.0533	3170.2623
Mooring Line 7				
Maximum (kN):	3609.5033	3601.4833	3596.2733	3393.9934
Minimum (kN):	2842.4533	2834.5033	2835.1133	2918.0336

Table 9 Continued.

Parameters	Case1	Case2	Case3	Field measurement
Mean (kN):	3179.0087	3185.5293	3183.6998	3150.7918
Std (kN):	93.5964	92.0255	91.9922	44.878
RMS (kN):	3180.3862	3186.8583	3185.0286	3151.1114
Mooring Line 8				
Maximum (kN):	3666.9933	3659.0333	3654.1733	3144.893
Minimum (kN):	2946.4033	2940.9833	2940.9633	2757.8976
Mean (kN):	3277.0202	3283.9074	3281.97	2947.2618
Std (kN):	88.7572	86.9843	86.8903	37.8588
RMS (kN):	3278.2219	3285.0539	3283.12	2947.505
Mooring Line 9				
Maximum (kN):	3393.3433	3389.3133	3386.3133	3069.2732
Minimum (kN):	2913.0933	2906.6333	2906.1833	2811.2763
Mean (kN):	3145.9464	3150.6058	3149.2768	2944.6683
Std (kN):	59.949	58.5421	58.7696	26.8608
RMS (kN):	3146.5175	3151.1496	3149.8251	2944.7908

5.6 Dynamics of Steel Catenary Riser at the Touch Down Area

For steel catenary risers, the stresses occurring in the touchdown area are of prime importance for determination of key design parameters such as the required wall thickness, the material properties and the weld quality. Furthermore, the stresses in this area are in turn very sensitive to the behavior of the soil that is in contact with the riser pipe. Dynamics at the touch down area is dominated by the dynamics of suspended length of the riser. The proportion of riser pipe resting on the seabed, compared to the length that is suspended, varies with the motion of the floater at the surface (Giertsen et al., 2004). The Equilibrium position of SCR1 is illustrated in Fig. 70. The suspended length of the SCR1 varying as a function of time in the time domain and frequency domain is shown in Fig. 71 and Fig. 72 respectively. Amplitude spectrum shows that the

dynamics of suspended length mainly depends upon high frequency loads. It is not much affected by the slow-drift motions of the floating platform. To understand better, the motions of suspended length of SCRs, the floating system was subjected to linear translation motions. Analysis of the effects of theses translation motions are provided in Table 10. From the figure and the table, it is very clear that the dynamics of riser is influenced mainly by the heave motion of the spar. Therefore the fatigue loading on riser is mainly influenced by the heave motion.

Velocities and accelerations in three directions at the touch down area of the steel catenary riser is shown in Fig. 73 through Fig. 78. Vertical velocities and accelerations are high compared to the horizontal velocities and accelerations. This confirms that vertical motions are predominant at the touch down area of the riser than the horizontal motions. Therefore fatigue loading of the riser will be influenced mainly by the vertical motions.

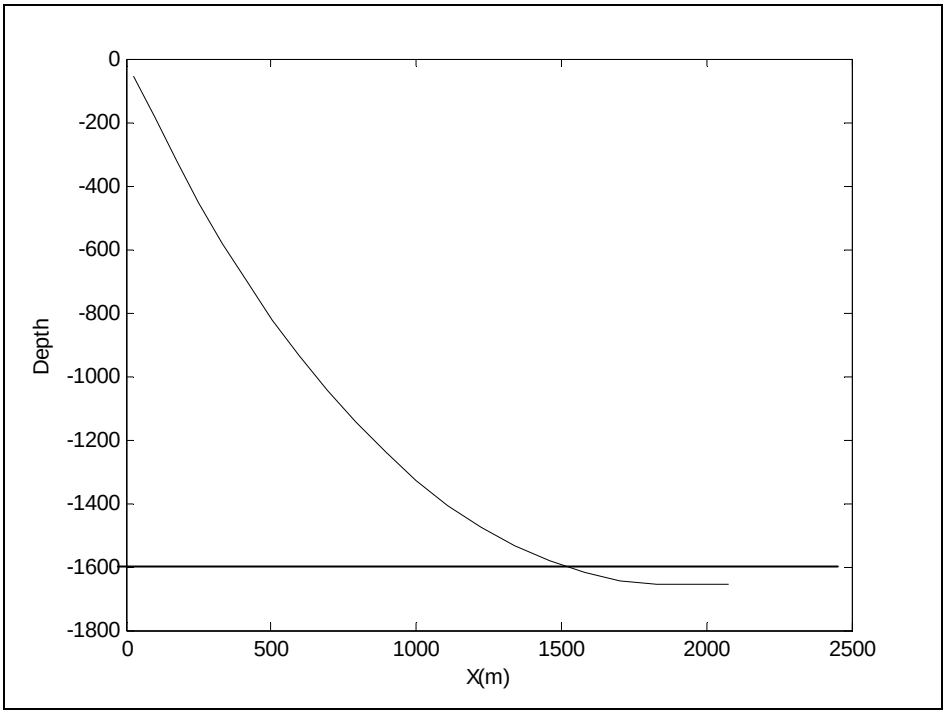

Fig. 70 Equilibrium position of a Steel Catenary Riser (SCR)

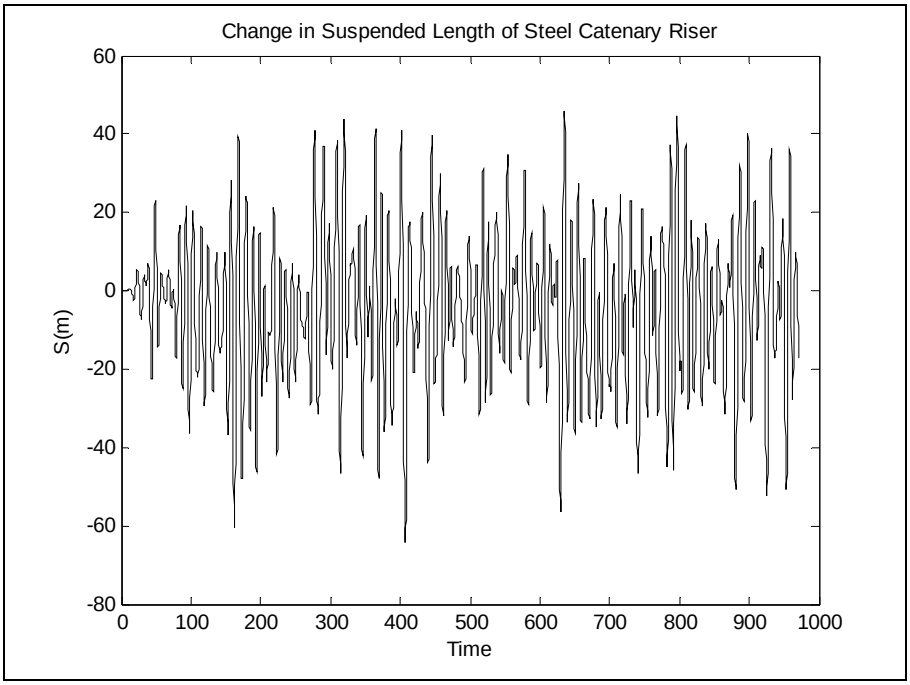

Fig. 71 Time series of suspended length of SCR1 during Hurricane Isidore

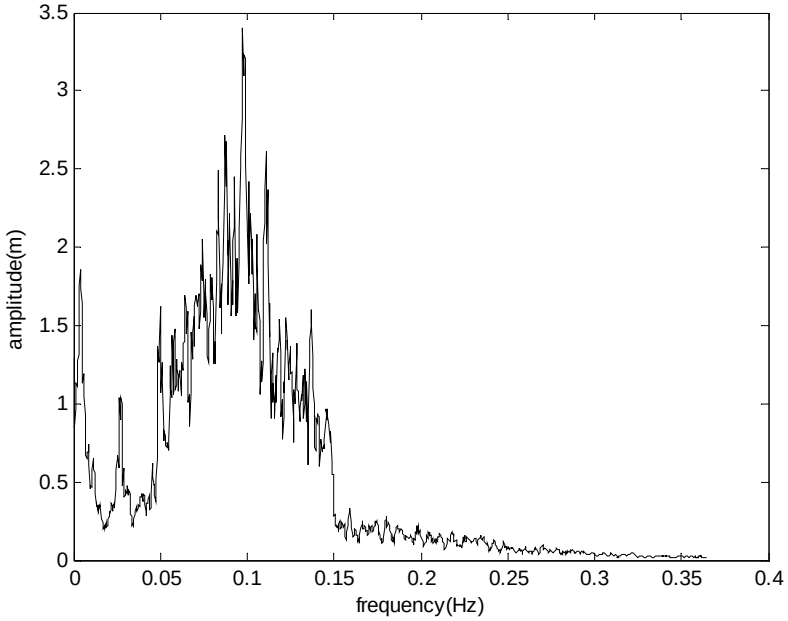

Fig. 72 Amplitude spectrum of change in suspended length of SCR1 during Isidore

Table 10 Sensitivity of SCR1 with the translation motions of spar

Translation Motion	Motion amplitude (m)	Frequency of motion (Hz)	Motion of suspended length (m)	Frequency of motion of suspended length (Hz)	Ratio of suspended length to motion
Surge	5.025	0.0052	3.587	0.0056	0.714
Sway	4.7742	0.0051	2.84	0.0054	0.595
Heave	0.28	0.0503	5.57	0.085	19.89

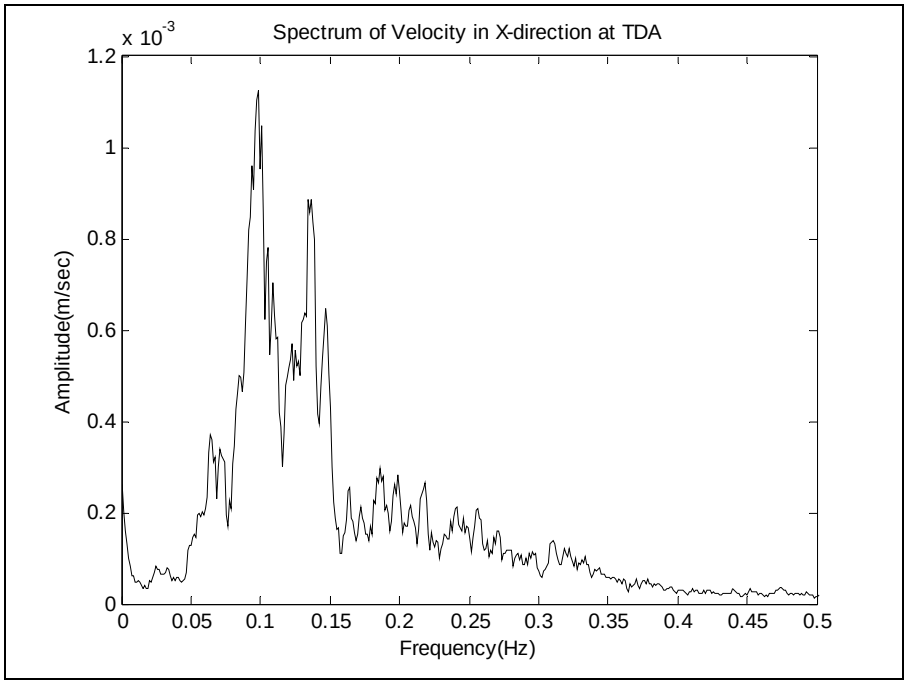

Fig. 73 Amplitude spectrum of velocity in X-direction at TDA

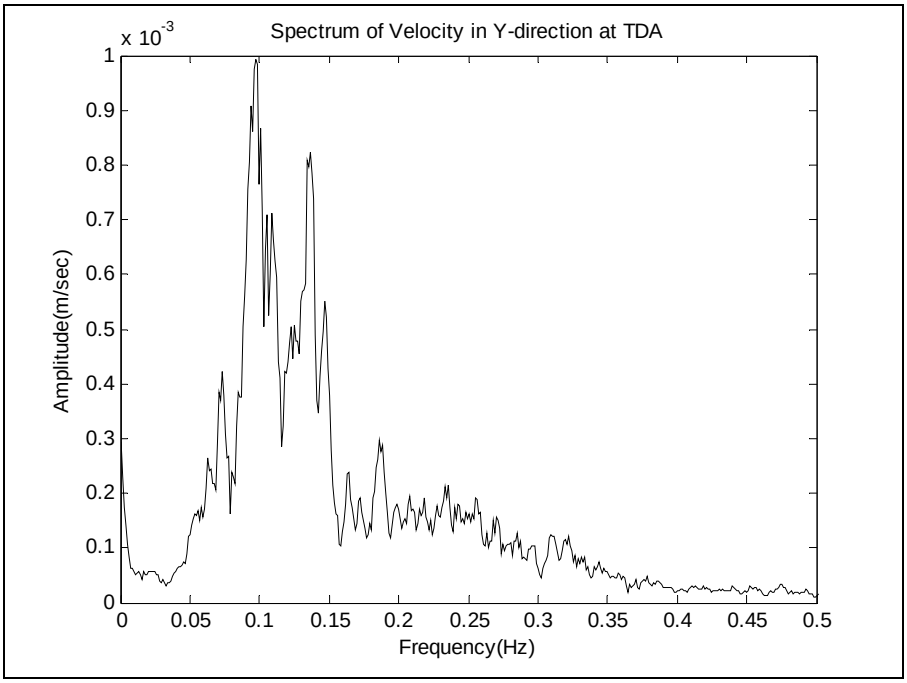

Fig. 74 Amplitude spectrum of velocity in Y-direction at TDA

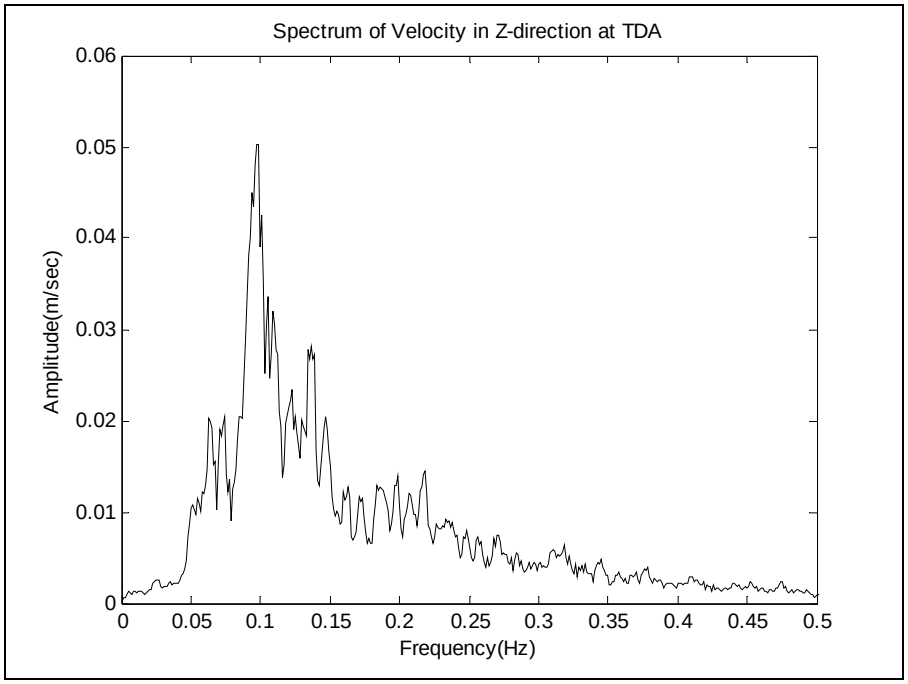

Fig. 75 Amplitude spectrum of velocity in Z-direction at TDA

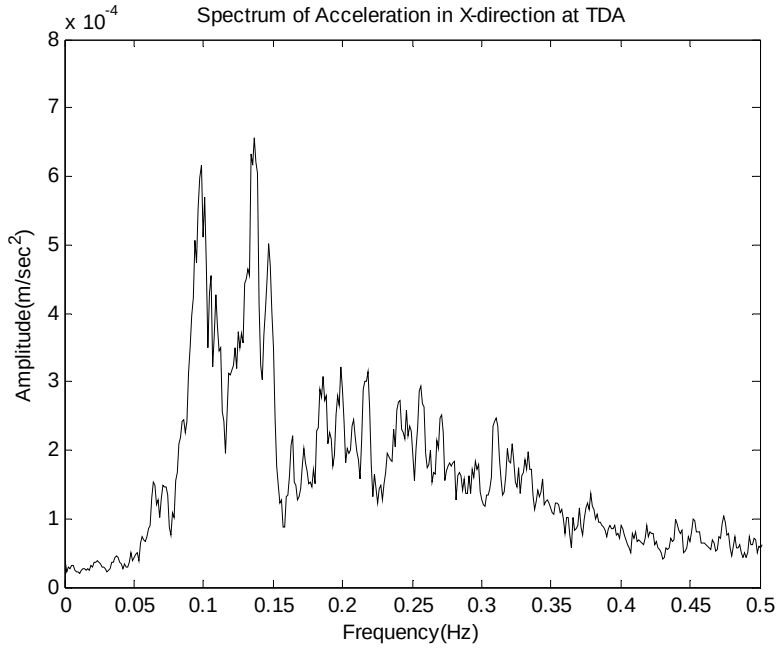

Fig. 76 Amplitude spectrum of acceleration in X-direction at TDA

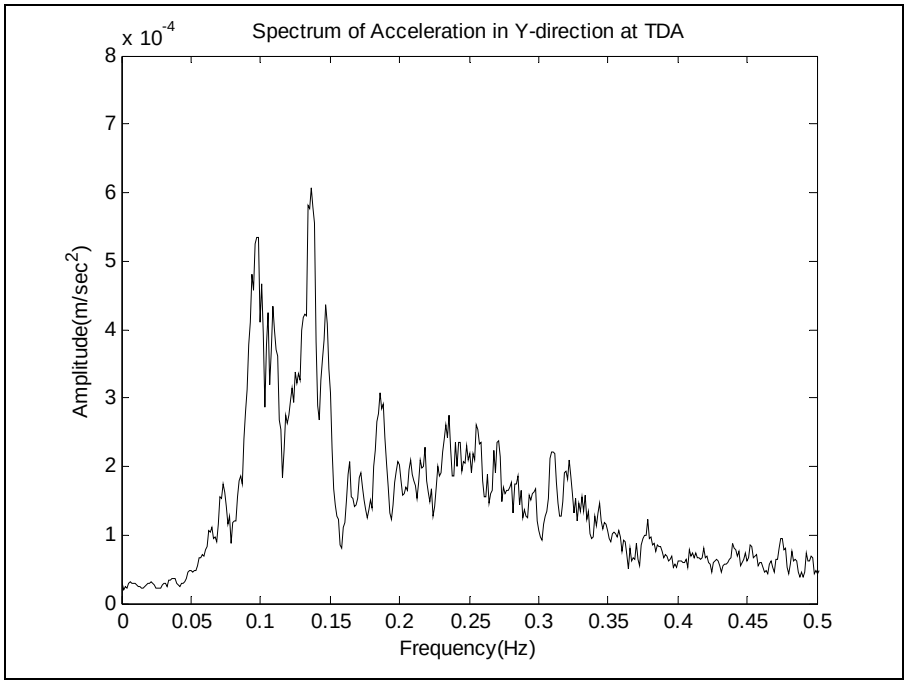

Fig. 77 Amplitude spectrum of acceleration in Y-direction at TDA

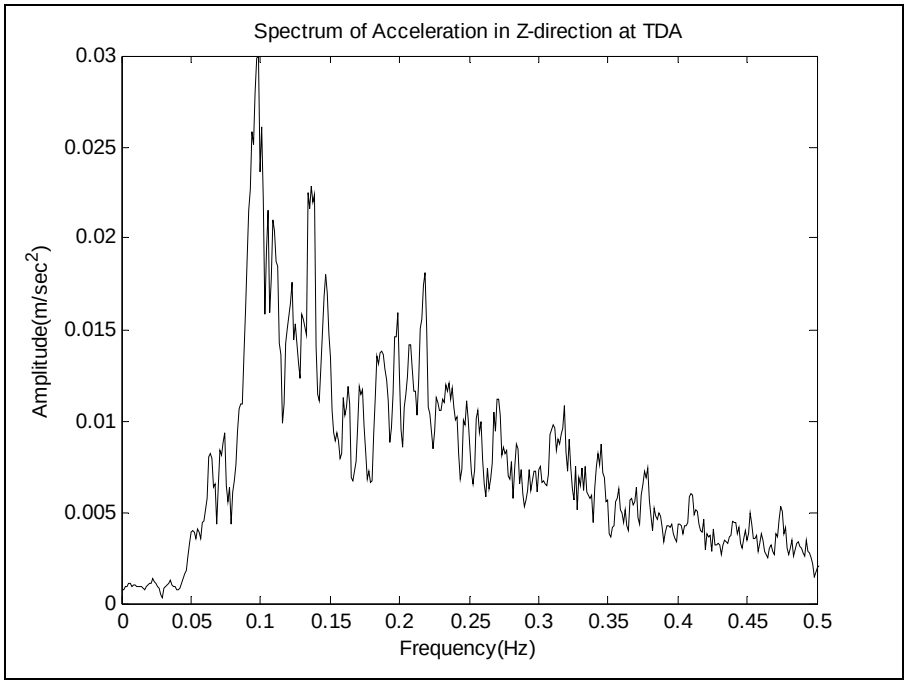

Fig. 78 Amplitude spectrum of acceleration in Z-direction at TDA

5.7 Influence of Hydrodynamic Coefficients of Heave Plates on Heave Motion

As discussed earlier prediction of hydrodynamic coefficients of heave plates is a challenge in the design of truss spars. The heave plates actually trap a large amount of water which moves along with the structure. This trapped water is known as added mass. Effective heave plates increase the added mass of a structure leading to an increase in the heave natural period detuning from the ambient wave period range. Hydrodynamic damping induced by the heave plates is also effective in reducing the heave motions of the spar. But various studies and experiments conducted have indicated that heave motion is primarily inertia dominated and the effect of drag damping is less significant (Magee et al., 2000). In order to study the sensitivity of the hydrodynamic coefficients of heave plates on the heave motion we have selected different combination of damping coefficient, Cd and added mass coefficient, Cm. The energy spectra of heave motion for various combinations of Cd and Cm are shown in Fig. 79. We can see from the figure

that the added mass coefficient influences the heave motion much more than the damping coefficient.

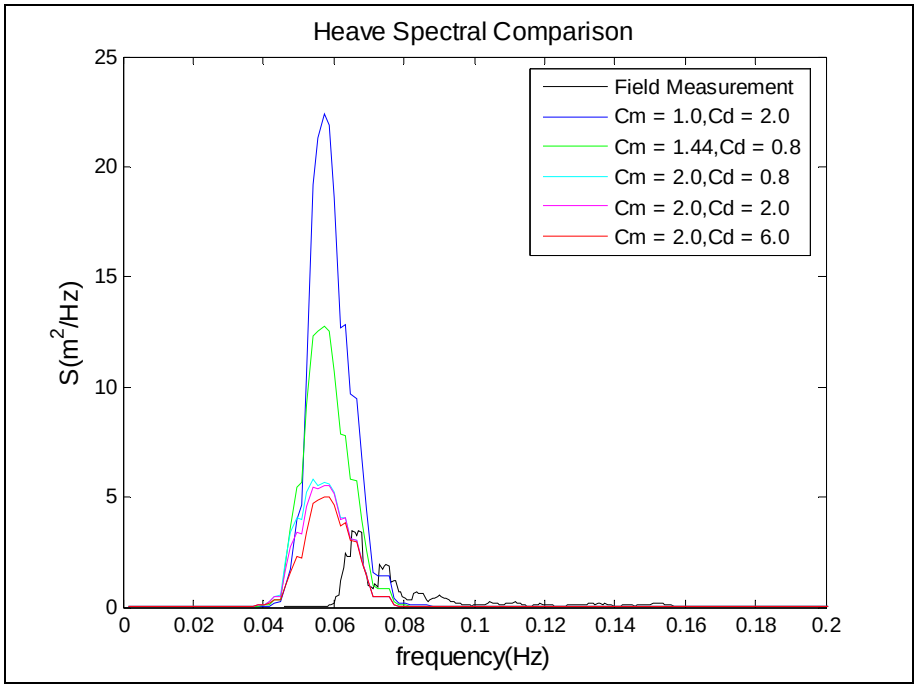

Fig. 79 Heave Spectral comparisons

6. CONCLUSIONS

Horn mountain, a truss spar interacting with its mooring and riser system was analyzed using a time-domain numerical code, known as 'COUPLE' and the results were compared with the corresponding field measurements made during Hurricane Isidore. Satisfactory agreement between the simulation and corresponding measurements is reached, indicating the numerical code, COUPLE, can be used to conduct the time-domain analysis of a truss spar interacting with its mooing and riser system under severe storm impact.

The simulated results show that the mean values of the global motions compare very well with the field measurements. The energy spectra of surge, sway, roll motions show that both slow drift motions and wave frequency motions are reasonably well predicted. The resonant motions of heave, pitch and yaw are over predicted indicating that the friction between the buoyancy cans and the riser guide frames has to be modeled for a more accurate prediction of heave, pitch and yaw.

Similar to the global motions the mean values of mooring line tensions also match very well with those of the field measurements, while the simulated dynamic tensions in mooring lines are almost twice the corresponding measured values. It is noted that the values of dynamic tension are very low compared to the corresponding mean tensions, typically in the range of 3 to 5%. Major reasons for this discrepancy is due to the discrepancies in the predicted global motions and corresponding field measurements, elongation of mooring chain above the fairlead, uncertainties in friction at the fairlead, the field measurements, directionality of wind waves and currents.

The comparative study of three different cases of coupled analysis underlines the significance of interaction of risers with the hull structure. There are substancial differences in the global motions when steel catenary risers and top tensioned risers were also considered in the simulations.

A detailed study on the motions of steel catenary risers near to the touchdown area is also performed which includes the variation of the suspended length of steel

catenary riser (SCR) and sensitivity of SCRs to surge, sway and heave motions of the truss spar. The results show that influence of heave motion is about 35 times greater than that of the surge and sway motions. The amplitude spectrum of variation of suspended length shows that the slow drift motions are very low and the high frequency motions are predominant.

REFERENCES

Argyris, J and Mlejnek, H.P., (1991); "Dynamics of Structures", Elsevier Science Publication Co., New York. Vol.5.

Avila, A. Lixion, (2002); "Tropical Cyclone Report, Hurricane Isidore", http://www.nhc.noaa.gov/2002isidore.shtml, National Hurricane Center (NHC), accessed on 2nd October, 2005.

Chen, Xiaohong (2002); "Studies on Dynamic Interaction Between Deep-water Floating Structures and Their Mooring/Tendon Systems". Ph.D. Dissertation, Ocean Engineering Program, Civil Engineering Department, Texas A&M University, College Station, Texas.

Ding, Y., Kim, M., Chen, X. and Zhang, J (2003); "A Numerical code (COUPLE 6D) for Coupled Dynamic Analysis of Moored Offshore Structures". *Proceedings of the International Symposium*, Deep Water Mooring Systems, Houston, pp. 168 – 182.

Edwards, Rod (2003); "Horn Mountain IMMS". BMT the Marine Analyst – Offshore Technology Conference (OTC) Newsletter.

Garett, D.L., (1982): "Dynamic Analysis of Slender Rods". Journal of Energy Resources Technology, Transaction of ASME 104, pp. 302-307.

Giertsen, E., Verley R. and Schrøder K., (2004);"CARISIMA A Catenary Riser/Soil Interaction Model for Global Riser Analysis". *Proceedings of 23rd International Conference on Offshore Mechanics and Arctic Engineering*, ASME, Vancouver.

Halkyard John, Liagre Pierre and Tahar Arcandra. (2004); "Full Scale Data Comparison for the Horn Mountain Spar", *Proceedings of 23rd International Conference on Offshore Mechanics and Arctic Engineering*, ASME, Vancouver.

Magee Allan, Sablock Anil, Maher Jim, Halkyard John, Finn Lyle and Dutta Indra. (2000); "Heave Plate Effectiveness in the Performance of the Truss Spar". *Proceedings of the ETCE/OMAE2000 Joint Conference on Energy for the New Millennium*, New Orleans. pp. 367-371

MATLAB®, version 7.0.1.24704(R14, 2004); The MathWorks, Inc.

Ma, W. and Webster, W.C., (1994); "An Analytical Approach to Cable Dynamics: Theory and User Manual", SEA GRANT PROJECT R/OE-26.

Nordgren, R.P., (1974); "On Computation of the Motion of the Elastic Rods", ASME Journal of Applied Mechanics, September, pp. 777-780.

Pauling, J.R. and Webster, W.C., (1986); "A Consistent Large-amplitude analysis of the Coupled Response of a TLP and Tendon System". *Proceedings of 5th Offshore Mechanics and Arctic Engineering*, ASME, pp. 126-133.

Prislin Igore, Blevins R.D. and Halkyard J. (1998); "Viscous Damping and Added Mass of Solid Square Plates". *Proceedings of 17th International Conference on Offshore Mechanics and Arctic Engineering*, ASME, Lisbon.

Sarpkaya, T. and Isaacson, M., (1981); "Mechanics of Wave Forces on Offshore Structures". New York: Van Nostrand Reinhold.

Tahar Arcandra, Finn Lyle, Liagre Pierre and Halkyard John. (2005); "Full Scale Data Comparison for the Horn Mountain Spar Mooring Line Tensions during Hurricane Isidore", *Proceedings of 24th International Conference on Offshore Mechanics and Arctic Engineering*, ASME, Greece.

Wood, W.L., (1990); "Practical Time-Stepping Schemes", Clarendon Press, Oxford.

Ye, M., (1994); "Prediction of Unidirectional Irregular Wave Kinematics and Evolution". MS Thesis, Ocean Engineering Program, Civil Engineering Department, Texas A&M University.

Zhang, J., Prislin, I., Yang, J., Wen J., (1997); "Deterministic Decomposition and Prediction of Irregular Ocean Waves". *COE Report No. 358*, Civil Engineering Department, Texas A&M University, College Station, Texas.

Zhang, J., Chen, L., Ye, M., Randall, R.E., (1996); "Hybrid Wave Model for Unidirectional Irregular Waves - Part I Theory and Numerical Scheme". *Applied Ocean Research* 18, pp. 77-92.

http://www.ndbc.noaa.gov/station_page.php, National Oceanic and Atmospheric and Administration's National Data Buoy Center Archives of observations, accessed on September 25th, 2005.

VITA

Basil Theckum Purath
301 Wilcrest Dr., Apt 7302
Houston, TX 77042
Email: basiltp@neo.tamu.edu

EDUCATION

- Master of Science. Graduation date: May 2006
  Major: Ocean engineering
  Texas A&M University
- Bachelor of Technology. Graduation date: June 2001
  Major: Naval architecture and ship building
  Cochin University of Science and Technology

EXPERIENCE

- Texas A&M University, College Station, Texas (January 2005 - January 2006)
  Research Assistant for Dr. Jun Zhang
- Mazagon Dock Ltd. (Oct 2002 – July 2004)
  Naval Architect